Lappeenranta
University of Technology

Ville Niskanen

RADIO-FREQUENCY-BASED MEASUREMENT METHODS FOR BEARING CURRENT ANALYSIS IN INDUCTION MOTORS

Supervisor   Professor Jero Ahola
                      Department of Electrical Engineering
                      LUT Institute of Energy Technology (LUT Energy)
                      Lappeenranta University of Technology
                      Finland

Reviewers   Dr. Ville Särkimäki
                      Senior researcher
                      ABB Service
                      Helsinki, Finland

                      Dr. Rahul Kanchan
                      Senior researcher
                      ABB Corporate Research
                      Västerås, Sweden

Opponent   Dr. Ville Särkimäki
                      Senior researcher
                      ABB Service
                      Helsinki, Finland

Abstract

Ville Niskanen

Radio-frequency-based measurement methods for bearing current analysis in induction motors

The most common reason for a low-voltage induction motor breakdown is a bearing failure. Along with the increasing popularity of modern frequency converters, bearing failures have become the most important motor fault type. Conditions in which bearing currents are likely to occur are generated as a side effect of fast du/dt switching transients. Once present, different types of bearing currents can accelerate the mechanical wear of bearings by causing deformation of metal parts in the bearing and degradation of the lubricating oil properties.The bearing current phenomena are well known, and several bearing current measurement and mitigation methods have been proposed. Nevertheless, in order to develop more feasible methods to measure and mitigate bearing currents, better knowledge of the phenomena is required. When mechanical wear is caused by bearing currents, the resulting aging impact has to be monitored and dealt with. Moreover, because of the stepwise aging mechanism, periodically executed condition monitoring measurements have been found ineffective. Thus, there is a need for feasible bearing current measurement methods that can be applied in parallel with the normal operation of series production drive systems. In order to reach the objectives of feasibility and applicability, nonintrusive measurement methods are preferred.

In this doctoral dissertation, the characteristics and conditions of bearings that are related to the occurrence of different kinds of bearing currents are studied. Further, the study introduces some nonintrusive radio-frequency-signal-based approaches to detect and measure parameters that are associated with the accelerated bearing wear caused by bearing currents.

Keywords: Bearing currents, radio frequency, nonintrusive measurement, low-voltage squirrel cage induction motor, condition monitoring

UDC 621.3:621.3.014:621.313.3:621.822:004.942:537.8

If you don't have a problem to solve, you definitely have a major one

Acknowledgments

Contents

List of publications

This doctoral dissertation is based on the following papers. The rights have been granted by the publishers to include the papers in the dissertation.

I. J. Ahola, V. Niskanen, and A. Muetze (2011), "On the role of the shaft end in the radio-frequency emission of discharge," in *Proceedings of the 14th European Power Electronics and Applications Conference (EPE)*, Birmingham, UK.

II. A. Muetze, V. Niskanen, and J. Ahola (2013), "On radio-frequency based detection of high frequency circulating bearing current flow," in *Proceedings of the International Electric Machines and Drives Conference (IEMDC)*, Chicago, IL, USA, pp. 1289–1294.

III. V. Niskanen, A. Muetze, and J. Ahola (2013), "Study on bearing impedance properties at several hundred kilohertz for different electric machine operating parameters," in *Proceedings of the IEEE Energy Conversion Congress and Exposition (ECCE)*, Denver, CO, USA, pp. 4460–4467.

IV. A. Muetze, V. Niskanen, and J. Ahola (2014), "On radio-frequency based detection of high frequency circulating bearing current flow," *IEEE Transactions on Industrial Applications,* Vol. 50, No. 4, pp. 2592–2601.

V. V. Niskanen, A. Muetze, and J. Ahola (2014), "On the Role of the Shaft End and the Influence of Frame Size and Load Coupling on the RF Emission Characteristics of Induction Motors," *EPE Journal*, Vol. 23, No. 4, pp. 42–50.

VI. V. Niskanen, A. Muetze, and J. Ahola (2014), "Study on bearing impedance properties at several hundred kilohertz for different electric machine operating parameters," *IEEE Transactions on Industrial Applications*, Vol. 50, No. 5, pp. 3438–3447.

VII. V. Niskanen, A. Pinomaa, and J. Ahola (2014), "HF near-field probe for magnitude measurements of EDM bearing currents," in *Proceedings of the 16th European Power Electronics and Applications (EPE)*, Lappeenranta, Finland.

The publications are presented in a chronological order. In this doctoral dissertation, they are referred to as Publication I, Publication II, Publication III, Publication IV, Publication V, Publication VI, and Publication VII.

Abbreviations and Symbols

Roman letters

A	area
A_f	cross-sectional area of the ferrite core
A_H	Herzian area
A_L	individual winding turn
B	magnetic flux density
C	capacitance
C_b	capacitance of a bearing
$C_{b,de}$	capacitance of the drive end bearing
$C_{b,nde}$	capacitance of the nondrive end bearing
C_{rg}	rotor-to-ground capacitance
C_{wf}	winding-to-frame capacitance
C_{wf}	winding-to-rotor capacitance
d_c	distance between capacitor plates
$\mathrm{d}u/\mathrm{d}t$	voltage transient
E_b	energy dissipated in a bearing
E_m	melting energy
E_v	vaporization energy
f	frequency
f_c	central frequency
f_{in}	input signal frequency (carrier wave)
f_s	sampling frequency
$f_{s,dec}$	sampling frequency after decimation
f_{sw}	switching frequency
G_a	antenna gain
G_t	transmitter antenna gain
G_r	receiver antenna gain
H	magnetic field strength
H_f	motor frame size
H_m	energy density for melting $\left[2.2 \cdot 10^{10}\ \mathrm{J/m^3}\right]$
H_v	energy density for vaporization $\left[14.3 \cdot 10^{10}\ \mathrm{J/m^3}\right]$
I_{com}	common-mode current (intrusive DC–100 MHz)
I_{cbc}	circulating bearing current (intrusive DC–100 MHz)
I_{rms}	root mean square current
I_b	bearing current (intrusive DC–100 MHz)
$I_{b,pp}$	peak-to-peak value of bearing current (intrusive DC–100 MHz)
$\hat{I}_b$	peak value of bearing current (intrusive DC–100 MHz)
I_g	ground current (intrusive DC–100 MHz)
I_{HF}	high-frequency current (3–30 MHz)
I_L	insertion loss
I_{rgc}	rotor-to-ground current (intrusive DC–100 MHz)

12

I_{VHF}	very high-frequency current (30–300 MHz)
$I_{\mathrm{wf,HF}}$	high-frequency winding-to-frame current (3–30 MHz)
$I_{\mathrm{wf,MF}}$	medium-frequency winding-to-frame current (300 kHz–3 MHz)
J_{b}	bearing current density
$\hat{J}_{\mathrm{b}}$	peak value of bearing current density
$J_{\mathrm{b,rms}}$	root mean square value of bearing current density
k_{λ}	propagation constant
k	transducer factor $\left[1/\Omega\right]$ dB
L	inductance
l_{ce}	electrical cable length
l_{cm}	mechanical cable length
l_{s}	length of a stator
M	event serial number
m	meaurement data cell number
N	total number of samples
N_{EDM}	total number of EDM event(s)
N_{w}	number of samples in a sample window
N_{wt}	number of winding turns
n	rotation speed [rpm^{-1}]
P_{n}	nominal power
P_{t}	transmission power
P_{r}	received power
P	point of observation
R_{EDM}	resistance in a bearing during EDM
R	resistance
R_{EDM}	resistance in a bearing during EDM
r_{p}	distance to the point of observation
r	radius, distance
T_{b}	operating temperature of a bearing
$T_{\mathrm{b,de}}$	operating temperature of a DE bearing
T	temperature [ºC]
t_{EDM}	duration of an EDM discharge
t_{op}	time of operation
t_{s}	sampling time
U_{in}	input voltage
U_{i}	information signal
U_{out}	output voltage
U_{s}	source voltage
U_{shaft}	voltage between the drive end and the nondrive end of a shaft
U_{com}	common-mode voltage
U_{b}	bearing voltage
U'_{b}	initial bearing voltage level at the moment of an EDM discharge
U_{Lg}	line to ground voltage
$U_{\mathrm{ni\text{-}HFMNFP}}$	output voltage of ni-HFMNFP (5–30 MHz)

U_{th} threshold voltage
v_{cable} signal propagation speed in a cable
W_b bearing stress
$X_{L,ni\text{-}HFMNFP}$ inductive reactance of ni-HFMNFP
Z_b impedance of a bearing
$Z_{b,EDM}$ bearing impedance during EDM
Z_{probe} termination impedance of a probe
Z_t transfer impedance

Greek alphabet

α phase angle
ε_0 permittivity of vacuum
ε_r relative permittivity
λ wavelength
μ_0 permeability of vacuum
μ_r relative permeability
μ_i initial permeability
ψ magnetic coil flux
ϕ_e elevation angle
ϕ_i inclination angle
φ azimuth angle
ω angular frequency

Abbreviations

AC   Alternating current
AM   Amplitude modulation
ASK   Amplitude shift keying
BC   Bearing current
BVR   Bearing voltage ratio
BPF   Band-pass filter
CBC   Circulating bearing current
DA   Discharge activity
DC   Direct current
DE   Drive end
DSP   Digital signal processor
EDM   Electrical discharge machining
EMI   Electromagnetic interference
ENF   Electric near field
ESIM   Electrostatic shielded induction motor
ETSI   European Telecommunications Standards Institute
FCC   Federal Communications Commission

14

FFT	Fast Fourier transform
FF	Far field
HF	High frequency (3–30 MHz)
HPF	High-pass filter
IGBT	Insulated gate bipolar transistor
LF	Low frequency (3–300 kHz)
LV	Low voltage (U_{rms} 400/690 V)
LPF	Low-pass filter
LVSCIM	Low-voltage squirrel cage induction motor
MF	Medium frequency (300 kHz–3 MHz)
MNF	Magnetic near field
MV	Medium voltage
NF	Near field
ni-HFMNFP	Nonintrusive HF magnetic near-field probe
NDE	Nondrive end
NEC	Numerical electromagnetic code
PE	Protective earth
PMA	Pulse magnitude analyzer
PWM	Pulse width modulation
RCMV-PWM	reduced common-mode voltage pulse width modulation
RF	Radio frequency (3 kHz–300 GHz)
RFI	Radio frequency interference
RF-SBBCDM	Radio-frequency-signal-based bearing current detection method
rms	Root mean square
rpm	Rounds per minute
SNR	Signal-to-noise ratio
RGC	Rotor-to-ground current
TrA	Transient activity
VSI	Voltage source inverter
VHF	Very high frequency (30–300 MHz)
OEM	Original equipment manufacturer
MOD	Maintenance and operational data

1 Introduction

It is nearly a century since classical bearing currents were recognized in (Alger and Samson, 1924). It was stated that in the case of low-voltage (LV) motors, a bearing current of this kind would be a significant cause of degradation in bearings of larger motors only (i.e., 500 Hp ~ 375 kW). The problem was considered important since the operating conditions of bearings of a motor play a significant role on the system performance. The quality of production can be degraded even by incipient wear of a bearing, where vibration may cause an incorrect operation of the motor. When an incipient bearing fault progresses into a failure state, it causes a production downtime, which leads to economic losses. This holds true especially in cases where production interference is unexpected (a sudden failure of a bearing). A breakdown of a bearing is caused by mechanical wear of bearings, which can be caused by a lack of lubrication or deformation of raceways or rolling elements. However, by appropriate condition monitoring, unexpected downtimes can be reduced (the length and number of downtimes). Over the past few decades, bearing currents have been found to accelerate mechanical wear also in LV motors of all sizes, thereby significantly shortening the lifespan of bearings (Bonnett, 2000). For example, in 1995 (Bell et al., 1998), a synthetic fiber manufacturer reported an increment of bearing failure density. In the studied system driven by a pulse-width-modulated insulated gate bipolar transistor voltage source inverter (PWM IGBT VSI), failures occurred seven times more often than in systems running without a VSI. After a six-month period, the maintenance team found the PWM IGBT VSI-driven system to be unreliable. It was reported that the grease in the bearings used in the PWM IGBT VSI-driven motor was discolored, and its consistency had changed so that the lubricant properties of the grease were substantially degraded. This trend can be seen in Fig. 1.1, which illustrates the dominating role of bearing faults related to additional bearing current types that may be found in LV motors.
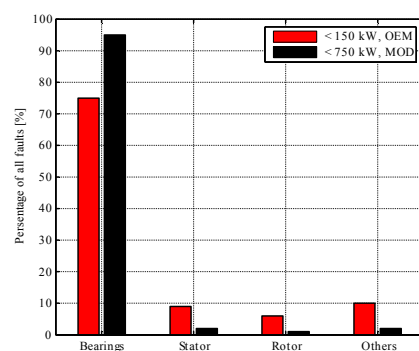

Fig. 1.1. Origins and proportions of faults in a small LVIM (low-voltage induction motor) given by the original equipment manufacturer (OEM) for motors and generators $P_n \leq 150$ kW (black) and the maintenance and operational data (MOD) for motors and generators $P_n \leq 750$ kW (red) in years 1995–1997 (Tavner et al., 2008).

It is pointed out here that the surveys considering broken parts in electrical machines are from the 1990s, when the number of VSI applications was rapidly growing and the problem was still new, and thus, mitigation methods were not yet available. On the other hand, to the author's knowledge, there are no surveys available that are up to date and illustrate the current situation. Based on histograms, it can be stated that for all sizes of LVIMs, most of the motor faults are related to a bearing failure. However, although bearing faults constitute a large proportion of all faults of motor origin, the life span prediction methods that are based on bearing failure histograms are still found to be inadequate. This is due to multiple variables that affect the bearing wear (Bell et al., 1998). Therefore, a lot of effort has been put into research on bearing currents over the past few decades. According to (Guttowski et al., 2006; Muetze and Binder, 2003; Muetze and Binder, 2007), practice has shown that if $I_{rgc} \approx 0$, the size of the motor determines whether CBC or EDM is dominating. Furthermore, as suggested by (Tischmacher et al., 2010), also certain operating parameters such as rotation speed and temperature have a significant effect on the bearing current types present at a certain moment. However, it is worth noting that bearing current measurements require modifications to the motor.

The objective of this doctoral dissertation is to develop methods to detect and evaluate bearing currents by nonintrusive measurements. The dissertation introduces and demonstrates new opportunities for different measurements and simulation methods that are enabled by the radio frequency (RF) nature of the bearing current phenomena. Therefore, the novelty of the work lies in the application of RF simulation modeling, signal processing techniques, and methods that allow nonintrusive detection of different kinds of bearing currents, and further, measurement of the magnitude of the electrical discharge machining (EDM) current pulses. The approach enables advanced development of a measurement system that can be applied in field conditions with conventional series production motors. Before that, bearing current phenomena caused by VSIs are studied by providing a review of publications on bearing currents. The review addresses the following aspects:

- Different types of bearing currents caused by VSIs
- Cause-effect chains of different bearing current types
- Parameters involved in bearing current phenomena
- Methods to measure bearing currents
- Aging impact of bearing currents
- Mitigation techniques for bearing currents

The studies in this doctoral dissertation are limited to low-voltage squirrel cage induction motors (LVSCIMs), although the same effects and phenomena may also occur in different types of low- and medium-voltage motors and generators. After the review of the background, the outline of the dissertation is provided, and the appended original publications are introduced. Finally, the scientific contributions of the doctoral dissertation are discussed.

1.1 Bearing current phenomena

There are four main types of VSI-induced bearing currents. These bearing current types are: small capacitive currents, EDM, circulating bearing currents (CBC), and rotor-to-ground currents (RGC) (Guttowski et al., 2006; Muetze and Binder, 2003). Recently, a fifth, combined bearing current has been introduced (Muetze, 2008). In practice, the latest one is a combination of EDM and CBC, and is thus not studied or discussed in this doctoral dissertation any further. Excluding small capacitive currents, the bearing currents mentioned above are substantial to cause damage to bearings. In addition, the mechanical dimensions of motors are shown to contribute to which kinds of bearing currents are capable of degrading bearings in each motor size (Muetze and Binder, 2003). Furthermore, bearing current phenomena can be divided into two mechanisms. The root cause for both mechanisms is a high du/dt waveform at the motor terminals (Muetze and Binder, 2003; Muetze and Binder, 2007a). A cause-effect chains of four main VSI-induced bearing current types are introduced and illustrated in Fig. 1.2.
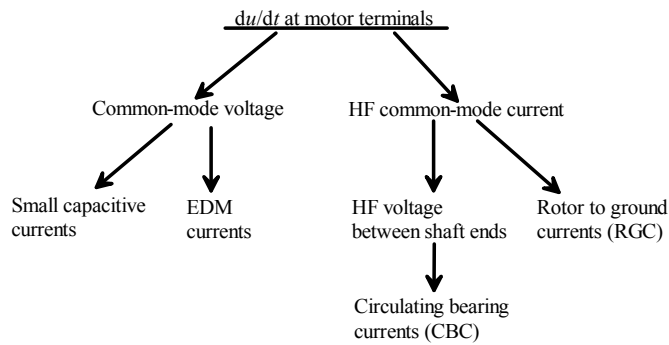
Fig. 1.2. VSI-induced bearing current types and their origins (Muetze and Binder, 1997; Muetze and Binder, 2003; Muetze and Binder, 2007).

1.1.1 Origin of small capacitive currents and electrical discharge machining (EDM) currents

VSIs are known to cause a common-mode voltage U_{com} between the neutral point (star connected) or the singular point (delta connected) of a stator winding and the frame of a motor. This is due to the asymmetrical structure of a conventional two-level, three-phase VSI, where at least two of the three phases are connected to the same voltage potential of two possible voltage levels. In star-connected stator windings, U_{com} can be measured directly between the neutral point and the reference point, the ground potential. Alternatively, U_{com} can be determined by phase-to-ground voltage measurements, which is also applicable to delta-connected motors

18

$$U_{com} = \frac{U_{ug} + U_{vg} + U_{wg}}{3} \qquad (1.1)$$

.

Simplified equivalent circuits of star- and delta-connected windings are illustrated in Fig. 1.3.
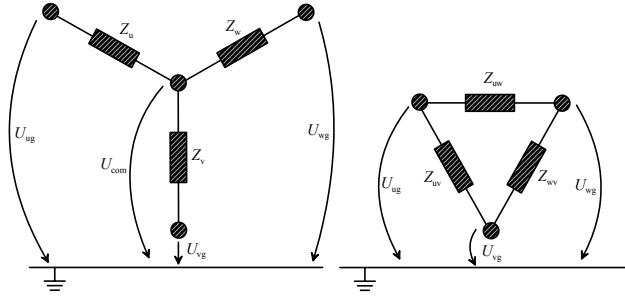
Fig. 1.3. Simplied equivalent circuits of three-phase star- (on the left) and delta-connected (on the right) stator windings.

Because of the requirements of low switching losses and fast closing and opening times of semiconductor switches, such as an IGBT, a high du/dt is introduced in the stator windings of a motor. In the case of an IGBT VSI, du/dt includes frequencies up to the high-frequency (HF) range (Wu, 2006). At this point, stray capacitances in an LVSCIM become significant thereby allowing the occurrence of different kinds of bearing currents. The crucial capacitances related to bearing currents are: the rotor-to-frame capacitance C_{rf}, the stator winding-to-frame capacitance C_{wf}, the stator winding-to-rotor capacitance C_{wr}, and the bearing capacitance C_b, which is a common notation for the capacitance of the drive end (DE) bearing $C_{b,de}$ or the capacitance of the nondrive end (NDE) bearing $C_{b,nde}$. These capacitances can be analytically calculated by the equations presented in (Adabi et al., 2010; Busse et al., 1997b; Zare, 2010). In addition, the initial value of C_{wf} can be quite easily measured when the rotor of a motor is removed. However, measurement of the other capacitances requires special arrangements, and some of them, such as bearing capacitances, are likely to vary during operation. Because of these capacitances, the medium-frequency (MF) and HF components of U_{com} are coupled through C_{wr} to the parallel capacitances $C_{b,de}$, $C_{b,nde}$, and C_{rf}, which are charged during du/dt of U_{com} in the stator windings. This results in the generation of a bearing voltage U_b (Busse et al., 1997a), which can be further specified as $U_{b,de}$ and $U_{b,nde}$ when relevant. The circuit described above is called a capacitive voltage divider, and its simplified equivalent circuit is given in Fig. 1.4.
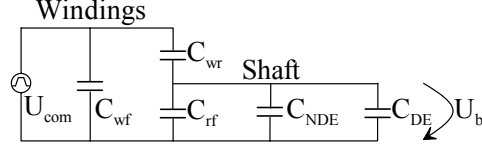
Fig. 1.4. Simplified equivalent circuit of a voltage divider for EDM and small capacitive currents.

As can be seen in Fig. 1.4, there is a relation between U_{com} and U_b. The dependency is called a bearing voltage ratio (BVR), and it is determined by

$$BVR = \frac{U_b}{U_{com}}.$$
(1.2)

Alternatively, BVR can be expressed by coupling the capacitances involved in the capacitive voltage divider (Busse et al., 1997a; Busse et al., 1997b)

$$BVR = \frac{C_{wr}}{C_{wr} + 2C_b + C_{rf}}.$$
(1.3)

Typical BVR values are in the range of 0.03–0.1 (Muetze and Binder, 2007b). In addition, since bearing capacitances are likely to vary during operation, a feasible approach to bearing capacitance calculation is given in (Busse et al., 1997b), where the rolling element is assumed to lie against one of the two raceways so that only one film layer of insulation oil is involved:

$$C_b = 0.5 \frac{\varepsilon_0 \varepsilon_r A_H}{d_c},$$
(1.4)

where a typical bearing lubricant thickness d_c is in the range of 0.2–2 μm, and the Herzian contact areas A_H usually range from square millimeters up to tens of square millimeters. This typically results in bearing capacitance values from tens of picofarads to hundreds of picofarads when the relative permittivity of the lubricant grease is $\varepsilon_r \approx 3$. According to the capacitance and U_{com} values, it is possible to estimate the bearing voltage. For example in (Busse et al., 1997b), the capacitance values for a $P_n = 5.5$ kW motor (15 Hp) are calculated as follows: $C_{wf} \approx 10$ nF, $C_{rf} \approx 1$ nF, $C_{wr} \approx 100$ pF and $C_b \approx 20$–200 pF, thereby resulting in BVR = 0.07–0.09 and $U_b = 26$–34 V, which are based on the approximated value of $U_{com} = 373$ V.

1.1.2 Small capacitive currents

According to (Muetze and Binder, 2003; Muetze and Binder, 2007a), small capacitive currents are considered to be harmless to bearings. The magnitude of these currents ranges from 5 to 200 mA, and thus, the resulting bearing current densities are considered insignificant from the perspective of aging impacts. Moreover, these currents are likely to flow through the bearing capacitances without causing discharges or a requirement of galvanic contact within the bearing. Small capacitive currents share the same coupling method and are generated by the HF part of U_{com} similarly as EDM bearing currents. Because they are considered insignificant from the viewpoint of bearing aging, these currents are not discussed in this doctoral dissertation in more detail.

1.1.3 EDM currents

Electrical discharge machining (EDM) currents are recognized to cause degradation of bearings. When considering the aging impact of EDM, it is proposed that EDM may cause critical current densities inside bearings in motors with frame sizes up to 132 mm $\leq H_f \leq$ 160 mm. In these cases, A_H is usually in the range of square millimeters (Muetze and Binder, 2003; Shancheng and Zhenggou, 2006; Muetze and Binder, 1997; Muetze and Binder, 2007a). Considering EDM, melting and possible vaporization of metal and deformation of the lubricant oil are caused by an arc (Muetze et al., 2006). As a consequence of the EDM discharge, microcraters, also called pitting, may be generated to the surfaces of the bearing raceways. This effect is suggested to increase the significance of the aging caused by the EDM. Typical bearing wear caused by the EDM is shown in Fig. 1.5, where the Nachi C3-6309 ball bearing used in the EDM measurements at Lappeenranta University of Technology is disassembled and opened. It is worth noticing that the signs of aging are visible already when the bearings have run $t_{op} \approx$ 2000 h.

| (a) | (b) |

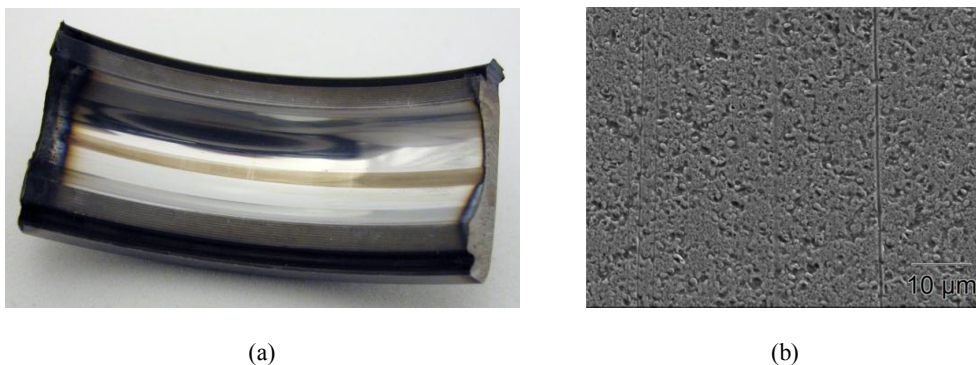Fig. 1.5. Bearing wear caused by EDM bearing currents. Fig. 1.5a. Optical view of a bearing subject to EDM. Fig. 1.5b. Electronic microscope view from the surface of the corresponding piece of the outer raceway. As a consequence of the aging test, several microcraters can be clearly seen in the Nachi 6309-C3 ball bearing lubricated with a synthetic grease and operated for $t_{op} \approx$ 2000 h (right).

An EDM phenomenon illustrated in Fig. 1.6 occurs if a rotor is not properly grounded, meaning that there is no low-impedance path from the rotor to the ground. Only an incipient balancing current is probably present, and thus, capacitances are capable of charging. Such a condition usually prevails when a shaft coupler is insulated or a load has no galvanic connection to the ground; for example, the load is not supported by additional bearings. When the voltage threshold level of the bearing lubricant is exceeded, the energy stored into C_{tot} is discharged through the bearing. A bearing voltage breakdown occurs typically when U_b reaches a 5–30 V level. A discharge can be detected as a high du/dt in U_b and as an associated current pulse I_b through the bearing. Usually, the peak amplitudes of the current pulses are reported to vary from 0.5 to 3 A (Guttowski et al., 2006; Muetze and Binder, 2003; Muetze and Binder, 2007a; Särkimäki, 2009; Ahola et al., 2010; Muetze et al., 2010). On the other hand, (Kriese et al., 2010) reports that the resistance of an EDM discharge R_{EDM} inside a bearing is approximately $3 \pm 1.5 \ \Omega$ and varies case by case. In practice, this would mean that a discharge from $U'_b = 8$ V should result in peak values of bearing current ranging from ~1.8 to ~5.3 A. As can be seen, in the worst case, the announced deviation in R_{EDM} may result in three times as high bearing current magnitudes as in the presented case. It is possible that such an uncertainty may make the accuracy of the analysis inadequate for aging impact studies. However, it is noted here that the results are based on measurements carried out with a special bearing test platform (Kriese et al., 2010). Furthermore, by contrast, typical waveforms of U_b and I_b of an EDM discharge are shown in Fig. 1.7 when measured from an LVSCIM equipped with plastic-sleeve-insulated bearings. It is pointed out that because of the modifications in the motor structure, the both measurements are likely to result in different signal characteristics when compared with conventional series production LVSCIMs.
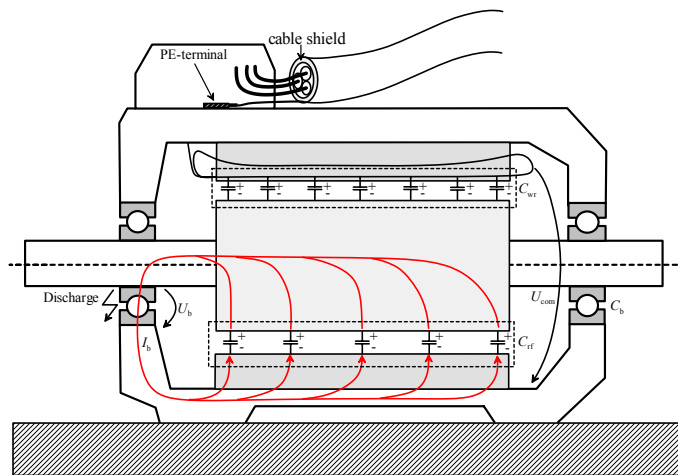
Fig. 1.6. EDM bearing current mechanism, where the rotor-to-frame and bearing capacitances are charged to a certain voltage potential compared with the frame of the motor, eventually causing a balancing current that flows through a bearing of the motor.
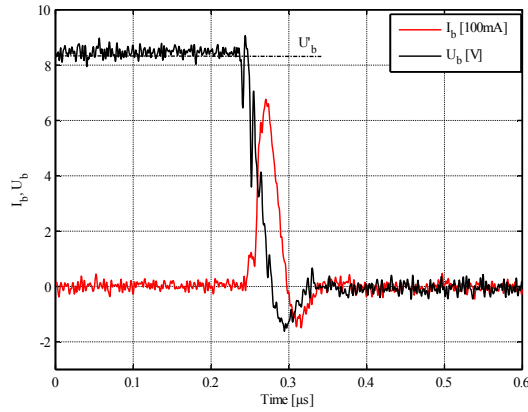
Fig. 1.7. Typical waveforms of the bearing voltage U_b with a discharge voltage level U'_b and a bearing current I_b during an EDM discharge. The example EDM event is recorded by intrusive measurement from a $P_n = 15$ kW, four-pole, LVSCIM, with SNR 6309-C3 bearings lubricated with a mineral-oil-based grease.

Several operating parameters are reported to have an effect on the voltage threshold level of a lubricant film (Muetze and Binder, 1997; Busse et al., 1997b; Tischmacher et al., 2010; Muetze et al., 2010; Ahola et al., 2010). For example, it is proposed that the breakdown voltage of a bearing lubricant is highly dependent on the operating temperature and the rotation speed. (Kriese et al., 2012) continues that the bearing voltage level defined by the BVR is more likely achieved at a temperature of $T_b = 20$ °C than at $T_b = 80$ °C when the rotation speed is between $500 \leq n \leq 3000$ rpm before the breakdown occurs. This is because in the case of $T_b = 80$ °C, the lubricant film is so thin that a significant bearing voltage cannot be gained over it. Furthermore, the electrical properties of different kinds of lubricants are shown to have an effect on the voltage threshold level and thereby on the occurrence of EDM bearing currents. The influence of different lubricants is discussed in more detail in section 1.1.9. In addition, the aging impact of EDM bearing currents is studied in section 1.1.4. Moreover, (Muetze and Binder, 2007a) reports that an aging impact trade-off between EDM and circulating bearing currents (CBC) takes place within a frame size range of $100 \text{ mm} \leq H_f \leq 280 \text{ mm}$. CBC is addressed in more depth in sections 1.1.5 and 1.1.6.

Because of difficulties involved in the measurement of different quantities associated with EDM bearing currents, several electrical simulation models and equivalent circuits to simulate and analyze EDM bearing currents have been introduced by various authors (Särkimäki, 2009; Busse et al., 1997c, Kriese et al., 2010, and Ahola et al., 2010). For example (Kriese et al., 2010) proposes a structure illustrated in Fig. 1.8. With the simulation model, it is possible to estimate the EDM and capacitive currents of a certain motor. The estimation of I_b is based on an intrusive U_b measurement, according to which the bearing voltage source E_b is determined.
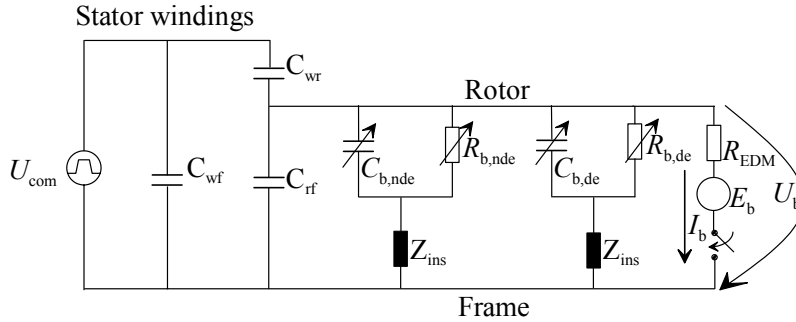
Fig. 1.8. Equivalent circuit model of a motor for EDM current simulations.

In the simulation model, $R_{b,de}$ and $R_{b,nde}$ represent the bearing resistances and R_{EDM} the EDM discharge resistance. Z_{ins} are formed by bearing insulations and shorting wires that are required for the intrusive bearing current measurement used for reference measurement purposes. It is pointed out that the applicability of the circuit model shown in Fig. 1.8 is tested with bearings that are assembled in a special test bench instead of a conventional motor. In other words, this means that a separate test bench that has no rotor frame capacitance may not lead to similar measurement results as would be obtained with a test setup where the LVSCIM is modified to enable similar tests.

1.1.4   Harmful EDM current densities and energies

In the case of EDM, each time the EDM current penetrates through the lubricant film, a small amount of metal from the bearing raceway is removed, and thus, a microcrater (pitting) is produced (Muetze et al., 2006). The crater and the resulting surface roughness will either be flattened by the following bearing ball, or the bearing ball is forced to jump over the crater thereby introducing a fluting effect. It is noteworthy that discharges do not have only pitting and surface roughening effects, but they also cause changes in the structure of the lubricant oil, thus reducing the lubrication characteristics of the oil (Stack et al., 2003; Bell et al., 1998). According to (Gettowski et al., 2006; Muetze and Binder, 2007; Muetze and Binder, 2003; Muetze and Binder, 1997; Stack et al., 2003), EDM is considered harmful only if it reaches a certain magnitude. At this point, the aging effects mentioned above become significant. To study the issue, in (Stack et al., 2003), a set of test runs were performed. The target was to study how much current is needed to significantly reduce the bearing life. To this end, harmful magnitudes are often defined by the bearing current density $\hat{J}_b$, which is a function of the Herzian surface area A_H and the magnitude of the bearing current pulse $\hat{I}_b$

$$\hat{J}_b = \frac{\hat{I}_b}{A_H}.$$

(1.5)

The equation takes into account that at a low speed or in a stationary position the rolling elements have larger contact areas, and thus, higher current magnitudes can flow through the bearing without causing degradation. In (Muetze et al., 2004) it is noted that with intrusive I_b measurements, $BW_{I,b} = DC{\sim}50$ MHz is used in the aging impact studies. Further, in (Busse et al., 1997a; Busse et al., 1997c), the expected lifetime LT_e set by the bearing currents for a bearing in a VSI-driven system can be estimated according to

$$LT_e[\text{h}] = 7867204 \cdot 10^{-\left(2.17\left(\frac{\hat{I}_b}{A_H}\right)\right)}.$$

(1.6)

It is worth noticing that the equation assumes the magnitude of bearing current density to be fixed. Thus from the analysis uncertainty point of view, when $\hat{J}_b = 1$ A/mm^2 is measured, $LT_e = 53189$ h (six years) is given. Again, if uncertainty of $\left|\Delta\hat{J}_b\right| = 0.1$ A/mm^2, then, in the worst case, the estimate can have any value in the range of 32271–87663 h (3.5–10 years). Furthermore it is noted that the amount of discharges is not taken into account either. In addition, we may point out that Eq. (1.6) relies on the fact that the bearing current flows through a Herzian area, and this approximation may cause more uncertainty if an EDM current is likely to flow through a substantially smaller area as proposed in (Muetze, et al., 2006). For these reasons, the aging impacts of different EDM current densities are classified in a more general form into three main groups presented in Table 1.1.

Table 1.1. Aging impact of the EDM as a function of bearing current density.

Classification, $\hat{J}_b[\text{A/mm}^2]$	Safe operation	Aging impact	Destructive
Reference			
(Muetze; Binder, 2003)	0.1–0.3	0.7–	
(Muetze, Binder, 2007)	< 0.4	0.6–0.8	≥ 0.8
(Stack et al., 2003)	≤ 0.1		
(Busse et al., 1997c)	< 0.6	> 0.8	2

Within the safe operating region, it is estimated that these magnitudes of current densities are not sufficient to cause damage to a bearing or significantly reduce its lifetime. The current densities within the 'aging impact' region are considered to be sufficient to cause aging of the bearing. The current densities in the "destructive" region are found to have a significant influence on the lifetime of the bearing. As can be seen in Table 1.1, similar findings on the aging impacts of EDM as a function of $\hat{J}_b$ have been reported by several authors.

As noted earlier, again in (Kriese et al., 2012), the electrical wear of a bearing is demonstrated to be a function of the number of EDM events, not only $\hat{J}_b$. For this reason, other approaches to estimate and analyze additional bearing wear caused by

bearing currents are also studied. In (Muetze et al., 2006; Stack et al., 2003), an analysis of the dissipation of electrical energy E_b in a bearing is provided. It is proposed that

$$E_b = U'_b \cdot \hat{I}_b \cdot t_{EDM} \tag{1.7}$$

can be used to analyze the energy of an individual discharge. Again, (Muetze et al., 2006) continues that

$$E_{b,tot} = U'_b \cdot \hat{I}_b \cdot t_{EDM} \cdot N_{EDM} \tag{1.8}$$

could be applied to the estimation of the total dissipated energy in a bearing. In Eq. (1.8), t_{EDM} is the duration and N_{EDM} is the number of an individual EDM pulse involved in the study. This equation takes into account the variation in the DA that may occur within the analysis period. Hence, Eq. (1.8) is assumed to be applicable to EDM currents; however, it does not take into account that U'_b and I_b may vary over the period under study. This will increase the uncertainty of the analysis. Furthermore, because of the need for the intrusive measurement of I_b in Eq. (1.8), the analysis based on the equation can be considered impossible in series production motors. Therefore, the capacitance energy equation given for example by (Ahola et al., 2010) and the total energy dissipated in a bearing (1.8) can be combined, and hence

$$E_{b,tot} = \frac{1}{2} C_{tot} U'_b \cdot N_{EDM} \tag{1.9}$$

can be proposed. In this case, it is assumed that all the energy charged to C_{tot} is dissipated in the bearing. Again, according to (Tischmacher and Gattermann, 2010), where the aging impact of EDM bearing currents in the case of a 6210-type ball bearing is examined by the dissipated discharge energy, it is reported that the energy required to vaporize a certain size of a microcrater can be determined by

$$E_v = H_v \cdot r^3, \tag{1.10}$$

where the energy density $H_v = 14.3 \cdot 10^{10}$ [J/m^3], and r is the radius of the microcrater. Similarly, the energy density required to melt a certain area is determined by $H_m = 2.2 \cdot 10^{10}$ [J/m^3]. The required EDM discharge energy levels for different aging levels are shown in Fig. 1.9a. Moreover, the aging impact of different U'_b levels with different C_{tot} values is presented in Fig. 1.9b. Subplot A depicts U'_b required for vaporization, and the formation of microcraters of different sizes is shown for different values of C_{tot}. Similarly, in subplot B, the U'_b values for melting effects are given. It is worth noticing that there is no information on the applicability of the estimation method for different sizes of bearings and the impact of different sizes of A_H.

(a)   (b)
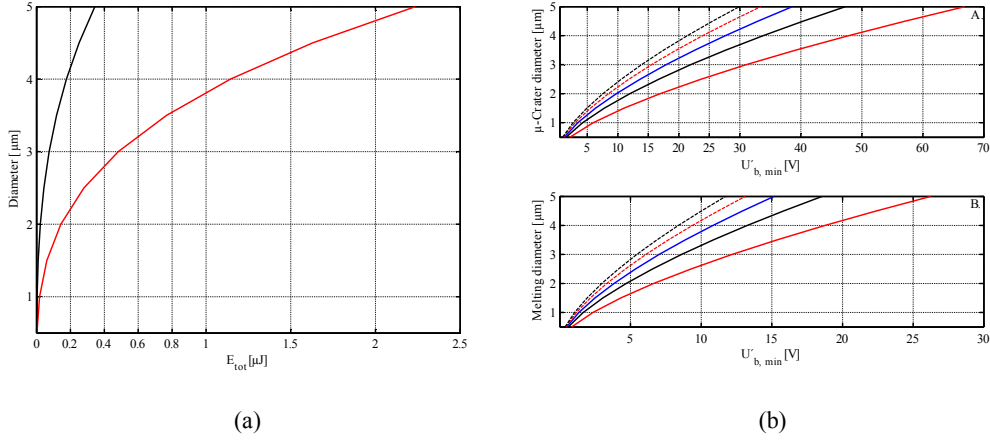
Fig. 1.9a. Estimation of the aging impact by EDM discharge energies; the required discharge energies for different aging levels. The energy required for melting areas of different sizes (black); the energy required to vaporize and produce different sizes of microcrates (red). Fig. 1.9b. Estimation of the aging impact by U'_b with different C_{tot} values. Subplot A shows the U'_b levels required for different microcrater sizes with different C_{tot} values. Subplot B presents the U'_b levels required for different melting sizes with different C_{tot} values. C_{tot} = 1 nF (red), C_{tot} = 2 nF (black), C_{tot} = 3 nF (blue), C_{tot} = 4 nF (dashed red), C_{tot} = 5 nF (dashed black).

It is known that the surface roughness of bearing raceways lowers the threshold voltage level of the lubricant film and excites an EDM DA (Stack et al., 2003). Similarly, the EDM DA is increased when the motor is warming up. On the other hand, it is stated that in these operating conditions, an individual discharge may possess less energy than the discharges from a higher U'_b level. However, when considering the aging impact of EDM bearing currents, the criteria for severe bearing damage are not defined unambiguously, and furthermore, the criteria are most propably application dependent. In addition, a similar expected bearing lifetime estimate as given in Eq. (1.6) is not introduced for EDM energies (Tischmacher and Gattermann, 2010). Nevertheless, based on the above discussion and the assumption that the level of a severe bearing damage is defined by the melting or vaporization level of the bearing raceway, an example of a 6309 ball bearing (45x100 mm) can be given, where the contact areas of both the inner and outer raceways are entirely vaporized. The width of the contact area at the bottom of the raceways is set to 1 mm and the total length of raceways is 0.46 m, resulting in A = 456 mm^2 for the total area to be vaporized. In addition, the capacitance of an energy storage is set to C_{tot} = 3.5 nF. Thus, the required U'_b levels for different sizes of craters can be calculated. The time required to entirely vaporize a given area in the case of different EDM activity values and U'_b levels is shown in Fig. 1.10. Further, it is pointed out that at the motor start-up, the EDM discharge activity levels are reported to reach values up to a range of 10^4/s (Muetze et al., 2010). Thus, the bearings of motor drive systems under cyclic operation would become subject to severe bearing degradation in a matter of days. In addition, the effect of deviation in U'_b on the time needed for

vaporizing the entire surface area can be demonstrated by an example where the required time is roughly doupled when U'_b drops from 9 V to 3.2 V at EDM activity = 200/s, which might well be the case in the real world.
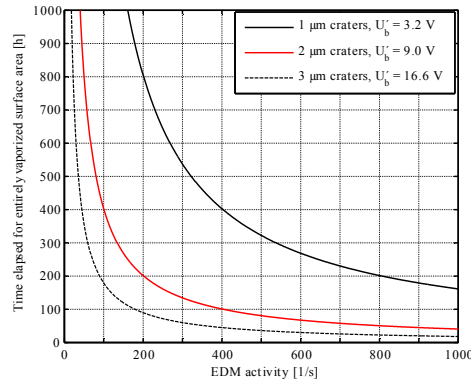
Fig. 1.10. Time required to entirely vaporize or melt a surface area of $A = 456$ mm^2 as a function of EDM activity in the case of different U'_b levels (crater size).

1.1.5 Origin of rotor-to-ground currents (RGC) and circulating bearing currents (CBC)

Yet another distinguishable source of bearing currents is common-mode medium-frequency (MF) and high-frequency (HF) ground currents. These currents flow through C_{wf} thus resulting in MF and HF stator winding-to-ground currents $I_{wf,MF}$ and $I_{wf,MF}$ (later $I_{wf,MF+HF}$). In the case of radial flux motors, these currents couple inductively to the rotor inducing a voltage between the rotor ends of the motor. A balancing current is likely to flow in the lowest impedance path, resulting in CBC (Muetze and Binder, 2007a). In addition, in the case of a poor grounding of the frame, the voltage difference between the frame of a motor and the ground can also cause rotor-to-ground currents (RGC). This is especially the case when the shaft coupler between a transmission system and a motor is not insulated. At this point, the ratio of impedances of different grounding media determines the proportion of the grounding current that flows as an RGC. When the shaft coupler between the driven motor and the rotor is insulated or the load has no galvanic connection to the ground, in other words, the load device is not supported by additional bearings, CBC becomes the most dominating bearing current type in terms of aging impact in large-size motors. In (Muetze and Binder, 2007a; Muetze and Binder, 2007c), it is proposed that the numerical value of the induced shaft voltage U_{shaft} between the DE and NDE bearings can be estimated through the dependency on the stator length

$$U_{\text{shaft}} \approx I_{\text{wf,MF+HF}} \cdot l_{\text{s}}, \tag{1.11}$$

where l_{s} is the length of the stator core (Muetze and Binder, 2007a). It is pointed out that the dependency shown in (1.11) is not an equation but a dependency derived from multiple equations studied in (Muetze and Binder, 2007b) and is based on an assumption that the dimensions and capacitances of the motors are scaled in the same ratio with the stator length.

1.1.6 Circulating bearing currents (CBC)

As proposed in (Muetze and Binder, 2003; Muetze and Binder, 2007; Chen et al., 1996; Bell et al., 1998), when considering motors with frame sizes of $H_{\text{f}} \geq 280$ mm, EDM currents are assumed insufficient to cause damage to the bearings because $C_{\text{tot}} = C_{\text{wr}}+C_{\text{b,de}}+C_{\text{b,nde}}$ of the motors does not increase in the same ratio as the Herzian area in the bearings. In the case of large motors, the increment of the significance of CBC in terms of bearing aging impact can be described by the cause-effect chain when moving upwards in motor sizes.

1. It is assumed that the area between the stator frame and the windings increases along with an increase in the frame size, resulting in an increment of C_{wf}.
2. The magnitude of $I_{\text{wf, MF+HF}}$ increases because of the low-impedance path provided by the increased C_{wf}.
3. The magnitude of the circular HF magnetic flux increases because of an increase in the magnitude of $I_{\text{wf, MF+HF}}$.
4. An inductive coupling occurs between the stator frame and the rotor, similarly as in the case of an HF transformer.
5. A voltage difference U_{shaft} is generated between the bearings by an induction phenomenon.
6. A balancing current flows through bearings causing CBC.
7. When the frame size is in the range of $H_{\text{f}} \geq 280$ mm, the induction voltage is sufficient to produce a balancing current magnitude that may degrade the bearings.

The cause-effect chain of the CBC phenomenon is shown in Fig. 1.11 and an equivalent circuit model in Fig. 1.12.
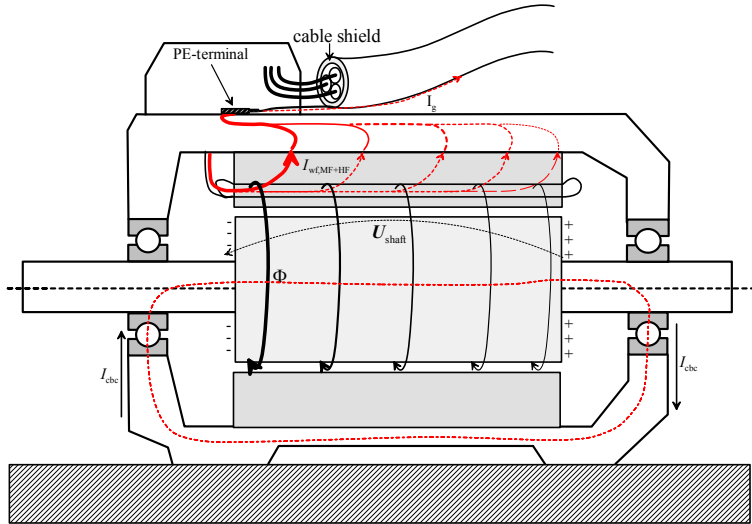
Fig. 1.11. CBC mechanism, where the high du/dt components of the input voltage waveform are flowing through C_{wf} as $I_{wf,MF+HF}$ thereby generating a magnetic flux that couples with the rotor. As a result, there is a voltage difference between the DE and NDE of the rotor caused by the induction phenomenon. A balancing current is about to flow in the lowest impedance path as CBC through the bearings.
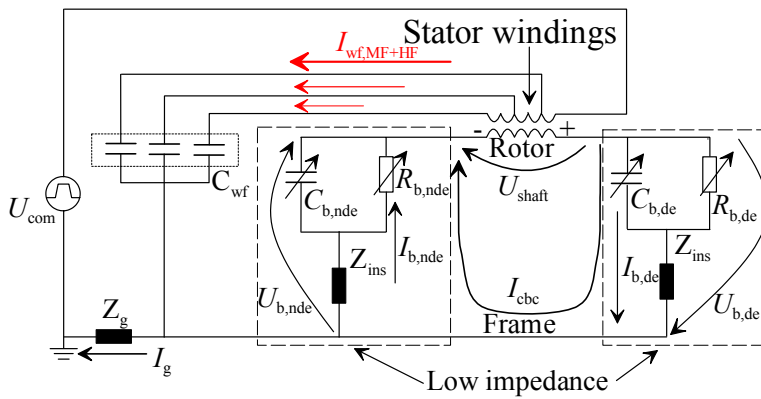
Fig. 1.12. Equivalent circuit of the CBC. $R_{b,de}$ and $R_{b,nde}$ represent the bearing resistances. In addition, Z_{ins} are impedances caused by a motor modification such as a bearing insulation.

Because of the different coupling method compared with EDM, CBC can typically generate significant current magnitudes considering their aging impact in LVSCIMs for motor sizes $H_f \geq 280$ mm, which commonly correspond to motor power ratings of $P_n \approx 75$ kW and above (Guttowski et al., 2006; Muetze and Binder, 2003). Several authors have agreed that the highest I_{cbc} magnitudes occur at slow rotation speeds $n < 500$ rpm and when the bearing operating temperatures are $70\,°C \leq T_b \leq 80\,°C$

(Muetze and Binder, 2003; Muetze, Binder, 2006; Tischmacher et al., 2010). This is understandable because at low speeds and high temperatures, the oil film inside the bearings is likely to be thin enough to enable sufficient I_{cbc} for bearing aging (Tischmacher et al., 2010). For example, in (Muetze and Binder, 2006; Muetze and Binder, 2007a), up to $|\hat{I}_{cbc}| = 20$ A value is reported in a certain operating point in a motor $P_n = 500$ kW.

1.1.7 Rotor-to-ground currents (RGC)

In (Guttowski et al., 2006; Muetze and Binder, 2003; Muetze and Binder, 2007), it is stated that an RGC occurs usually in poorly grounded systems. This current type is present in cases where the rotor is connected to the earth potential through a lower impedance than the stator housing. Regardless of the motor size, the magnitude of I_{rgc} may reach significant levels, thereby substantially accelerating bearing aging. In addition, I_{rgc} is stated to excite a CBC mechanism, because a low-impedance path for $I_{wf,MF+HF}$ is available. The cause-effect chain of the RGC phenomenon is shown in Fig. 1.13, and an equivalent circuit model in Fig. 1.14. Figure 1.14 represents the worst case; the highest RGC magnitudes are present in an electric drive system that has no proper grounding medium from the motor frame to the ground, and thus, only an incipient frame-grounding current I_{fg} occurs.
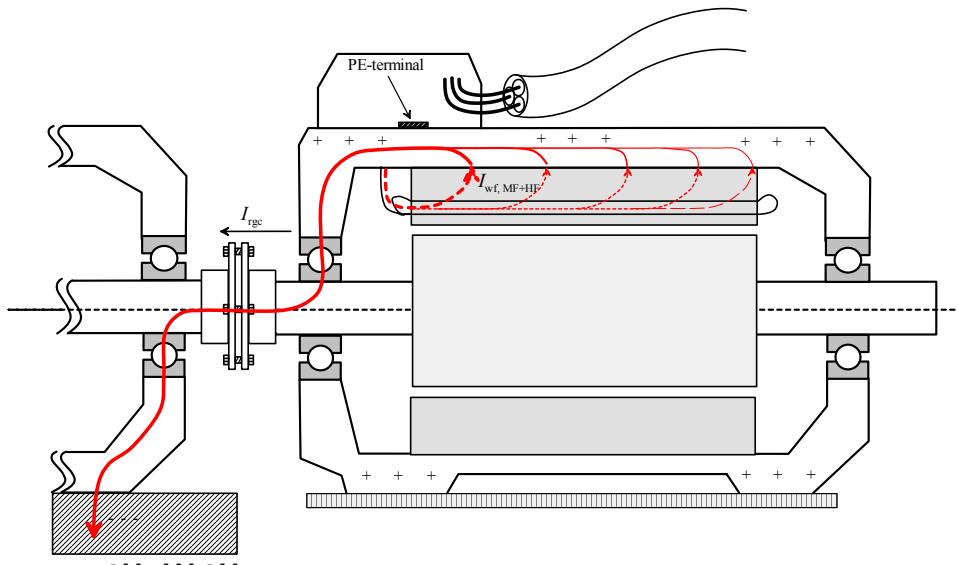
Fig. 1.13. RGC mechanism where the motor is electrically "floating" compared with the ground potential as a result of a poor grounding of the frame of the motor. As a consequence of the poor grounding, the high du/dt components of the input voltage waveform are flowing through C_{wf} as $I_{wf,MF+HF}$, and further, as a balancing current, which is about to flow in the lowest impedance path to the ground, in this case as RGC through the DE bearing.

Fig. 1.14. Equivalent circuit model of the RGC. The lowest impedance path for the balancing current goes through the bearing(s) of the motor and the bearing(s) of the load machine. The motor frame is "floating" compared with the ground potential because of the improper grounding indicated by the high impedance Z_{fg}.

1.1.8   Harmful CBC densities

In (Muetze, Binder, 2007; Stack et al., 2003), it is shown that CBC can significantly reduce the lifetime of a bearing. CBC flows through a relatively small conductive area, and therefore, in certain operating conditions, it is capable of producing a current density that is sufficient enough to cause damage to the bearings. In the galvanic conductive area, electrical energy is converted into heat, thereby causing melting and fluting on the bearing raceways and eventually, a bearing failure. It is worth noticing that even if a galvanic connection occurs, $R_b \neq 0$, and thus, because of the RI^2 losses, melting is likely to take place. This applies especially when considering substantially small conduction areas (areas in the range of mm^2) to which the generated heat dissipates. In (Busse et al., 1997c), it is stated that the aging impact of CBC, the waveform of which is typically sinusoidal, should be analyzed with respect to its $J_{b,rms}$ value rather than the $\hat{J}_b$ value, and $J_{b,rms} \leq 0.56$ A/mm^2 is given as the safe operating limit for sinusoidal current. Unlike EDM, the magnitude of CBC can be estimated as a function of ground current I_g. This is because I_g contains $I_{wf,MF+HF}$ that causes U_{shaft} and leads to the generation of CBC. Based on this, dependencies for the approximation of the magnitude of CBC with different bearing configurations are listed in Table 1.2. Further types of insulated bearings are discussed in section 1.2.2.

Table 1.2. Magnitudes of CBC as a function of I_g in different bearing configurations of an LVSCIM (Muetze and Binder, 2007).

Type of bearings	Peak current
Two conventional bearings	$I_{cbc,max} < 0.4 \cdot I_{g,max}$
One insulated bearing	$I_{cbc,max} < 0.2 \cdot I_{g,max}$
Two insulated bearings	$I_{cbc,max} < 0.1 \cdot I_{g,max}$
One or two hybrid bearings	$I_{cbc,max} \approx 0$

Alternatively, according to (Muetze et al., 2006), the aging impact of CBC can be approached by estimating the total energy dissipated in the bearing. It is proposed that the analysis can be executed by calculating the bearing stress

$$W_{b,tot} = J_{b,rms} \cdot t_{op} \cdot f_{sw} \,. \tag{1.12}$$

It is stated that the introduced bearing stress is proportional to the electrical energy dissipated in the bearing (Muetze et al., 2006). Further, it is concluded that when $W_{b,tot} = 6 \cdot 10^9$ in all the tested bearings (6209-C3, 6309-C3 and 6308-C3), the whole surface of the bearing raceway has melted at least once. However, the value of $W_{b,tot}$ at which the bearings could be considered severely damaged is not clearly indicated in the paper. It is also pointed out that Eq. (1.12) for the estimation of the total dissipated energy assumes that the current with a fixed magnitude flows through the bearing during each switching. Basically, this limits the applicability of the equation to CBC and cases where the bearings are operating under conditions discussed in section 1.1.6.

1.1.9   Characteristics of bearing lubricants

In (Busse et al., 1997a; Tischmacher et al., 2010), it is stated that the thickness of an oil film is a function of grease viscosity, temperature, motor speed, and bearing loads. An analytical approach to estimate the minimum oil film thickness is also proposed in (Busse et al., 1997c). (Tischmacher et al., 2010) continues that the oil film acts as a dielectric material between the rolling elements and raceways of the bearing, thus forming a capacitor. The lubricant grease plays an essential role when considering the bearing current magnitude and frequency of occurrence. In (Tischmacher et al., 2010), the influence of the rotating speed on the bearing capacitance is also studied. It is stated that within a temperature range of 20 °C $\leq T_b \leq$ 40 °C, the capacitance of the bearing remains constant in the whole rotation speed range (20 $\leq n \leq$ 3000 rpm), resulting in a conclusion that there is no significant change in the oil film thickness. However, in the temperature range of 60 °C $\leq T_b \leq$ 80 °C, the rotation speed has a significant influence on the oil film thickness and the bearing capacitance. It can also be stated that at low rotating speeds, 20 $\leq n \leq$ 40 rpm, and in the temperature range from T_b = 40 °C to T_b = 80 °C, the oil film thickness is almost zero, and hence, a metallic contact is introduced. As a result of the studies dicussed above, three different operating modes for bearings are introduced. These modes are insulated, discharge, and ohmic. It is pointed out that the studies are performed with a bearing that is assembled on a separate

platform instead of a motor (Tischmacher et al., 2010). Further, (Gostabile et al., 2007) studies how different conditions affect the dielectric characteristics of lithium-thickened lubricant greases used in bearings. Three different types of lubricants are tested. The test results are collected in Table 1.3, where the values of ε_r are determined with a sinusoidal signal. A further breakdown voltage $U^{'}$ is determined with a square wave signal and a discharge distance of 0.175 mm. It is pointed out that since the test setup is a point-to-plane platform, the influence of the rotation speed and the viscosity of the lubricant are excluded from the study.

Table 1.3. Electrical properties of different types of bearing lubricants.

	Paraffinic mineral oil	Highly refined mineral oil	Hydroxystearate
Thickener	Lithium	Lithium	Lithium
$\varepsilon_{r(1\ kHz)}$	5–10 (30–90 °C)	2.2–2.4 (30–90 °C)	3.1–3.3 (30–90 °C)
$\varepsilon_{r(100\ kHz)}$	2–4 (30–90 °C)	1.8–2 (30–90 °C)	2.4–2.5 (30–90 °C)
$U^{'}_{(1\ kHz)}$	1.4 kV	-	-
$U^{'}_{(10\ kHz)}$	1.5 kV	> 3.0 kV	2.4 kV

1.1.10 Aging impact of a running-in phenomenon

Misalingment between the bearing parts and the surface roughness occur in new bearings. The initial surface roughness of a new bearing can be reduced by polishing the raceways of the bearings before taking them into use. However, such a procedure is too expensive to apply in practice. In (Rao et al., 1981), it is suggested that a running-in procedure of bearings should be performed before placing the bearings under stress. It is shown that misalingments and roughness of the raceways are removed within four hours of the running-in procedure. In (Tischmacher and Gattermann 2012b), it is reported that the roughness of the bearing raceways increases the discharge activity (DA). It is also suspected that additional DA induced by the initial roughness of raceways might be sufficient to produce incipient defects, which are significant enough to excite DA and lead to fast development of a bearing failure. Therefore, it is argued that an incorrect running-in procedure significantly decreases the lifetime of bearings. However, to the author's knowledge, the topic is not studied in detail, and further tests are recommended. DA is discussed in more detail in section 1.3.1.

1.2 Bearing current mitigation techniques

Because of the many benefits provided by a conventional two-level VSI, alternatives to replace the device are considered unnecessary or unprofitable. Consequently, also the root cause for bearing currents in an LVSCIM will remain. However, in order to alleviate the side effects caused by the VSIs, several bearing current mitigation techniques have been studied and implemented in a large number of publications

(Saunders et al., 1996; Guttowski et al., 2006; Wu 2006; Muetze and Binder 1997; Bell et al., 1998; Muetze and Binder, 2003; Muetze and Binder, 2006; Muetze et al., 2007; Akagi and Tamura, 2006; Shah et al., 2011; Schweitzer and Maslen, 2009). Each technique has advantages and restrictions of its own. In this section, different mitigation techniques to decrease the magnitude of a certain type of bearing currents are introduced in brief, and the advantages and disadvantages of each technique are summarized. Table 1.4 lists a number of bearing current techniques.

Table 1.4. Summary of different kinds of bearing current mitigation methods.

Mitigation method	Small capacitive currents	EDM currents	Rotor-to-ground currents	Circulating bearing currents
Shielded cable			X	
Sinusoidal filter*				X
Common-mode choke*			X	X
Passive du/dt filter*			X	X
Passive du/dt reactor*			X	X
Insulated bearing	X	X	X	X
Hybrid bearing		X	X	X
Shaft DC grounding	X	X		
Modulation scheme	X	X	X	X
Insulated shaft coupler			X	
Conductive shaft coupler**	X	X	X	X
Low-impedance connection between the frames of the driven motor and the load			X	
Conductive lubricant		X		
Electrostatic shielding***	X	X		
Magnetic bearings	X	X	X	X

*No connection to the DC link of the VSI;
** reduces the current through an individual bearing;
*** tested only for EDM

1.2.1 HF signal magnitude reduction at the motor terminals

A cost-effective solution to reduce the magnitude of U_{com} can be achieved by applying an appropriate modulation scheme that affects the charasteristics of the supply signal waveform of the conventional two-level VSI. To this end, reduced common-mode voltage pulse width modulation (RCMV PWM) techniques are introduced. By these techniques, U_{com} can be reduced from U_{dc} to $\pm U_{dc}/6$. The difference between these methods compared with conventional PWM methods is that zero voltage vectors are avoided. Unfortunately, a disadvantage of such modulation techniques is the increased current ripple (Hava and Un, 2009; Cetin and Hava, 2009; Cacciatto et al., 2007; Cacciato et al., 2009; Cacciato et al., 2013). An advanced approach is to apply a multilevel inverter, where each output voltage level can be achieved by multiple

switching combinations. This way, it is possible to decrease the magnitude and number of high du/dt common-mode pulses at the motor input by selecting the most feasible switching combinations. This mitigation technique is applicable in practice only to new motor drive installations (Guttowski et al., 2006; Wu 2006). In addition, in most of the cases, the acquisition cost of a multilevel VSI becomes a problem. In general, we may assume that the switching frequencies are probably growing, thereby contributing more to du/dt events that may generate bearing currents. Furthermore, it is pointed out that in the case of CBC and RCG, not only the magnitude but also the frequency content of the common-mode voltage is an important factor. In the case of EDM, parasitic capacitances are likely to be charged even if the frequency content of U_{com} were reduced. Another way to reduce the HF content of a motor input is to apply an appropriate filter. Several filtering techniques are studied in (Guttowski et al., 2006; Muetze and Binder 1997; Muetze and Binder, 2003; Muetze and Binder, 2006). It is shown that a du/dt filter significantly reduces the I_{rgc} and $I_{wf,MF+HF}$ currents. Although the du/dt filter reduces the HF content of the motor input signals, according to (Muetze and Binder, 2006), a disadvantage of this mitigation technique is its high acquisition cost. Moreover, a passive filter that has no connection to the DC link of a VSI does not have a significant influence on the EDM-type bearing currents, since the filter does not eliminate the common-mode voltage. However, in a special case reported in (Akagi and Tamura, 2006), a passive EMI (electromagnetic interference) filter is introduced, which applies motor windings as a part of the filter. The filter produces a significant reduction in the EDM bearing current ratings, although the condition requirement for this filter to operate efficiently is that the motor has to be ungrounded. A disadvantage is that this requirement may excite an RGC depending on the grounding on the load side. Noteworthly, passive filtering of the motor input signal is also caused by a supply cable between an inverter and an induction motor. The effects of different types of supply cables on the signal waveform at the motor terminals are measured and discussed in (Shah et al., 2011). Again, according to (Muetze and Binder, 2003), the use of a shielded supply cable lowers the stator grounding impedance thus reducing the RGC. Based on tests, it is found that a shielded cable actually excites a CBC because of its lower grounding impedance compared with a nonshielded cable. This is because of an increment of the $I_{wf,MF+HF}$ magnitude. As noted above in Table 1.2, $I_{g,max}$ is shown to have an impact on the magnitude of I_{cbc}. (Saunders et al., 1996; Muetze et al., 2007) extend the studies regarding the effect of electrically short and electrically long motor supply cables. It is proposed that the critical cable length l_c can be estimated according to the rise time of the voltage t_r and the signal propagation speed v_{cable} in the cable

$$l_c = 0.5 \cdot v_{cable} \cdot t_r. \tag{1.13}$$

A cable that is longer than the defined critical length may increase the overshoot of the common-mode voltage at the stator windings of a motor, thereby increasing the magnitude of U_b. (Saunders et al., 1996) provides a deeper insight into the transmission line theory and the generation and effects of the standing wave phenomenon on the voltage waveforms at the motor terminals. In addition, (Saunders et al., 1996; Hyypio

1997; Mercier and Cooper, 1999) discuss the effect of the standing wave phenomenon. The basic principle is that the longer is the cable, the higher is the voltage peak value. However, it is pointed out that the supply cable acts as a low-pass filter (LPF), and thus, the higher signal components are attenuated in the case of a longer cable compared with a shorter one thus the reducing peak value of the voltage. Furthermore, it is stated that in the case of a longer cable, $I_{g,max}$ is also reduced (Muetze et al., 2007). Again, an increment in the magnitude of I_g is shown to excite a CBC. Based on that, for an electrically long cable, when $\mathrm{d}u_{Lg}/\mathrm{d}t > 0.5$ kV/µs (where u_{Lg} is the line to ground voltage of the supply signal), we may write (Muetze et al., 2007a)

$$I_{g,max} \leq 1.5 \cdot 2/3 \cdot \mathrm{d}u_{Lg}\big/\mathrm{d}t \cdot C_{wf}, \tag{1.14}$$

and for an electrically short cable

$$I_{g,max} \leq 1.5 \cdot \mathrm{d}u_{Lg}\big/\mathrm{d}t \cdot C_{wf}. \tag{1.15}$$

Further, for $\mathrm{d}u_{Lg}/\mathrm{d}t \leq 0.5$ kV/µs and an electrically short cable

$$I_{g,max} \leq 2 \cdot \mathrm{d}u_{Lg}\big/\mathrm{d}t \cdot C_{wf}. \tag{1.16}$$

As a conclusion, when considering the selection of a supply cable, the question comes down to the value of C_{wf} of the motor and the type of the bearing current that has to be mitigated.

1.2.2 High-impedance bearings

The functioning of insulated bearings is based on a 50–250 µm thick aluminum oxide layer. The insulation provides resistive and capacitive impedance thereby decreasing bearing currents. In (Muetze and Binder, 2003; Bell et al., 1997), it is stated that insulated bearings reduce all four sorts of bearing currents. For example, if both bearings of the motor are insulated, a <40% reduction in EDM bearing currents can be achieved. It is worth noting that in order to prevent EDM currents, all of the bearings that have a galvanic coupling to the shaft of the driven motor have to be insulated. Otherwise, all discharges will be concentrated on the noninsulated bearing thus shortening its life dramatically. CBC can be mitigated with one insulated bearing. Different bearing assemblies and their influence on the CBC have been studied in (Muetze and Binder, 2007). A special case of insulated bearings is hybrid bearings, which have ceramic rolling elements and aluminum oxide insulation combined. Hybrid bearings are reported to suppress CBC, RGC, and EDM completely. However, because of the complex structure of the bearing, the acquisition cost of such bearings is significantly higher than that of conventional ones. This makes insulated bearings a more preferable choice for larger motors (Muetze and Binder, 1997; Bell et al., 1998). Hybrid bearings are recommended only with small motor sizes up to $P_n \leq 1$ kW, and

especially for new motors, when the manufacturer installs the bearings (Muetze and Binder, 1997). The ultimate solution for bearing currents is the use of magnetic bearings. According to (Schweitzer and Maslen, 2009), this bearing type does not rely on conventional bearings during normal operation at all. In normal operation, the shaft of the motor is levitated by a magnetic field. Disadvantages of magnetic bearings are their high acquisition costs, complex structure, and control system.

1.2.3 Impedance between a motor and a load

An insulated shaft coupler can be used to reduce the current flow through the bearings at a load machine or a mechanical transmission system. In other words, it eliminates the RGC. A disadvantage of this method is that it does not necessarily reduce currents in the bearings of a driven motor and may even increase bearing currents by blocking one current path. It is also pointed out that nonconductive material between the shaft coupler plates is not applicable in all cases (Guttowski et al., 2006; Muetze and Binder, 2003; Muetze and Binder, 2007; Muetze and Binder, 1997). A typical reason is the weak mechanical resistance compared with metal shaft couplers. Additionally, a conductive shaft coupler between a motor and a load can be used to reduce the magnitude of bearing currents in an individual bearing. Moreover, it may remove the EDM problem, since more bearings are likely to be involved in the system, and a lubrication film may not be present in all of the bearings. Nevertheless, the number of bearings under the influence of bearing currents is increased, and in some cases, more maintenance is required. Furthermore, because of the possibility of RGC, (Guttowski et al., 2006) notes the feasibility of a low-impedance connection between a motor frame and a frame of a load. This method makes it possible to reduce the RGC to half of the original value. The method is based on an experimental case where the voltage difference between the frame of the driven motor and the load was reduced by an additional low-impedance path between the frames. A disadvantage is the limited shaft length of the connection between the driven motor and the load. It is also worth bearing in mind that an increased I_g excites a CBC.

1.2.4 Methods to eliminate U_b

The conductive properties of a lubricant can be increased by additional substances such as graphite. In (Guttowski et al., 2006), it is proposed that the use of a low-resistive grease would most probably decrease the EDM activity. However, in the case of a low-resistive grease, according to (Busse et al., 1997b), current magnitudes ranging from $\hat{I}_b = 267$ mA, which corresponds to $I_{b,rms} = 189$ mA in the case of a sinusoidal signal (it is proposed that it is indeed I_b not J_b), are sufficient to cause decomposition of the lubricant grease into lithium iron oxide. This has a negative effect on the lubrication properties of the grease, thereby increasing mechanical wear and eventually leading to a bearing failure. It is also pointed out that the use of a low-resistive grease causes corrosion. This is due to the electromechanical reaction between the metal surface and the low-resistive grease. Even though the availability of a low-resistive grease has

somewhat improved since the publication of (Bell et al., 1998), some of the above-mentioned problems are still remaining. The problem that the conductivity of the grease is lost over time is verified by experimental tests, where the conductivity of a synthetic-oil-based low-resistive grease was lost after t_{op} = 40 h of operation. It is suggested that the main reason for the lack of conductivity is the deformation of the substances so that the conductive substance will be displaced from the ball path. Unfortunately, restoration of conductivity, which would have had a major influence in the case of a motor in cyclic operation, was not reported (Tischmacher and Gattermann, 2012a). An alternative approach to reduce U_b is to apply a shaft grounding brush. This bearing current mitigation method provides a low-impedance grounding parallel to the motor bearings. In (Guttowski et al., 2006; Bell et al., 1998), also several disadvantages are reported; the grounding brush requires maintenance and may excite circulating bearing currents. This is due to the low-impedance path for current from the rotor to the ground. Obviously, mitigation of the effect of CBC on the bearing would require grounding brushes in the proximity of both bearings, or a combination of multiple mitigation methods such as an insulated bearing on the one side and a conductive brush on the other. Alternatively, a maintenance-free solution for new motors is introduced in (Bell et al., 1998; Akagi and Tamure, 2006), where an electrostatic shielded induction motor (ESIM) is discussed. The method is based on a nonmagnetic shield structure installed onto the windings in the air gap between the stator windings and the rotor, thereby reducing the capacitive coupling between the stator windings and the rotor and causing reduction in the rotor-to-ground voltage. This method effectively eliminates EDM currents. However, the performance of the bearing current reduction method in the case of CBC is not reported.

1.3 Bearing current measurement techniques

Several measurement methods for acquiring the magnitude of bearing currents in a certain motor have been introduced and tested for example in (Muetze and Binder, 2003; Muetze and Binder, 1997; Särkimäki 2009; Ahola et al., 2010). The common test setups are based on measurements that require an intrusive connection between the motor and the measurement device. Typically, for instance insulated bearings and conductive brushes are used to attach the measurement probe to a motor. Additional bearing test platforms are also applied (Tischmahcer et al., 2010). Alternatively, a more applicable nonintrusive RF-signal-based method to detect bearing current activity in the case of EDM currents is introduced in (Särkimäki, 2009). However, thus far, it is applied only for the detection of EDM-type bearing currents and further studies on the DA in (Muetze et al., 2010; Ahola et al., 2010). It is yet uncertain whether bearing current magnitudes or discharge energy can be estimated by measurements made by the RF-signal-based bearing current detection method (RF-SBBCDM). This is partly due to the lack of several radio channel and transmitter circuit parameter values.

1.3.1 Nonintrusive bearing current detection and measurement methods

Rokowski coil can be applied for nonintrusive current measurements. The design and applicability of the coil are discussed in (Ray and Davis, 1999; Hewson et al., 2006). In the RGC measurement, Rokowski coil couples with the magnetic field that is formed by a current flowing on the shaft that connects the driven motor to the load. Advantages of the probe are that it does not saturate because of the air-core structure, and consequently, the dynamic range of the probe is wide. For example, the same probe can be used in measurements where for instance signal magnitudes in the range of 100 A or 100 kA are present. Because the coil does not have a core made of magnetic material, it has better linearity in the frequency domain than a probe that has a magnetic core. The most problematic bearing current type from the nonintrusive measurement point of view is EDM bearing currents. As can be concluded from Fig. 1.8, measurements on EDM bearing current are difficult to conduct. This is because the current does not exit the motor but discharges energy in the capacitance within the motor. Unlike in the RGC or CBC, there is no reference signal that would be practical to measure intrusively without modifications to the motor. This can be seen in Fig. 1.15, where the common-mode current from the PE cord is measured simultaneously with EDM. Fortunately, in (Särkimäki, 2009), the RF-SBBCDM is introduced and tested. A decaying RF pulse generated by EDM is received as a signal pulse U_{RF} from the motor. In this method, radio wave propagation is introduced and applied; the signal is received in far-field conditions. However, it is stated that so far the method is applicable to EDM bearing currents only. For a motor involved in the test setup described in (Särkimäki, 2009), the power of the transmitted signal is measured to be concentrated around 200 MHz. Therefore, the measurement is performed in the frequency range of 100–400 MHz. One benefit that follows from the measurement band selection is the frequency span that is almost free of telecommunication interference. The detection method is based on a hypothesis that a small fraction of energy discharged during EDM is transmitted as an RF signal. It is found that the average power of the received signal is $12 \text{ mW} \leq P_r \leq 49$ mW, when the total charged energy in the motor is 245 nJ. In (Särkimäki, 2009) it is pointed out that the operation of a motor as a transmitting antenna is not studied in full detail. However, some estimations on the motor performance as an antenna, for example the gain and the radiation pattern, are provided. It is also suggested that unlike in the performed tests, an anechoic chamber should be used for true antenna radiation pattern measurements.
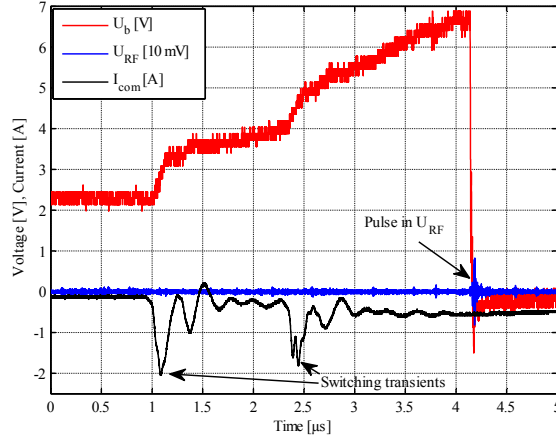
Fig. 1.15. Simultaneous measurement of I_{com}, U_b and U_{RF} for EDM; The example is taken from a conventional series production (not modified) P_n = 5.5 kW, six-pole LVSCIM. The other equipment of the measurement setup equipment is listed in Table A1 (Appendix A). In the figure, the associated U_{RF} signal is received at the moment of an EDM discharge. The switching events do not generate detectable RF emission, nor an EDM discharge can be detected by I_{com} measured from the PE cord.

The uncertainty in the dependency between the discharge energy and the received RF signal power is most probably due to several reasons; for example, in the far-field region and free space, the impedance of the electromagnetic wave is fixed, Z_0 = 377 Ω. This is independent of the ratio of the magnitudes of voltage and current by which the RF signal is generated. Thus, a similar signal strength can be received without a possibility of noticing the difference in the ratio of initial signals. Furthermore, it is also worth remembering that only the real part of the electric and magnetic fields can be radiated as an RF signal. Thus, a possible phase shift between the voltage and current vectors and thereby between the electric and magnetic fields, E ang H, respectively, has an effect on the radiated signal as given in the time-averaged power density vector

$$S = \frac{1}{2} Re\left(E \times H^*\right),$$ (1.17)

where H^* is the complex conjugate of H. Hence, a deviation in the impedance in the transmitter circuit has an effect on the current magnitude and phase compared with voltage. These aspects may cause uncertainty to the measurement when only the initial current or voltage waveform causing the RF signal is studied (Barclay, 2013; Harish, Sachidananda, 2007; Balanis, 2005).

When considering EDM DA studies, a disadvantage in the measurement system introduced in (Särkimäki, 2009) is its limited memory capacity. Hence, the pulse

waveform of the received pulses cannot be recorded for later analysis. In (Muetze et al., 2010), the applicability of the RF-SBBCDM is improved by adding a single trigger level discharge counter unit to the measurement system. Now, EDM DA values can be studied in different operating conditions. As discussed above, in (Muetze et al., 2010) RF-SBBCDM is applied only to EDM DA studies. It is found that DA can be excited by changing the operating parameters. In (Ahola et al., 2010) it is also suggested that bearing diagnostic might be possible according to the DA characteristics of a motor. A disadvantage of the RF-signal-based measurement method is that only one signal trigger level can be applied at a time in the current measurement setup. Consequently, studies considering the magnitude level distribution of EDM are far beyond the capabilities of the current measurement system. In (Tischmacher and Gattermann, 2012b), an intrusive measurement system for studies on EDM pulse magnitude distribution is applied. It is shown that the DA of EDM pulses that are considered harmful tends to increase according to the state of the bearing wear, which is determined by an accelerometer-based reference measurement. In addition, it is pointed out that the aging impact of EDM bearing currents should not be evaluated by the DA only but as a combination of the DA and the magnitude distribution of the discharge energies. Again, it is noted that in general, the electric field stress generated by a square wave voltage that the lubricant film is capable of withstanding is approximately $1 \text{ kV/mm} \leq U' \leq 30 \text{ kV/mm}$ depending on the applied lubricant (Busse et al., 1997b). Hence, after surpassing this electric field strength threshold level, the DA is likely to increase significantly. It is pointed out that the studies are performed with a bearing that is assembled on a separate platform.

1.4 Motivation of the work

A common reason for the unpopularity of a certain bearing current mitigation method such as insulated bearings is their high investment costs. Moreover, some of the bearing current mitigation methods such as conductive brushes may lose their functionality, which calls for monitoring and maintenance. When a complete solution for the bearing current problem is considered unaffordable to be implemented, proper measurements for the monitoring or determination of a correct countermeasure come into question. Unfortunately, implementation of most of the bearing current measurement methods requires modifications to the system to be measured, and possibly, an intrusive coupling even to the rotating parts of the motor. The applicability of intrusive measurement methods may be limited to periodically executed measurements or laboratory tests. In addition, it is possible that the operating conditions or the system configuration do not necessarily correspond to the normal operating conditions of the motor. Consequently, a comprehensive view on the distribution of the measured quantities may not be acquired, which may lead to wrong conclusions in terms of the aging impact. Furthermore, the cost of the required measurement instrumentation can be too high to reserve a measurement unit of its own for every motor under monitoring. This leads to a conclusion that because of the nonlinear aging mechanism, periodically executed

measurements may be ineffective in terms of failure-preventing condition monitoring and maintenance. A challenge related to the nonintrusive measurement and detection of EDM is due to the deviation in the time periods between the switching event(s) that charge(s) the rotor circuit and the following EDM discharge. Therefore, the conditions in which EDM occurs and the parameters that affect the current magnitude are difficult to estimate. Again, when considering CBC and RGC, the most typical conditions and the highest energy that can contribute to the generation of CBC are present right after the switching transient. Hence, determining the conditions of bearings at that very moment becomes crucial in terms of the CBC and RGC magnitude. To this end, effort should be put to enhance the feasibility of the measurements so that they could be executed in parallel with the normal operation of a series production motor. One approach is to apply nonintrusive measurement methods.

1.5   Research methods and objective of the work

This doctoral dissertation aims at investigating new methods by which the accuracy of the bearing current analysis can be improved, without a necessity of galvanic measurement probe coupling to the rotating parts of the motor or the electrical insulation of bearings. Thus, the work provides new knowledge of bearing currents and feasible methods to measure them online in field conditions. The hypothesis is that by the applied method, RF-SBBCDM, the occurrence of CBC and RGC can be detected without a mechanical coupling to the motor. This is done by verification of the dependency between the RF signal reception and the occurrence of the different bearing current types. To this end, the influence of the operating parameters on the electrical modes of bearings is studied by an intrusive bearing impedance measurement method, which is introduced in this doctoral dissertation. The study is considered crucial in order to gain understanding of the bearing impedance during the occurrence of different kinds of bearing currents. As a link to the RF-SBBCDM, which can be applied in parallel with the normal operation of a conventional VSI-driven LVSCIM system without the requirement of any modifications to the system, a transient activity (TrA) is introduced. Further, its relation to the discharge activity (DA) that is determined by the modified RF-SBBCDM (Muetze et al., 2010) is verified. Moreover, in order to improve the performance of the RF-SBBCDM, an electromechanical simulation model is built to study the motor operation as a transmitting antenna. With the knowledge acquired by these studies, the applicability of the RF-SBBCDM in the case of CBC and RGC is studied and verified. In addition, the applicability of the RF-SBBCDM is enhanced by very high-frequency (VHF) signal content studies in the case of EDM currents. Furthermore, a measurement probe based on a nonintrusive HF magnetic near-field (ni-HFMNFP) coupling is introduced, designed, and tested for the magnitude measurement of EDM bearing currents. In addition, the performance of the ni-HFMNFP is evaluated by comparing the measurement data with the reference measurement.

1.6   Outline of the work

The doctoral dissertation consists of an introductory section and the appended original publications. Figure 1.16 illustrates the relations between the chapters and the appended publications and shows the applied research methods. The figure also demonstrates how each publication responds to the research objectives. The contents of the introductory section are divided into six chapters as follows.
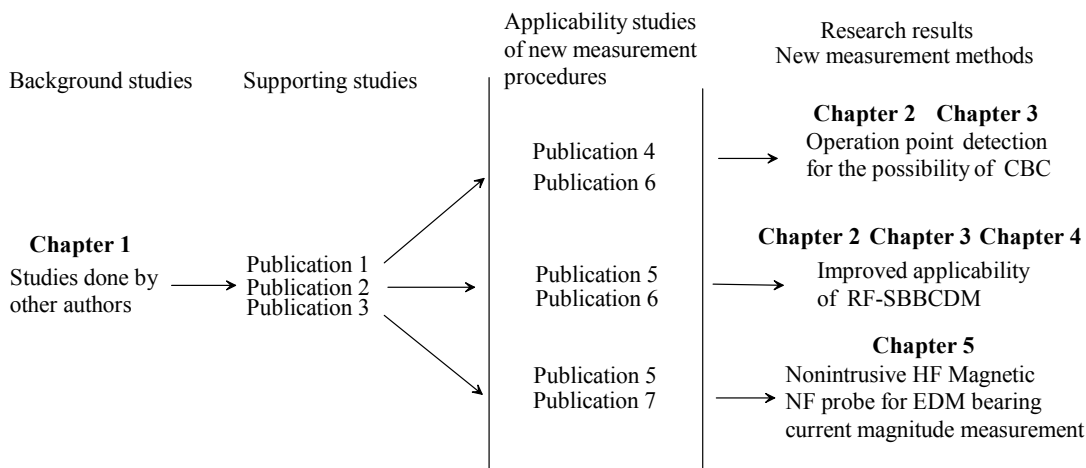

Fig. 1.16. Scheme of studies carried out in the doctoral dissertation, the applied methods and the publications linked to the context of the dissertation.

Chapter 1   addresses the bearing current phenomena, their impacts, and measurement and mitigation methods. The chapter also determines the outline and motivation of the doctoral dissertation and describes the content of the following chapters.

Chapter 2   provides verification and extension of the studies conducted on the bearing modes as proposed in (Tischmacher et al., 2010). In addition, the chapter introduces an intrusive but practical way to measure bearing impedance and bearing mode transients. The study provides basic knowledge on which the RF-SBBCDM and other RF-signal-based measurement methods can be based. The chapter provides new knowledge of the electrical bearing behavior and the initial requirements for the electrical conditions of bearings that the occurrence of EDM and CBC necessitates (Publications III and VI).

Chapter 3   focuses on the applicability studies considering the nonintrusive RF-SBBCDM to determine the operating mode and region of bearings and to detect the possibility of CBC (Publications IV–VI).

Chapter 4 introduces a new approach to study the functioning of a motor as a transmitting antenna for the RF signal. The method is based on the application of an electromechanical antenna simulation modeling approach adopted from the field of RF engineering and applied for the first time to electrical drive systems. The chapter provides the background and rationale behind the use of a motor as a signal transmitter. The chapter also expands the knowledge on the applicability of the RF-SBBCDM (Publications I and V).

Chapter 5 discusses the design, testing, and verification of the applicability of a ni-HFMNF coupling-based probe for the magnitude measurement of E DM current pulses (Publication V and VII).

Chapter 6 is the final chapter before the appended publications. In the chapter, conclusions and suggestions for future work are made.

A brief description of the contents of the publications comprising this doctoral dissertation is given, and the contributions of the author and the coauthors to the publications are reported in the following. The other coauthors not listed below have participated in the project cooperation. Furthermore, the coauthors have contributed to the preparation of the publications by revision comments and suggestions. These publications comprise three journal articles and four international conference papers.

Publication I addresses the application of discharge detection by using the propagation delay of the RF signal between multiple antennas of the receiving system. In addition, preliminary suggestions for the RF radiation pattern of a motor are given.

The manuscript was mainly written by Prof. Jero Ahola. The measurements were conducted in collaboration with Ville Niskanen, and further, the simulation model for the electromechanical transmitter antenna was designed and analyzed by Ville Niskanen. Suggestions, comments and part of the writing work of the manuscript were accomplished by Prof. Annette Muetze.

Publication II concentrates on the analysis of the detection of CBC and RGC by the RF-SBBCDM.

The manuscript was mainly written by Prof. Annette Muetze. The measurements and the measurement data analysis were mainly performed by Ville Niskanen. Suggestions for measurements and comments were given by Prof. Jero Ahola.

Publication III introduces an intrusive method to measure the impedance, mode transitions, and operating modes of bearing(s) as a function of several operating parameters.

The measurements and the measurement data analysis were mainly performed by Ville Niskanen. Prof. Annette Muetze was responsible for most of the writing work. Prof. Jero Ahola collaborated in measurements and gave suggestions for the paper.

Publication IV continues and deepens the studies on the detection of CBC by the RF-SBBCDM.

The publication was mainly written by Prof. Annette Muetze. The measurements and the measurement data analysis were entirely performed by Ville Niskanen. Prof. Jero Ahola gave suggestions and comments on the paper.

Publication V presents detailed studies on the RF signal radiation pattern simulations for the LVSCIM and verifications of simulations by measurements.

The entire simulation model procedure, measurements, and measurement data analysis were mainly performed by Ville Niskanen. Prof. Annette Muetze wrote most of the manuscript. Prof. Jero Ahola collaborated in measurements and gave suggestions for the paper.

Publication VI expands the studies on the bearing impedance behavior.

The measurements and measurement data analysis were performed by Ville Niskanen. Prof. Annette Muetze wrote most of the manuscript. Prof. Jero Ahola gave suggestions and comments on the paper.

Publication VII introduces a nonintrusive method to measure the surface current magnitudes of HF EDM pulses that are flowing on an end plate of a motor. The paper presents and tests a prototype of a nonintrusive HF magnetic near-field probe (ni-HFMNFP).

The probe design, construction, measurements, and measurement data analysis were performed by Ville Niskanen assisted by Dr. Antti Pinomaa. The manuscript was also written by Ville Niskanen. Prof. Jero Ahola gave suggestions for the probe design and final comments on the paper.

The author of this doctoral dissertation has also been the author or a coauthor in the following publications on closely related topics. However, these publications are excluded from the dissertation as they are considered to be outside the very scope of the doctoral dissertation.

Niskanen V., and Ahola J. (2011), "Implementing a clamp on wireless torque measurement system for rotating shaft applications (UI)," in *Proceedings of the 14th European Conference on Power Electronics and Applications (EPE 2011)*, Birmingham, UK.

Niskanen V., and Ahola J. (2011), "Modeling and verifying the characteristics of induction motor as transmitting antenna for inverter-induced bearing discharges," in *the Eighth International Conference on Condition Monitoring and Machinery Failure Prevention Technologies*, Cardiff, Wales, UK.

Ahola J., Niskanen V., Tamminen J., and Ahonen T. (2011), "Performance Evaluation of Radio Frequency Based EDM Bearing Current Detection Method," in *the Eighth International Conference on Condition Monitoring and Machinery Failure Prevention Technologies*, Cardiff, Wales, UK.

Niskanen V., Ahola J., and Lehtinen P. (2012), "Study of applicability of RF based measurement method for partial discharge detection in stator windings," in *the Ninth International Conference on Condition Monitoring and Machinery Failure Prevention Technologies*, London, UK.

Niskanen V., Ahola J., and Lehtinen P., (2013), "Verification of the applicability of an RF-signal-based detection method for partial discharges on inverter-fed random wound stator windings in a low-voltage induction motor," in *Proceedings of the 15th European Conference on Power Electronics and Applications (EPE 2013)*, Lille, France.

Romanenko A., Ahola J., Muetze A., and Niskanen V. (2014), "Study of incipient bearing damage monitoring in variable-speed drive systems," in *the 16th European Conference on Power Electronics and Applications (EPE 2014)*, Lappeenranta, Finland.

1.7 Scientific contributions

The main scientific contributions of this doctoral dissertation are:

- Study of the bearing impedance behavior in the time domain and introduction of an intrusive method for its measurement (Publications III–IV and VI).
- CBC aging impact estimation by measurements that can be carried out for a series production motor based on the application of a bearing impedance analysis.
- Introduction and application of numerical electromagnetic code (NEC) based antenna simulation software, adopted from RF engineering for studies on the transmitting antenna and radiation pattern characteristics in the case of a low-voltage squirrel cage induction motor (LVSCIM), (Publications I and V).
- Verification of the signal content dependency between EDM events and the received signal in the case of the RF-SBBDCM.
- Application of the RF-signal-based bearing current detection method (RF-SBBCDM) combined with the knowledge of the bearing behavior to determine the operating region of bearings and analyze the possibility of the occurrence of circulating bearing currents (CBC) with an aging impact (Publications II and V).
- Design, implementation, and verification of the operation of a nonintrusive HF magnetic near-field probe (ni-HFMNFP) for the measurement of the bearing current magnitude caused by electromagnetic discharge machining (EDM), (Publication VII).

2 Bearing impedance

Although considerable research efforts have been placed on bearing currents over the past few decades, comprehensive understanding of the aging mechanisms and parameters that have an influence on the bearing currents is still missing, judging by the suggestions made for further studies in (Tischmacher and Gattermann, 2010, Kriese et al., 2012; Muetze et al., 2010). It is understood that the electrical operation and characteristics of bearings play a crucial role when considering bearing currents. In addition to the fact that bearings are subject to wear, their electrical characteristics determine the kind and magnitude of bearing currents that may exist in a certain operating point in certain environmental conditions. In several publications, rotation speed and operating temperature are reported to have a significant effect on the oil film thickness and the voltage threshold level (Muetze and Binder, 1997; Muetze et al., 2010; Kriese et al., 2012). However, the electrical operation of a bearing is often studied from the perspective of the voltage threshold level of the bearing lubricant, and therefore, it is more probable that the key operating region limits of bearings are determined by the applied square wave voltage stress than by any other operating parameters. This may result in cases where the applied voltage stress values are likely to reach levels that may not occur in actual LVSCIM applications (Busse et al., 1997a; Busse et al., 1997b; Tischmacher and Gattermann, 2010). For the above reasons, it is thus advisable to study the electrical behavior of bearings in actual application conditions. To this end, in the test series conducted in this chapter, the voltage stress values $\hat{U}_b \leq 10$ V, are applied. These voltage stress levels occur commonly in LVSCIM drive systems. Furthermore, it is known that the bearing voltage and current signals related to CBC range from hundreds of kHz to 3 MHz. Thus, 300 kHz and 1.5 MHz frequencies are selected for externally fed bearing voltage signals. In addition, instead of a squarewave signal, the single-tone input signal provides a feasible approach to study the impedance behavior of the bearing. It is proposed that by the introduced procedure it is possible to estimate the operating point in which the CBC may reach sufficient magnitudes considering the bearing aging. In addition, the frequencies of the applied input signals are selected such that they differ from each other, and thus, the frequency dependency of the bearing electrical behavior can be studied at once. The results are considered useful supplementary information when the probability of occurrence of a certain type of bearing current comes into question. This is assumed to be crucial for example in nonintrusive measurements, where the general impedance behavior of bearings in the speed–temperature plane is desired to improve the accuracy of the analysis.

The studies discussed in this chapter are based on experimental measurements applied to bearing impedance measurements for $P_n = 15$ kW and $P_n = 75$ kW LVSCIMs and postprocessing of the measurement data. As a result, the bearing impedance behavior in the time domain and an intrusive method for its measurement are introduced. It is shown that by the proposed measurement procedure, a general pattern can be determined for the repeatability of the bearing behavior for a certain type of bearings.

The studies also aim to enhance understanding of the influence of the variation in crucial parameters: the effects of rotation speed and operating temperature on the bearing impedance behavior, based on which it is possible to determine the occurrence of harmul bearing current types for different motor sizes (P_n = 15 kW EDM and P_n = 75 kW CBC). Furthermore, the study demonstrates the dependency between the bearing mode transients and the occurrence of an RF signal that is applied to the RF-SBBCDM (Särkimäki 2009). The studies discussed in this chapter are based on Publications III and VI.

2.1   Bearing impedance measurement

This measurement method was first introduced in studies where the target was to artificially excite a magnitude of CBC in a P_n = 15 kW motor. In the course of the measurements it was found that the externally fed sinusoidal voltage waveform was interrupted by sudden collapses. At the same time, an increment in the bearing current magnitude was detected. Thus, the idea for an impedance analysis arose; the bearing impedance analysis is based on the measurement of bearing voltage and current waveforms of an externally fed sinusoidal signal with a fixed frequency. The frequencies applied in the externally fed signal are selected based on the fact that f_{in} = 300 kHz and f_{in} = 1500 kHz are the frequencies that may be present in the case of CBC. Moreover, they are considered to deviate so much from each other that the effect of signal frequency on the impedance can be studied. In addition, it is argued in the literature (Zika et al., 2009) that a DC signal prevents the restoration of the lubricant oil film, and thus, EMD would no longer occur in the bearing. Consequently, the degradation level would be significantly lower than for AC signals. In addition, it is not possible to measure capacitance in the case of a DC signal, or at least a transient is needed for calculation. Therefore, the procedure would be more difficult compared with the analysis of MF signals. The bearing impdedance is calculated by

$$Z_b = \frac{U_b}{I_b},\tag{2.1}$$

where the complex U_b and I_b are measured from the bearing, and the magnitude of impedance is determined by

$$|Z_b| = \sqrt{R_b^2 + X_b^2}\tag{2.2}$$

and the phase angle by

$$\alpha_{Zb} = \tan\left(\frac{X_b}{R_b}\right).$$
(2.3)

Now, when $\alpha_{Zb} = 0°$, $X_b = 0$, and $R_b = Z_b$, and when $\alpha_{Zb} = -90°$, $R_b = 0$, and $X_b = Z_b$, the capacitance of the bearing can be determined as the frequency f_{in} of the sinusoidal input signal is known

$$C_b = \frac{1}{2\pi f \cdot X_b}.$$
(2.4)

The bearing impedance calculation, which is based on an FFT analysis of U_b and I_b, is executed in Matlab. The Matlab script is presented in the FFT and impedance calculation script (Appendix A). In addition to the voltage and current waveforms, the bearing temperature is also measured. An illustration of the measurement setup is shown in Fig. 2.1 and the equipment applied with the $P_n = 15$ kW motor is introduced in Table A1 (Appendix A). Examples of the measured bearing voltage and current waveforms in different operating conditions and the assosiated impedance analysis are shown in Fig. 2.2.
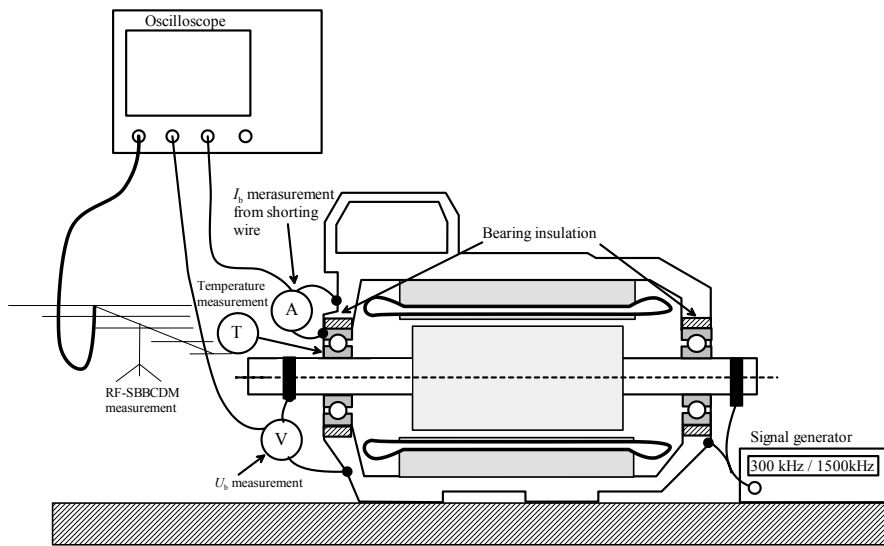

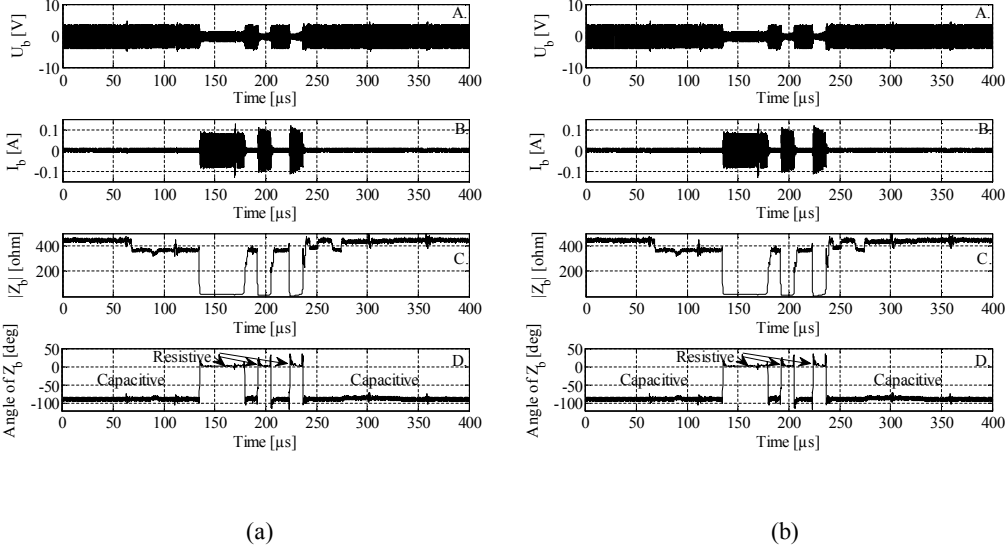Fig. 2.1. Measurement setup for bearing impedance measurements.

(a)   (b)

Fig. 2.2. Bearing impedance analysis based on a measurement executed with P_n = 15 kW and under the operating parameters n = 1500 rpm and f_{in} = 1500 kHz. Subplots A of both Fig. 2.2a and Fig. 2.2b depict an externally fed sinusoidal bearing voltage waveform, and subplots B the corresponding bearing current waveform. Subplots C illustrate the magnitude of the bearing impedance calculated from the data shown in subplots A and B. Subplots D provide the phase information of the impedance analysis. In Fig. 2.2a, the impedance analysis parameters are C_b = 0.15 nF, $R_{b,\,min}$ = 23.8 Ω, and $T_{b,de}$ = 30 ℃. In Fig. 2.2b, the impedance analysis parameters are C_b = 0.24 nF, $R_{b,\,min}$ = 5.8 Ω and $T_{b,de}$ = 49 ℃.

When comparing the measurements shown in Fig. 2.2a and Fig. 2.2b, major changes in the impedance can be detected. When the motor is warming up, the capacitance of the bearing is likely to increase, which is due to the thinner oil film within the bearing. Further, in the resistive mode, as shown in the subplots on the right, a lower $R_{b,min}$ value can be found when compared with the case shown in the subplots on the left. It is noted that the analysis is applicable to a static bearing mode analysis, not to an impedance analysis of the bearing mode transients. This is because of the restricted bandwidth of the measurement, the applied decimation, and the additional filtering in the analysis. The highest frequency that can be handled in the analysis is set by the Nyquist criteria

$$f_{max} = \frac{f_{s,dec}}{2}. \tag{2.5}$$

On the other hand, in order not to produce distortion to the frequency content in the analysis, the lowest frequency component that can be included in the analysis is set by the FFT window size N_w. In addition, the window size has to be $N_w = 2^N$, where N is a positive integer.

$$f_{\min} = \frac{f_{s,dec}}{N_w} \tag{2.6}$$

Hence, in the impedance analysis on a f_{in} = 300 kHz signal with a sampling frequency after decimation $f_{s,dec}$ = 10 MHz and a window size N_w = 32, the frequency range of the analysis is set to 300 kHz $\leq f_{bw} \leq$ 5 MHz. Similarly, for a f_{in} = 1500 kHz feed signal, N_w = 8 resulting in a 1.25 MHz $\leq f_{bw} \leq$ 5 MHz signal band. This means that from the mechanical point of view, bearings can be considered stationary during the bearing mode transient, and the effects caused by the movement of bearing balls can be neglected. When considering the capacitive mode, based on the impedance analysis, it is possible to approximate the overall lubricant film thickness inside the bearing. In order to give a comprehensive idea of the analysis, typical A_H values and the corresponding capacitance values are obtained as a function of lubricant film thickness in the motor that is subject to EDM bearing currents. The case of the curve series shown in Fig. 2.3a and when Eq. (1.4) is applied with ε_r = 3 as given in (Muetze and Binder, 2007b) is presented as an example. For comparison, for a P_n = 15 kW LVSCIM and 6309-C3 ball bearings, the average value of A_H without any external load forces is approximately 2.4 mm^2 (Muetze et al., 2006). It is worth noticing that A_H is also a function of external forces concentrated on the bearings. Since external forces are likely to vary depending on the operating parameters and the motor application, there will probably also be some deviation in A_H. Further, the second subplot gives some examples of capacitances for bearings that are commonly used in the motor size of H_f = 160 mm, where the bearings are subject to severe degradation caused by EDM. The values illustrated in Fig. 2.3b are calculated according to the A_H values acquired from (Muetze, et al., 2006; Oliver and Binder, 2009).
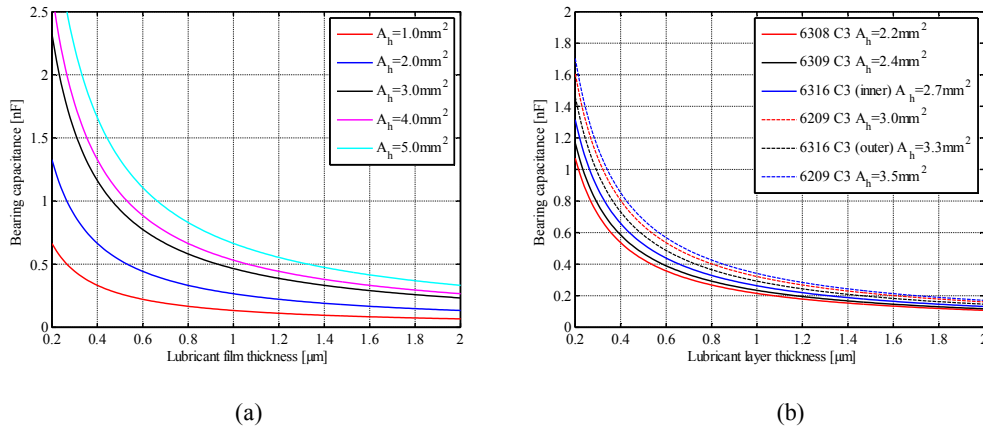

(a)

(b)

Fig. 2.3a. Bearing capacitance as a function of lubricant oil film thickness of different Herzian areas.
Fig. 2.3b. Bearing capacitance as a function of lubricant oil film thickness for commonly used bearing sizes.

2.2 Bearing modes

As shown above in Fig. 2.2, bearings are determined to have two static electrical operating modes, capacitive and resistive. In the capacitive mode, the voltage over a bearing can be built up, and the bearing represents closely the capacitance, having a $\alpha_{Zb} \approx -90°$ phase shift between current and voltage. Alternatively, in the resistive mode, the resistance ranges from a few ohms up to a couple of dozens of ohms. The phase shift between voltage and current is $\alpha_{Zb} \approx 0°$, and thus, the impedance is close to the pure resistive mode.

2.2.1 Bearing mode transient activity

In addition to two static bearing modes, there are three distinguishable bearing operating regions: pure capacitive, active, and pure resistive. In the active region, the bearing changes its mode between capacitive and resistive. In several publications (Busse et al., 1997a; Busse et al., 1997b; Tischmacher and Gattermann, 2010), the limits between the operating regions in the speed–temperature plane are determined by adjusting the magnitude of the input signal as high as possible. In these cases, it is often of interest to know the highest possible voltage stress of the square wave signal that the bearing is capable of withstanding. However, there are only a few studies on voltage stress levels that may occur in actual VSI drive systems, instead of arbitrarily selected, externally fed voltage levels. In this doctoral dissertation, based on short-period measurements lasting no longer than two to four hours, it is concluded that the operating parameters such as rotation speed and operating temperature have a significant effect on the bearing mode transient activity (TrA) when $\hat{U}_b \leq 10$ V. Thus, the studies presented in this doctoral dissertation are brought closer to practice, where changes between operating regions are not entirely determined by the highest possible voltage stress but also by other operating parameters that mainly determine the oil film thickness within bearings. Further, it is shown that TrA from the capacitive to resistive mode corresponds to the EDM DA obtained by the RF-SBBCDM in the case of a VSI-driven system. It was found that a deviation in the bearing impedance modulates the externally fed sinusoidal signal. The waveforms of U_b in the pure capacitive region, active region, and pure resistive region are shown in Fig. 2.4. In the example series, the operating parameters $n = 1500$ rpm, of $P_n = 15$ kW, $f_{in} = 300$ kHz and $\hat{U}_b = 7$ V externally fed signal) were kept constant while the motor was warming up.
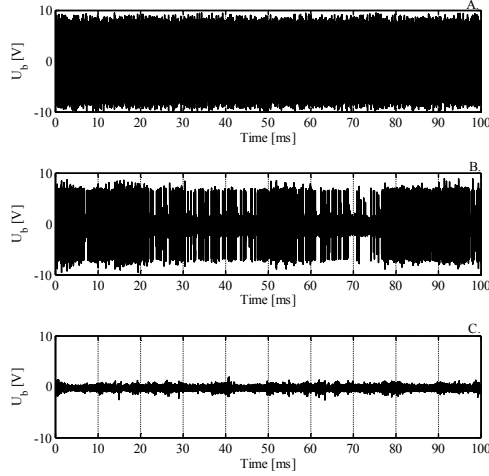
Fig. 2.4. Three operating regions of the P_n = 15 kW motor with n = 1500 rpm, f_{in} = 1500 kHz, and $\hat{U}_b$ = 7 V. Starting from subplot A: pure capacitive region at $T_{b,de}$ = 33 ºC, subplot B: active region at $T_{b,de}$ = 47 ºC and subplot C: pure resistive region at $T_{b,de}$ = 54 ºC.

According to (Frenzel 1999), the measured U_b waveform can be interpreted as a digital version of the analog amplitude modulation (AM), called a binary amplitude shift keying (ASK) signal. Here, the carrier wave $\hat{U}_{in} \cdot \sin(2\pi f_{in}t)$ is modulated by an information signal $U_i(t)$, which has two possible values [not true : true]. The logic 'not true' represents the resistive mode and the logic 'true' the capacitive mode. Now, the transmitted and the received signal can be expressed as

$$U_b = \hat{U}_{in} \cdot \sin(2\pi f_{in}t) + U_i(t) \times \sin(2\pi f_{in}t).$$
(2.7)

Thus, mode changes can be detected by demodulation of the measured U_b signal. When the modulation index of the AM signal $m_i \leq 1$, an envelope detection method can be applied to separate the information signal (the mode transients) from U_b. The information signal can be separated from the carrierwave signal U_{in} by the following signal processing procedure: first, the received signal U_b is rectified

$$U_{b,abs} = |U_b|.$$
(2.8)

It is pointed out that as a product of rectification, the signal frequency is doubled. Next, the rectified signal is low-pass filtered. The pass band of the filter is adjusted according to

56

$$f_{pass} < f_{ub,abs}. \tag{2.9}$$

Since the target is to detect as short-period changes in the bearing mode as possible, f_{pass} = 550 kHz was set for f_{in} = 300 kHz. Similarly, f_{pass} = 2950 kHz was chosen when f_{in} = 1500 kHz was applied. It is pointed out that unlike in the conventional analog AM signal demodulation, the information signal $f_i \ll f_{in}$ is no longer only true in this certain case of ASK. Yet another option for low-pass filtering would be to use a band stop filter that filters U_{in}. An advantage of the procedure would be that shorter mode transient periods than $1/2 \cdot f_{in}$ could be detected, but at the cost of an increased noise level caused by the signal distortion of the rectification process and other additional interferences. This leads to a decision to apply a conventional low-pass filter. Now, TrA is determined by counting transients from the demodulated signal. Further, a hysteresis filter with 25% threshold margins was applied to reduce the effect of noise for the TrA analysis. Envelope detection and hysteresis filter levels are shown in Fig. 2.5, and the calculation script for TrA in the case of f_{in} = 300 kHz is presented in the TrA Matlab script (Appendix A).
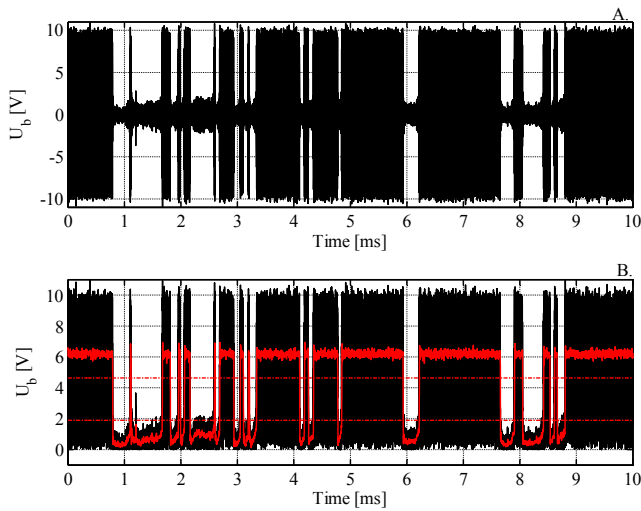
Fig. 2.5. Demodulation of the U_b signal for the TrA analysis. Subplot A presents the original U_b signal and subplot B the envelope signal of the original bearing voltage waveform (black) and information signal U_i (red).

Based on the signal processing and analysis shown in Fig. 2.5, Table 2.1 lists the experimental values with a wider range of rotation speeds and temperatures and their relation to the bearing behavior for the P_n = 15 kW motor and f_{in} = 300 kHz in different speed–temperature conditions, when the signal is analyzed within a T_w = 100 ms time window. Similarly as in Table 2.1, Table 2.2 lists the experimental values for the

bearing behavior for the $P_n = 15$ kW motor and $f_{in} = 1500$ kHz input signal in different rotation speed and temperature conditions, when the signal is analyzed within a $T_w = 100$ ms time window.

Table 2.1. $P_n = 15$ kW motor, $f_{in} = 300$ kHz MF supply voltage, and $\hat{U}_b = 7$ V.

n	*Temp*	*TrA*	*Cap. Mode*	C_b	$R_{b,min}$
[rpm]	[°C]	[$^1/_{ms}$]	[p.u]	[nF]	[Ω]
240	23	0.15	0.9998	0.36	n.a
	37	0	0.1382	0.89	n.a
450	28	0	0.9997	0.36	n.a
	48	2.16	0.0328	0.9	5.3
1500	30	0	1	0.62	29.9
	56	2.44	0.0181	n.a	n.a
2000	24	0	1	0.12	20.3
	41	2.08	0.0235	0.31	7.6
3000	24	0	1	0.12	17.9
	44	1.08	0.110	0.35	4.7

Table 2.2. $P_n = 15$ kW motor, $f_{in} = 1500$ kHz MF supply voltage, and $\hat{U}_b = 7$ V.

n	*Temp*	*TrA*	*Cap. Mode*	C_b	$R_{b,min}$
[rpm]	[°C]	[$^1/_{ms}$]	[p.u]	[nF]	[Ω]
200	28	0.37	0.0158	0.31	20.3
400	26	0.33	0.9733	0.24	29.5
1500	27	0.08	0.9973	0.15	46.6
	48	2.99	0.0478	0.24	5.8
2000	29	0.33	0.991	0.14	20.1
	47	10.55	0.2491	0.22	4.1
3000	28	0.02	0.9992	0.14	15.1
	48	4.82	0.0601	0.26	4.7

The experimental values for the bearing behavior for the $P_n = 75$ kW motor and $f_{in} = 300$ kHz in different rotation speed and temperature conditions are listed in Table 2.3, when the signal is analyzed within a $T_w = 100$ ms time window. Compared with the measurements executed with the $P_n = 15$ kW motor, it was noticed that the input signal level was limited by the current feeding capacity of the signal source. It was concluded that in the case of the $P_n = 75$ kW motor, a lower impedance was introduced because of the larger contact areas in the bearing. Thus, it was not possible to get the voltage to the same level as in the $P_n = 15$ kW in all of the operating points. Therefore, for the sake of consistency, an $\hat{U}_b = 2.5$ V input signal was used in the measurement series with the $P_n = 75$ kW motor. The measurement equipment for the $P_n = 75$ kW motor test setup is listed in Table A2 (Appendix A). Further, similar to Table 2.3,

58

Table 2.4 gives the experimental values regarding the bearing behavior for the P_n = 75 kW motor and f_{in} = 1500 kHz input signal under different rotation speed and temperature conditions, when the signal is analyzed within a T_w = 100 ms time window.

Table 2.3. P_n = 75 kW motor, f_{in} = 300 kHz, MF supply voltage, and $\hat{U}_b$ = 2.5 V.

n	*Temp*	*TrA*	*Cap. Mode*	C_b	$R_{b,min}$
[rpm]	[°C]	[$^1/_{ms}$]	[p.u]	[nF]	[Ω]
240	24	027	0.9153	0.51	9.4
	37	2.10	0.0713	0.67	9.6
450	24	0.26	0.9784	0.36	7.9
	37	2.18	0.7782	0.62	6.8
	46	3.75	0.1312	0.97	4.8
1500	24	0.01	0.9989	0.26	n.a
	37	2.79	0.8734	0.51	5.2
	57	4.54	0.0556	0.92	4.5
2000	27	0	1	0.25	8.9
	36	2.63	0.9341	0.32	5.2
	47	16.88	0.2757	0.36	4.0
3000	28	1	0.9992	0.18	8.2
	36	0.45	0.99	0.23	5.6
	50	8.55	0.5318	0.4	3.3

Table 2.4. P_n = 75 kW motor, f_{in} = 1500 kHz, MF supply voltage, and $\hat{U}_b$ = 2.5 V.

n	*Temp*	*TrA*	*Cap. Mode*	C_b	$R_{b,min}$
[rpm]	[°C]	[$^1/_{ms}$]	[p.u]	[nF]	[Ω]
200	25	1	0.9985	0.22	5.1
400	25	0	1	0.18	n.a
	39	4.4	0.2053	0.39	1.6
1500	26	0	1	0.18	11.6
	39	1	0.9997	0.25	6.5
	48	6.41	0.643	0.54	3.7
2000	27	0	1	0.16	5.1
	50	6.8	0.159	0.55	5.1
	64	0.5	0.001	1.1	2.5
3000	28	0.04	0.9985	0.2	11.3
	38	4.65	0.8651	0.26	6.7
	50	10	0.6378	0.4	5.6

For both motors, it was determined with which temperature and rotation speed parameter combination the bearings are in the pure resistive mode. This was done to assist the analysis considering the probability of occurrence of CBC and the end of

EDM. The experimentally obtained speed–temperature lines for the pure resistive region for both the $P_n = 15$ kW ($\hat{U}_b = 7$ V) and $P_n = 75$ kW ($\hat{U}_b = 2.5$ V) motors with $f_{in} = 300$ kHz and $f_{in} = 1500$ kHz input signals are shown in Fig. 2.6. Especially in the $P_n = 15$ kW motor when the radial load forces to the rotor are kept constant, it can be seen that the limits of the electrical operating region of the bearing in the speed–temperature plane can be varied by adjusting f_{in} of the voltage stress signal. Again, it is suggested that the applied voltage magnitude has a similar effect on the limits of the region in the speed–temperature plane.
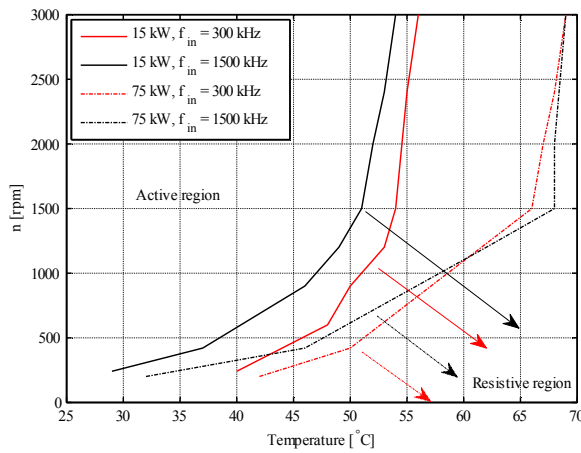

Fig. 2.6. Temperature–speed lines of the $P_n = 15$ kW and $P_n = 75$ kW motors for transitions from the active region to the pure resistive region in the case of $f_{in} = 300$ kHz and $f_{in} = 1500$ kHz signals. $\hat{U}_b = 7$ V for $P_n = 15$ kW and $\hat{U}_b = 2.5$ V for $P_n = 75$ kW. In the figure, the active region covers areas on the left from each boundary line; similarly, the right-side areas are for the pure resistive regions. The arrows are associated with the corresponding boundary lines by the same colors and line types to illustrate the movement further into the pure resistive region.

In addition to the determination of the limits for operation in the pure resistive region, it is pointed out that CBC is likely to occur during resistive-mode periods when bearings are operating in the active region. However, CBC may not necessarily reach significant magnitudes in terms of aging impact even if the bearing(s) are in the resistive mode (regardless of the operating region). Therefore, it is assumed that the accuracy of the CBC aging impact analysis given in Eq. (1.12) and the dependency on the I_g values given in Table 1.2, as discussed in section 1.1.8, can be improved by applying the information acquired by the bearing impedance analysis. Thus, the frequencies of the input signals applied to the bearing impedance analysis were selected according to frequencies that commonly correspond to the frequency of U_b and I_b in the case of CBC. Further, to enhance the analysis accuracy, it is considered essential that the deviation of $J_{b,rms}$ is determined. As demonstrated in this chapter, the variation in $R_{b,min}$ can be determined by measurements. As a practical example for $J_{b,rms}$ deviation studies, the values (listed in Table 2.4) from two operating points in the case of $f_{in} = 1500$ kHz,

$n = 200$ rpm, $H_f = 280$ mm, $l_s = 0.5$ m, ($P_n = 75$ kW), $C_{rf} = 35.2$ nF (measured), $l_{cm} \approx 10$ m ($l_{ce} =$ short), and $R_{b,tot} = 2 \cdot R_{b,min}$ The experimental reference values of I_{cbc} are determined from CBC measurements executed with the measurement setup introduced in Table C3 and Fig. C5 (Appendix C). It is pointed out that in this analysis, the resistance of the motor frame as a part of the CBC path is not taken into account. Furthermore, the analysis is based on the combination of U_{shaft} Eq. (1.11) and the approximation given in Eq. (1.15) for an electrically short cable

$$U_{shaft} \leq 1.5 \cdot \frac{du_{Lg}}{dt} \cdot C_{wf} \cdot l_s . \tag{2.10}$$

For analysis, it is assumed that only U_{shaft} has an effect on the bearings, and hence, Eq. (2.1) is applied. In the resistive mode $Z_b = R_b$ holds, and thus, $\hat{I}_{cbc}$ can be approximated by

$$\hat{I}_{cbc} \leq \frac{\hat{U}_{shaft}}{R_{b,tot}} . \tag{2.11}$$

Based on the equations above, the curves illustrated in Fig. 2.7 can be generated. Subplot A represents $\hat{I}_{cbc}$ as a function of the sum resistance of the bearings for different du_{Lg}/dt at the motor terminal supply signal. According to subplot A of Fig. 2.7, it can be approximated that du_{Lg}/dt could be $du_{Lg}/dt = 0.5$ kV/µs for the experimentally measured operating points acquired in Chapter 2 for the $P_n = 75$ kW motor and $f_{in} = 1500$ kHz. This is simply based on the location of both operating points that are well in line with the curve (not verified with a measurement of du_{Lg}/dt). Again, from subplot B, the limits in the $R_{b,tot}$ - A_H plane for different du_{Lg}/dt signals for considerably high CBC densities are determined. Based on the selection of $du_{Lg}/dt = 0.5$ kV/µs, from subplot B of Fig. 2.7, we can see that for example, if $A_H = 5$ mm^2 for the bearings, neither of the example operating points would be within the aging impact zone. For reference, in similar conditions but with $du_{Lg}/dt = 1$ kV/µs, significant CBC values may occur.
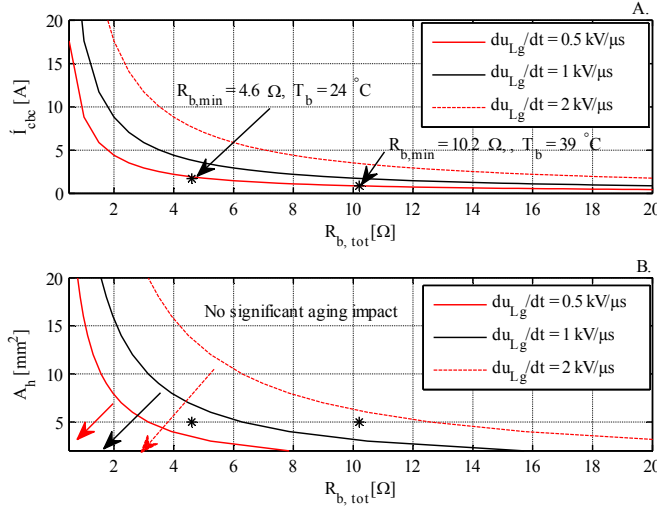
Fig. 2.7. Subplot A: influence of the bearing resistance on the magnitude of CBC. Subplot B: the influence of the bearing resistance on the bearing current density with a significant aging impact generated by CBC (LVSCIM, l_{ce} = short, H_f = 280 mm, (P_n = 75 kW) and C_{wf} = 35.2 nF. Subplot B depicts the aging impact boundary curves, where $J_{b,rms}$ = 0.56 A/mm^2, for each du_{Lg}/dt. Further, each arrow (associated with the color and line type) demonstrates the direction of the increase in the aging impact from the boundary curves. In the example case, both measurement points are on the right side of the du_{Lg}/dt = 0.5 kV aging impact boundary curve, and therefore, the aging impact is not involved when A_H = 5 mm^2 is set.

2.2.2 Bearing mode transient detection by the RF-SBBCDM

It was studied how the received RF pulses correspond to the input signal waveform transients. Figure 2.8a depicts an example case demonstrating the U_b, I_b, and U_{RF} waveforms of the P_n = 15 kW motor running at n = 1500 rpm in the temperature $T_{b,de}$ = 24 ºC and fed by a $\hat{U}_b$ = 10 V, f_{in} = 300 kHz input signal. When comparing with the TrA analysis executed with signal demodulation, it can be seen that short-mode transients can be detected with the RF-SBBCDM while such transients are invisible in the signal demodulation analysis. As can be seen in Fig. 2.8a, some of the EDM events in the U_b waveform (subplot A), which can be verified by current pulses I_b (subplot B), do not cause clearly detectable RF pulses in U_{RF} (subplot C). The location of not detectable (or missing) RF pulses is indicated by a dashed ellipse. This is because the discharge takes place from such a low U'_b level that the radiated part of the energy is most probably too weak to be detected properly from the noise. Further, we can see that the higher the U'_b level is at the moment of discharge, the higher is the received RF pulse amplitude. Hence, it is possible that the mode transient from those U'_b levels that do not cause a detectable RF pulse may be insignificant when considering their aging impact. Moreover, Fig. 2.8b demonstrates a disadvantage of the envelope detection

method, since it is not able to spot the short-term bearing mode changes (periods shorter than $1/f_{in}$). We can see that only two transients from the capacitive to the resistive mode would have been detected. For contrast, depending on the trigger level, the RF-SBBCDM detects up to six discharges. In addition to the fact that the RF-SBBCDM is nonintrusive, this is considered an advantage of the RF-SBBCDM.

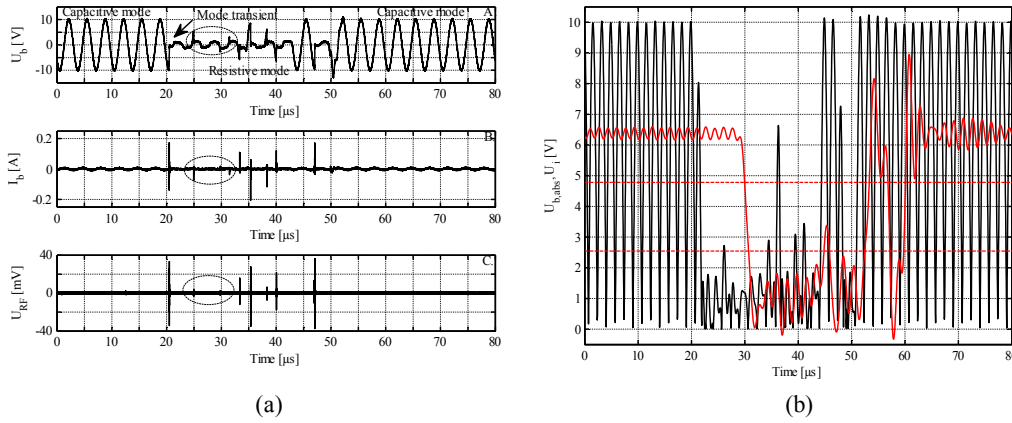(a)   (b)

Fig. 2.8. Comparison of the bearing mode transient analysis. Fig. 2.8a. Bearing mode transients and the corresponding RF pulses at the moments of transients from the capacitive to the resistive mode. The location of not clearly detectable (or missing) RF pulses associated with EDM events that occur from $U'_b < 5$ V is indicated by a dashed ellipse in each subplot of Fig. 2.8a. Fig. 2.8b. Bearing mode transient analysis by the envelope detection method, where $f_{in} = 300$ kHz, $\hat{U}_{b, abs} = 10$ V (black), the information signal U_i (red), and the mode transient threshold levels (dashed red).

2.3 Conclusions

In this chapter, the intrusive method for the FFT-based bearing impedance analysis and the envelope-detection-based TrA measurement were introduced and applied. It was shown that with the intrusive methods, the electrical behavior of bearings in different points of the speed–temperature plane can be determined. In addition, the performance of the TrA analysis is compared with the RF-SBBCDM. On a short time window scale (60 µs), as in Fig. 2.8a, it seems that the magnitude of the received RF pulses is directly related to U'_b. In addition, it is assumed that in a certain operating point (speed–temperature plane), the values of TrA and DA would be equal. This is when the lubricant film within the bearing is thick enough to withstand voltage stress without discharge until a level is reached at which the discharge is capable of generating a detectable RF pulse, and on the other hand, the bearing mode periods are long enough to be detected by an envelope signal analysis. It is concluded that detection of the entrance to the pure resistive region could be possible by combining the RF-SBBCDM and general knowledge of the electrical behavior of a certain bearing type with a certain lubricant. The measurement methods applied in this chapter and their main properties

are listed in Table 2.5. Moreover, according to the studies presented in this doctoral dissertation, three operating regions and two operating modes of bearings can be determined. Certain consistency in the electrical behavior of bearings was detected when the bearing behavior was studied within a short time frame compared with the lifetime of a bearing. Here, the effect caused by bearing wear can be considered insignificant (in this case; $t_{op} < 50$ h). A summary of the parameters related to the bearing behavior is given in Table 2.6.

Table 2.5. Main properties of the applied bearing-current-related measurement procedure.

Measurement purpose	Analysis method	Measurement type	Advantages	Disadvantages
Impedance analysis	FFT	intrusive	oil film thickness analysis discharge energy, voltage measurement	intrusive, requires motor modification, external single-tone signal needed
TrA, Bearing operating region analysis	Envelope detection	intrusive	can be done simultaneously with impedance analysis	intrusive, $1/f_s$ transients neglected, external single-tone signal needed
DA, Bearing operating region analysis	RF-SBBCDM	nonintrusive	nonintrusive, also detects $<1/f_s$ mode transients	No specific information on energies or bearing voltage levels

Table 2.6. Summary of the parameters related to the bearing behavior.

Bearing region	Pure capacitive	Active	Pure resistive
Bearing mode (s)	capacitive	capacitive/resistive	resistive
Lubricant oil film thickness	Thick enough to withstand voltage stress of $\hat{U}_b$ entirely	Lubricant layer is capable of withstanding voltage stress, but only up to a certain voltage level that is $< \hat{U}_b$	Thin to none (galvanic contact), only incipient $\hat{U}_b$ voltage levels may occassionally exist
Location in the speed–temperature plane*	High speed, low temperatures	Between pure capacitive and resistive regions	Low speed, high temperatures
Possible harmful bearing current type(s) **	None	EDM, (CBC)	CBC

*Determined with the SNR 6309-C3 $P_n = 15$ kW motor and the SNR 6316-C3 $P_n = 75$ kW (SNR). In addition, the frequency content and magnitude of U_b is likely to affect the operating region limits in the speed–temperature plane. **RGC is not included.

The initial-mode requirements for the EDM and CBC bearing currents are:

- For EDM, both (all) bearings are in the capacitive mode.
- For CBC, both bearings are in the resistive mode.

In general, it is concluded that when the bearings warm up, discharges start to take place from the lower bearing voltage levels, thus accelerating the DA. In the point where DA starts to decrease, one of the bearings of a motor is in the resistive mode for the most of the time. This leads to a conclusion that the longer is the time that the bearing(s) are in

the resistive mode, the higher is the possibility of CBC. Furthermore, in order to improve the accuracy of the CBC aging impact analysis, a new method to study the deviation in the bearing resistance and the deviation in $J_{b,rms}$ is introduced. The study demonstrates the importance of bearing electrical behavior but also understanding of the resistance behavior when considering the existing CBC magnitudes and a possibility of bearing wear. For the applied test setup and in the light of the acquired $R_{b,min}$ values, according to the introduced $R_{b,min}$-based CBC magnitude estimation, Eq. (2.11), it is proposed that CBC should not reach magnitudes that would lead to an aging impact anywhere in the active region. In general, this of course depends on the values of the du/dt and A_H parameters. Unfortunately, simultaneous measurement of the bearing impedance and the magnitude of CBC is considered somewhat difficult, which makes the accuracy verification of the method uncertain. In addition, in order to verify the applicability of the proposed method in a more general form, CBC events from a wide temperature range ($T_b > 80$ °C) with dozens of CBC events should be analyzed. Thus, in general, a feasible method to determine operation in the pure resistive region would be profitable. Moreover, the accuracy of the handheld infrared thermometer presented in Table A1 (Appendix A) is around ±5 ºC (including the uncertainty caused by the person holding the device), thereby making the reproducibility studies impractical. It is pointed out that the temperature values reported within the test series in this chapter are comparable with the given uncertainty as they are executed with the same procedure (measured from a certain location and distance from the corner of the DE bearing and the shaft). However, a higher uncertainty than announced may be involved if the results are compared with other similar tests executed elsewhere. This is because of the possibility of a nonverified consistent error (offset) between the actual temperature values and the corresponding measured ones. Thus, it is proposed that thermocouples such as PT-100 should be applied to more accurate temperature measurement. This, however, was not executed in this doctoral dissertation as the objective of the study was only to study possible methods, not to verify them at a general level. For these reasons, the reproducibility of the electrical behavior of bearings in the speed–temperature plane should be verified. Depending on the deviation in reproducibility, the results of the bearing impedance analysis may not be directly applicable as a look-up table reference to nonintrusive bearing current estimation. However, the analysis is considered to be applicable as a supplementary tool for example in nonintrusive bearing current measurement methods, where the probability of the occurrence of different bearing modes may be in focus. To sum up, the studies presented in this chapter are considered to be crucial to demonstrate the problems related to EDM and CBC bearing current measurements. Hence, further studies on reproducibility are considered mandatory. Nevertheless, these studies are deemed far beyond the scope of this doctoral dissertation.

3 Verification of the RF-signal-based detection method in the case of CBC and RGC

The objective of this chapter is to verify the dependency between CBC and RGC events with the associated RF pulses that are received by the RF-SBBCDM. As it was shown and concluded in Chapter 2, conditions in which CBC is likely to occur are present when the bearings are operating in the resistive mode. Based on $R_{b,min}$ values acquired in Chapter 2, it can be proposed that CBC would not possibly reach magnitudes sufficient to degrade the bearings, until they are in the pure resistive region. Therefore, it is considered crucial to verify that CBC does not cause detectable RF pulses when measured by the RF-SBBCDM. Thus, transition to the pure resistive region could be detected by nonintrusive measurement. The research is carried out by concurrent measurements where CBC and RGC detected by U_b and I_b waveforms are acquired by intrusive measurents, and meanwhile, the occurrence of the associated and detectable RF pulses is verified. In these verification measurements, different configurations of the experimental VSI-driven motor measurement setup are used, where the magnitude of the desired bearing current is stimulated by measurement setup modifications. As a result, the exhaustion of the associated RF pulse in the case of CBC and RGC is verified. Because of the applied RF-SBBCDM and its band-pass filter, a sinusoidal CBC waveform should not be detected by the RF-SBBCDM. The same should apply to RGC if it occurs when the bearings are in the resistive mode. Hence, it is assumed that operation in the pure resistive region can be detected by observing the exhaustion of RF pulses. The studies discussed in this chapter are based on Publications III and IV.

3.1 Measurements with a conventional bearing configuration

In general, it is possible that $I_{b,nde}$ and $I_{b,de}$ may contain terms that are caused by other bearing currents than CBC; therefore, it is advisable to determine that $|I_{b,nde,cbc}| = |I_{b,de,cbc}|$ applies to the CBC current terms. In addition, the phase shift between the CBC current terms is either $\alpha = 0°$ or $\alpha = 180°$, depending on the configuration of the positive current flow direction of the applied current probes. Similarly as for the measurements discussed in this chapter, both of the probes are assembled so that the positive current flow direction is the same (from the frame to the bearing or vise versa), and thus, $I_{b,de,cbc} = -I_{b,nde,cbc}$. Now, the magnitude of the CBC can be determined as

$$\hat{I}_{cbc} = \sqrt{\hat{I}_{b,de}^2 + \hat{I}_{b,nde}^2 + 2 \cdot \hat{I}_{b,de} \cdot \hat{I}_{b,nde} \cdot \cos(\alpha')} \,, \tag{3.1}$$

where α' is the phase shift between bearing current amplitudes $\hat{I}_{b,de}$ and $\hat{I}_{b,nde}$, and $\alpha' = 90{-}270°$, otherwise, $I_{b,de}$ and $I_{b,nde}$ do not contain a current term that is in a 180° phase shift.

As can be stated based on the introductory chapter and Publications III and IV, CBC is not found to reach high enough values to generate an aging impact or detectable RF

pulses under any circumstances in the case of the P_n = 15 kW motor; thus, the issue can be excluded from this doctoral disseration. Therefore, the studies discussed here are made for the P_n = 75 kW motor; accordingly, the measurement setup shown in Fig. 3.1 and the measurement equipment listed in Table B1 and Table B3 (Appendix B) were applied with a P_n = 75 kW motor, shown in Fig. B2 (Appendix B). The example measurements of the RF-SBBCDM for the P_n = 75 kW LVSCIM are shown in Fig. 3.2. It can be noticed that an incipient (visible), but in the field conditions nondetectable RF pulse is present. This observation is based on the consideration of a wider time window, when RF pulses with equal or higher amplitudes are received from interference sources. It was determined in the laboratory that if the trigger level for the RF pulse detection was set at $U_{th} \leq 3$ mV, the desired bearing current with the associated RF pulse could not be detected.
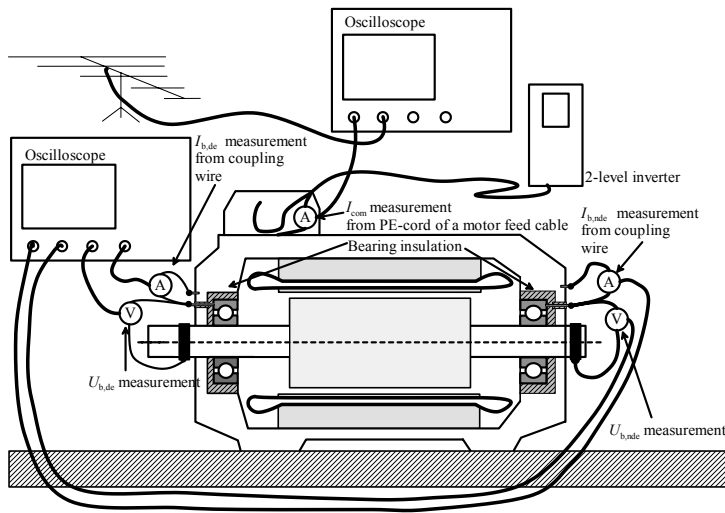

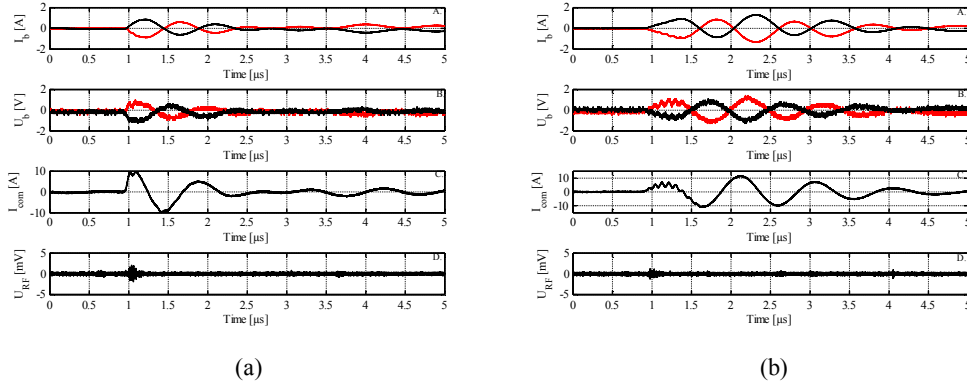Fig. 3.1. Illustration of the measurement setup for CBC.

Fig. 3.2. Experimental verification of the applicability of the RF-SBBCDM for CBC detection in the case of the P_n = 75 kW motor, n = 200 rpm and example waveforms of the CBCs for the detected RF pulses. In subplots A of Fig. 3.2a and Fig. 3.2b, $I_{b,nde}$ (red) and $I_{b,de}$ (black). In sublots B, $U_{b,nde}$ (red) and $U_{b,de}$ (black). Fig. 3.2a: at $T_{b,de}$ = 23 °C. Fig. 3.2b: at $T_{b,de}$ = 47 °C.

It was verified by laboratory measurements that RF signals with a small ($\hat{U}_{RF} \leq 2$ mV) amplitude can occasionally be received at the moment of the rise of the incipient bearing voltage that is followed by the CBC. As can be seen by comparing the subplots of Fig. 3.2a and Fig. 3.2b, less than two volts can be gained over the bearings during a transition further into the pure resistive region. The transition towards smaller bearing resistances can be detected by an increase in the bearing current magnitudes. In some cases, a small but detectable RF emission can be noticed. According to the studies shown in Fig. 3.2, the RF signal gets smaller as the resistance of the bearings decreases. It is pointed out that the waveform of the CBC itself consists of too low frequencies to cause a detectable signal to the receiver when the RF-SBBCDM is applied.

3.2 Measurements with a shorted NDE bearing configuration

Similarly, there was no received RF signal associated with the P_n = 15 kW motor when both of the bearings of the motor were set active. The measurement setup was modified in such a way that the NDE bearing was short circuited by a copper wire, but again, an associated RF pulse was not detected. The target of this procedure was to study whether an RF emission can be affected by the decreasing impedance on the CBC path thereby increasing the magnitude of the CBC. The applied measurement setup for both motor sizes is illustrated in Fig. 3.3. Experimental verification of RF-SBBCDM for the modified P_n = 75 kW motor setup is shown in Fig. 3.4.
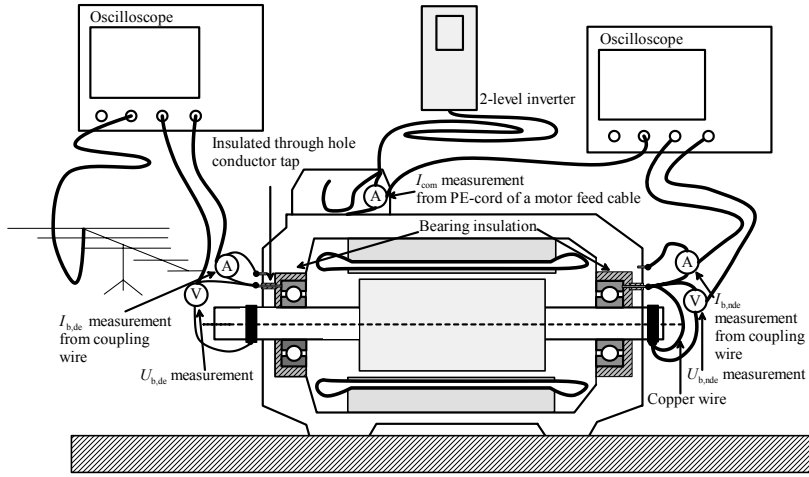
Fig. 3.3. Measurement setup for CBC when the NDE bearing is short circuited with copper wire.

As anticipated, it was observed that shorting the NDE bearing increases the magnitude of the CBC. However, a significant effect on the magnitude of the received RF pulses was not detected. This is because shorting of the NDE bearing disables the gain of the bearing voltage. Next, similar measurements were executed with the $P_n = 75$ kW motor and are shown in Fig. 3.4.
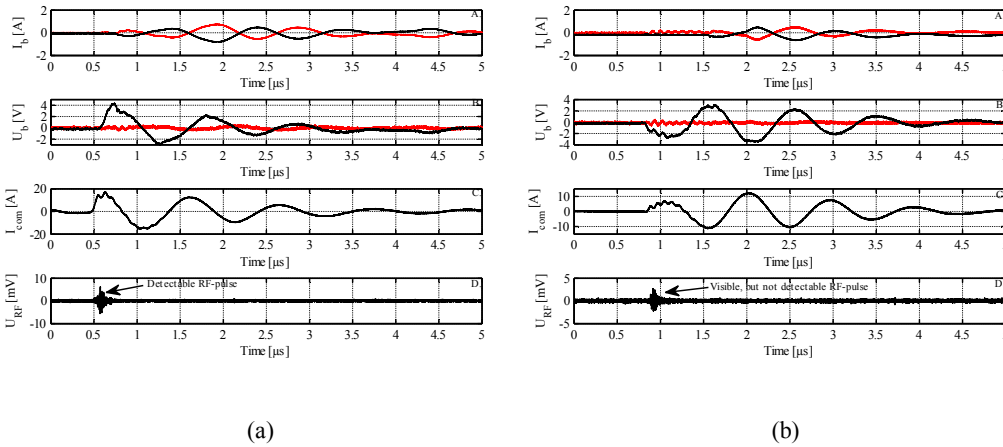

(a)   (b)

Fig. 3.4. Example waveform of the CBC for the detected RF pulse. The measurement is executed for the $P_n = 75$ kW motor with a short-circuited NDE bearing and an operating point of $n = 200$ rpm. In subplots A, $I_{b,nde}$ (red) and $I_{b,de}$ (black), in subplots B, $U_{b,nde}$ (red) and $U_{b,de}$ (black). In Fig. 3.5a, $T_{b,de} = 24$ ºC. Similarly, in Fig. 3.5b, $T_{b,de} = 48$ ºC.

3.3 RGC detection

In this section, it is also studied whether the RGC can be detected by the RF-SBBCDM. The measurement setup is shown in Fig. 3.5. In this test procedure, the protective earth (PE) conductor of the motor was removed from the motor terminal and connected to the shaft of the test motor, thereby providing only a low-impedance path for the ground currents to flow as RGC. Unlike previously in this chapter, and since RGC is found to reach high enough magnitudes to generate aging also in the case of $P_n = 15$ kW motor, RGC is included in the study. The results of the study conducted with the $P_n = 15$ kW motor are shown in Fig. 3.6.
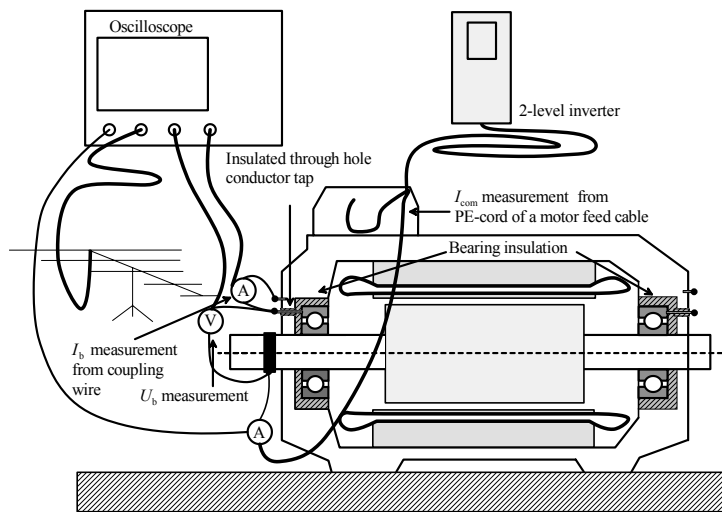

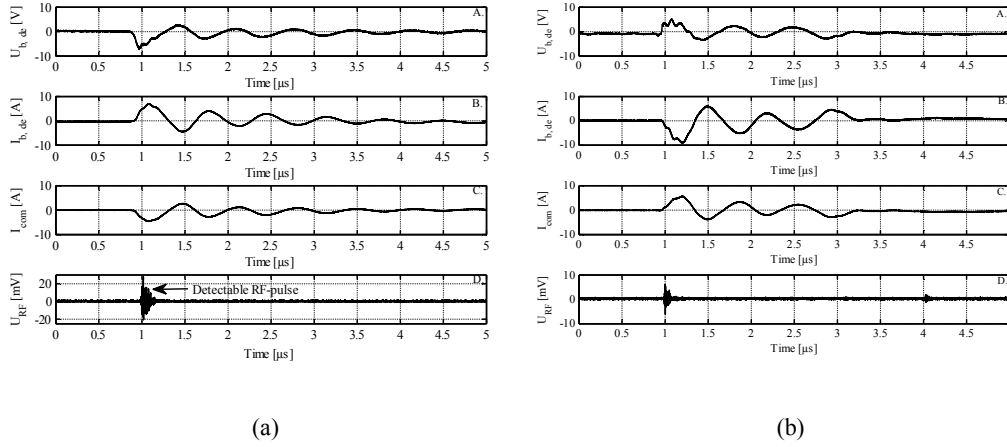
Fig. 3.5. Measurement setup for RGC.

(a)   (b)

Fig. 3.6. Example waveforms of the RGC for the detected RF pulse. The measurement is executed for the P_n = 15 kW motor with an insulated NDE bearing at n = 1500 rpm. In Fig. 3.6a, $T_{b,de}$ = 32 ºC. Simirlarly, in Fig. 3.6b, $T_{b,de}$ = 52 ºC. When moving upward in the temperature domain, weakening of the associated RF pulses can be noticed, and an increase in the $I_{b,de}$ magnitude is visible.

Based on a comparison of Fig. 3.6a and Fig. 3.6b, detectable RF signal levels are observed in the case of $T_{b,de}$ = 32 ºC. Again, a visible but in practice not detectable RF pulse is involved when the bearings are warmed up to $T_{b,de}$ = 52 ºC. It is pointed out that it is the bearing voltage level that is increased by changes in the measurement setup. Furthermore, the rotation speed n = 1500 rpm, which most propably enables a discharge-like event inside the DE bearing. It is also noteworthy that the time of the RF signal corresponds to the transient in the U_b waveform. A similar test procedure was carried out also with the P_n = 75 kW motor. Example cases of the measurements are shown in Fig. 3.7. Unlike in the P_n = 15 kW motor, the magnitude of the received RF pulses does not vary significantly when RGC is compared with the CBC measurements. Again, visible but in practice non-detectable RF pulses are detected.
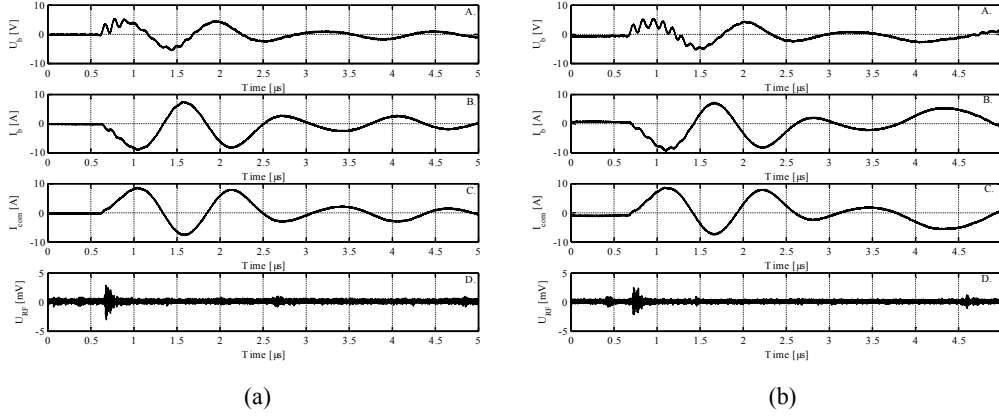
(a)   (b)

Fig. 3.7. Example waveforms of the RGC for the detected RF pulse. The measurement is executed for the $P_n = 75$ kW motor with an insulated NDE bearing at $n = 1500$ rpm. In Fig. 3.7a, $T_{b,de} = 25$ ºC. Similarly, in Fig. 3.7b, $T_{b,de} = 56$ ºC.

3.4   Conclusions

In this section, it was studied whether it is possible to detect the resistive operating region of bearings and occurrence of CBC and RGC nonintrusively by the RF-SBBCDM. The research was conducted by simultaneous intrusive measurements of U_b and I_b and the associated detectable RF emission by the RF-SBBCDM. In the measurements, different experimental measurement setup configurations were used to boost the magnitude of the desired bearing current. As a result, it was found that the received RF pulses associated with CBC were rare in occurrence and small in magnitude. It is noted that depending on the operating conditions and the measurement setup, it took up to ten minutes before an occasional, detectable and low-amplitude RF pulse ($\hat{U}_{RF} \ll 5$ mV) was received. Alternatively, RGC was detected to generate up to $\hat{U}_{RF} < 25$ mV pulses. Still, in all cases, the trend was that the magnitudes of the RF pulses were likely to decrease and became even more infrequent as a result of the bearing warm-up. In the occurrence of an RGC, an RF pulse was slightly more frequent (~1/10s) within the measurement series and more common at lower temperatures ($T_{b,de} < 40$ ºC). This leads to a conclusion that a nonlinear event such as a lubricant oil breakdown is most probably the key feature that stimulates a detectable RF emission. Further, it is proposed that transition into the entirely resistive region and a certain occurrence of CBC can be detected as a disappearance of RF pulses. Hence, based on the experimental measurements and the associated resistance values given for example in Table 2.4, in the pure resistive region, RF pulses are not detectable in the pass band of the RF-SBBCDM. Further, as the minimum criterion, it is proposed that RF pulses should not be received in case where CBC exceeds significant magnitudes for aging. At this point, the resistance of the bearings could be low enough to allow generation of CBC magnitudes sufficient to cause aging. However, because the studies in this chapter were conducted from the RF signal point of view, it was not exactly verified if there are

resistive periods in the active region in which $R_{b,min}$ is low enough to lead to a CBC sufficient to cause aging. Thus, it is uncertain whether CBC with an aging impact can occur during resistive-mode periods in the active region. For further tests on the feasibility of the introduced method, it is proposed that (unlike in the measurements presented in this doctoral dissertation) CBC events that do not have a slightest associated RF pulse should be included in the studies. As a result, higher CBC magnitudes should be obtained. Again, in order to confirm all these aspects, the reproducibility tests on the electrical behavior of certain types of bearings are considered mandatory. Nevertheless, since the main objective of the study was simply to verify whether RGC and CBC cause a detectable RF pulse in terms of the RF-SBBCDM, the frequency content of the signals involved in the CBC and RGC was not analyzed.

4 Electromechanical antenna simulation model of a motor

In this chapter, the operation of an induction motor as an RF signal transmitter is approached by an electromechanical antenna simulation model of the motor, later referred to as the 'motor antenna structure'. The study is considered crucial to gain knowledge of the RF radiation characteristics of a motor, thus supporting studies on the applicability of the RF-SBBCDM for bearing current detection and measurements. Hence, the objectives of the study can be set as follows:

- To verify the applicability of the simulation-based approach to the study of the RF signal transmitting properties of motor drive systems.
- To determine a feasible position for the receiver antenna to achieve the strongest possible signal strength.
- To determine a feasible frequency band for measurement.
- To determine the significance of the receiver antenna position in terms of signal strength deviation.
- To determine the effect of attaching a load machine on the signal strength and the position of the receiver antenna.
- To consider how the applicability of the RF-SBBCDM can be improved by the studies carried out in this chapter.

The research objectives listed above are studied by signal strength measurements (link budget) where the antenna properties of the $P_n = 15$ kW motor antenna structure are varied, and the detected changes are compared with the results given by the simulation model. In the simulation model verification measurements, two measurement procedures are carried out; outdoor measurements and laboratory measurements, each consisting of several measurement series. Based on the previous studies reported in (Särkimäki 2009), it is known that in the case of $P_n = 15$ kW motor, EDM generates a detectable RF pulse in the frequency range from 90 MHz to 400 MHz, which is used as the starting point in the studies. First, the antenna characteristics are studied in an outdoor environment, where the number of variables closely related to the EDM such as Z_{EDM} and the transmitted signal frequency are fixed. The parameter whose effect is studied in the outdoor tests is variation in the shaft length. By the procedure it is controlled that the corresponding changes in the simulation model produce similar results. After verifying the correspondence between the measurement setup and the simulation model, a load machine is attached to the model with different types of couplers, resulting in simulation-based values of the transmitting characteristics for different kinds of electric motor configurations (coupling to the load). The radiation pattern and the effect of the load machine are studied in the case of the $P_n = 15$ kW motor system in the laboratory environment. In this case, the radiation characteristics

are studied in a more practical way, since the signal source is the EDM event itself. The studies discussed in this chapter are based on Publications I and V.

4.1 Software and modeling

The antenna behavior of the $P_n = 15$ kW LVSCIM is modeled using the commercially available software EZNEC (EZNEC 2014). The software is based on a numerical electric code (NEC) calculation engine (Burke and Poggio, 1981b). In order to solve radiation pattern of complex model structures, the program, approaches the problem as a wired structure that is split into segments, which leads to a sum equation of incipient fields generated by each wire segment. The NEC also uses MFIE for surface analysis by estimating surfaces as wire grids and providing a reasonable accuracy between the simulation model and the corresponding actual antenna structure for far-field quantities. From the engineering point of view, the signal strength calculation is somewhat impractical in solving the integral equations involved in the radio signal radiation theory. Therefore, the problem is approached by applying the plane wave theory, according to which only the real part of the electric and magnetic fields as shown Eq. (1.17) can be radiated as a radio signal. In the case of a plane wave, which applies when $r \gg \lambda$ is met, the strengths of the electric and magnetic fields are always in a certain proportion to each other, which can be determined as the plane wave impedance, written as

$$Z_0 = \sqrt{\frac{\mu_0}{\varepsilon_0}} \, , \qquad\qquad (4.1)$$

resulting in $Z_0 = 377$ Ω. Thus, the RF signal strength in a certain far-field point generated by an individual dipole current element can be determined by (Barclay, 2013), and thus, the root mean square (rms) value for the signal strength can be calculated as

$$S_{rms}(r, \theta, \varphi) = \frac{1}{2} \cdot Z_0 \left| \frac{k_\lambda \cdot I \cdot \mathrm{d}l}{4\pi} \right|^2 \frac{\cos^2 \theta_e}{r^2} \, , \qquad\qquad (4.2)$$

where the propagation constant is $k_\lambda = 2\pi/\lambda$, and $\mathrm{d}l$ is the length of the dipole element. The parameters related to the field strength calculation for a certain far-field point in the case of a single dipole element are shown in Fig. 4.1a, where r is the distance between the source and the observation point in 3D spherical coordinates. Φ is the azimuth angle and θ_e is the elevation angle, which is alternatively given as an inclination angle θ_i. It is pointed out that for a signal strength calculation in the far field that is generated by a single dipole current element, the real part of the current should be substituted into Eq. (4.2). A detailed study of the mathematical background of the software calculation is not included in this dissertation; however, the mathematical theory behind the

calculation is comprehensively discussed for instance in (Burke and Poggio, 1981; Harish, Sachidananda, 2007; Barclay, 2013). Now, when the calculation of the incipient field generated by an individual current element is discussed, a segmentation and modeling principle can be introduced. An example of the wire structure segmentation is illustrated in Fig. 4.1b. The current distributions are not in a correct scale, but they are only depicted to demonstrate the cause-effect and propotion of the segment fields. The total field strengths are determined by superposition of the fields of each segment, thereby solving the transmitter antenna gain in a certain direction.
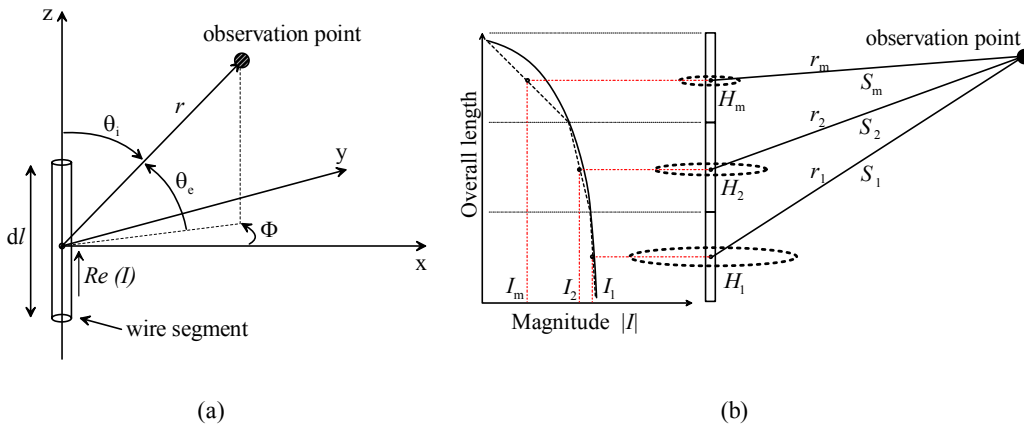

(a)   (b)

Fig. 4.1a. Parameters related to the far field signal strength calculation for a dipole current element. Φ is the azimuth angle and θ_e is the elevation angle. Fig. 4.1b. Structure of the wire segmentation and the current approximation for incipient H fields generated in each segment used in the EZNEC simulation software.

Moreover, the program computes the insertion loss I_L for the feed signal, because a constant input impedance for the whole studied frequency range is not likely to occur. Because of the limitations of the simulation software on the maximum diameter-to-wavelength ratio of single wire structures, the rotor circuit and the body of the motor as well as the ground plane below the DE shaft are modeled as wired structures. This is possible since in (EZNEC 2014) it is noted that conductive wall structures can be made by applying a wire grid, the diagonal length of which is $< 0.1\lambda$. However, the DE shaft of the $P_n = 15$ kW motor at its original length (12 cm) has a diameter-to-wavelength ratio $< 0.02\ \lambda$ (diameter of the shaft 42 mm and $\lambda_{min} > 85$ cm) and can thus be modeled by an individual conductive rod with a diameter of the shaft. The basic structure of the motor applied as the antenna model in this study is shown in Fig. C1 (Appendix C). The model consists of wires and lumped elements such as resistances, capacitances, and inductances. By using lumped elements, the effect of nonsimilarities such as the rotor-to-frame capacitance between the model and the corresponding motor can be reduced. Based on the model, the program calculates the 3D radiation pattern for the designed antenna structure and thereby the transmitter antenna gain G_t by solving the integral equations for the currents induced in the antenna structure by sources or incident fields.

Furthermore, it computes the antenna feed point impedance and the occurring insertion loss I_L as the RF power is supplied to the electric machine. An example of the 3D radiation pattern is shown in Fig. 4.2a, and the extracted 2D elevation projection in Fig. 4.2b. In the figure, the motor is placed so that the DE shaft is pointing to the direction of the positive x-axis. The best possible signal strength is found at the point indicated by a green dot.

(a)   (b)

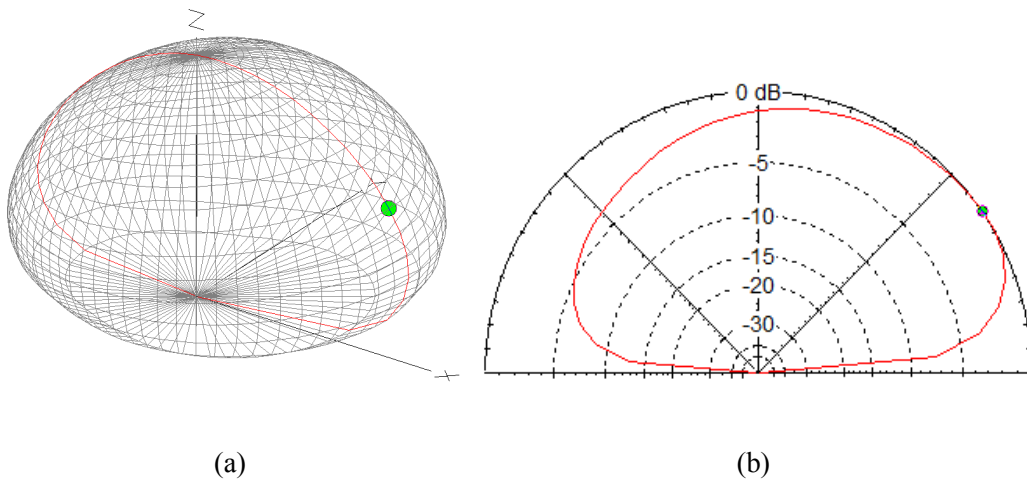Fig. 4.2a. 3D radiation pattern simulation of the standard P_n = 15 kW motor at 160 MHz and the x-axis projection of the 2D elevation angle projection (red). Fig. 4.2b. 2D elevation angle radiation pattern extracted from Fig. 4.2a. In Fig. 4.2b, the relative attenuation of each elevation angle compared with the best possible signal strength is illustrated on the decibel scale by the red curve.

4.2 Radiation pattern measurements in the outdoor environment

The simulated radiation characteristics are verified by measurements with the setup shown in Fig. 4.3 and the equipment introduced in Table C1 (Appendix C).

Fig. 4.3. Experimental measurement setup for link budget verification in the outdoor environment, where the transmitted signal is fed by an external signal source. In this measurement series, the motor was standing still and EDM was imitated by a 10 Ω shunt resistor assembled over the insulation of the DE bearing.

The study considers a frequency range from 30 MHz to 350 MHz. The criteria for the distance for the far-field region at a certain frequency is given in (Blake and Long, 2009) by

$$r \geq \frac{2D^2}{\lambda}.$$
(4.3)

With the maximum opening $D \leq 1$ m, the shortest wavelength $\lambda \geq 0.85$ m (350 MHz) results in $r \geq 2.35$ m. On the other hand, in order to study radiation as a plane wave, according to (Barclay) $r \gg \lambda$ should apply. Because of the limited space on the measurement site, it was decided that the criterion of Eq. (4.3) has to be met. Therefore, the distance r between the feed point (of the transmitting antenna, the electric motor) and the receiver antenna is kept constant at three meters. The maximum opening D of the transmitting antenna was approximated as an overall length of the frame and the DE shaft. The analysis and further comparison between the values given by the simulation model and experimentally measured values is based on a link budget measurement, where the transmitted and received powers are measured with one MHz steps over the frequency range from 30 to 350 MHz. Based on the measurements, the link budgets for each frequency (total gain) are computed by

$$A = 10 \cdot \log_{10}\left(\frac{P_{\text{out}}}{P_{\text{in}}}\right), \tag{4.4}$$

since the measured values P_{in} and P_{out} correspond to the transmitted and received powers P_{t} and P_{r} of Eq. (3.2) and

$$A = 10 \cdot \log_{10}\left(\frac{P_{\text{t}}}{P_{\text{r}}}\right) = 10 \cdot \log_{10}\left(I_{\text{L}} G_{\text{t}} G_{\text{r}} \left(\frac{\lambda}{4\pi r}\right)^2\right). \tag{4.5}$$

With the attenuation of free space $(\lambda/(4\pi r))^2$, the gain of the receiving antenna G_{r}, known from the datasheet (ETS, 2011), the computed gain of the transmitting antenna, and the insertion loss I_{L}, the simulated and measured link budgets can be compared. To accomplish the verification procedure, the shaft of the motor was artificially extended by a cylinder made from a thin copper plate. The standard length of the DE shaft is 12 cm, whereas the length of the extended shaft is 41 cm. Based on this information, the criterion for the selection of the extension length was set simply so that the original length << the extended length. This was done in order to verify the role of the DE shaft as the monopole-type transmitting element; in addition, with the corresponding changes in the simulation model and the experimental test setup, similar changes in the link budgets are obtained. The original shaft and the extended version of the shaft assembly are shown in Fig. C2a and Fig. C2b (Appendix C). In the verification measurements, the signal strength was measured at seven elevation angles as illustrated in Fig. C3 (Appendix C). Moreover, remembering that the transmitting antenna properties of the motor should imitate the circumstances in which EDM occurs, an additional resistor to imitate $Z_{\text{b,EDM}}$ was implemented as shown in Fig. C4 (Appendix C).

4.3 Verification of the transmitted signal characteristics of EDM in the laboratory

In addition to the radiation pattern verification tests in the outdoor environment, where equal conditions for measurement were considered essential, laboratory measurements were carried out where the transmitted signal is generated by EDM when the $P_{\text{n}} = 15$ kW motor was driven by a VSI. First, verification tests were performed to verify the dependency between the magnitude and frequency content of the U_{b} and I_{b} on the transmitter side and the corresponding RF signal in U_{RF} on the receiver side. The selection of the frequency band was based on the simulated input impedance of the motor antenna structure. The input impedance was calculated in the case where the source is attached directly inside the DE bearing, where the EDM discharge is likely to occur. According to the simulated input impedance shown in Fig. 4.4a, it can be expected that the motor antenna structure is in series resonance at 135 MHz and 165 MHz. Thus, one or both of these frequencies should be present when considering

the frequency content of the EDM events. Furthermore, in order to simplify the analysis, only one of the possible resonant frequencies was involved in the study. Hence, 135 MHz was selected for the analysis because of its better compatibility with the frequency response of the current probe applied to the I_b measurement. The measurement was carried out with the measurement setup illustrated in Fig. 4.4b and the equipment described in Table C2 (Appendix C).
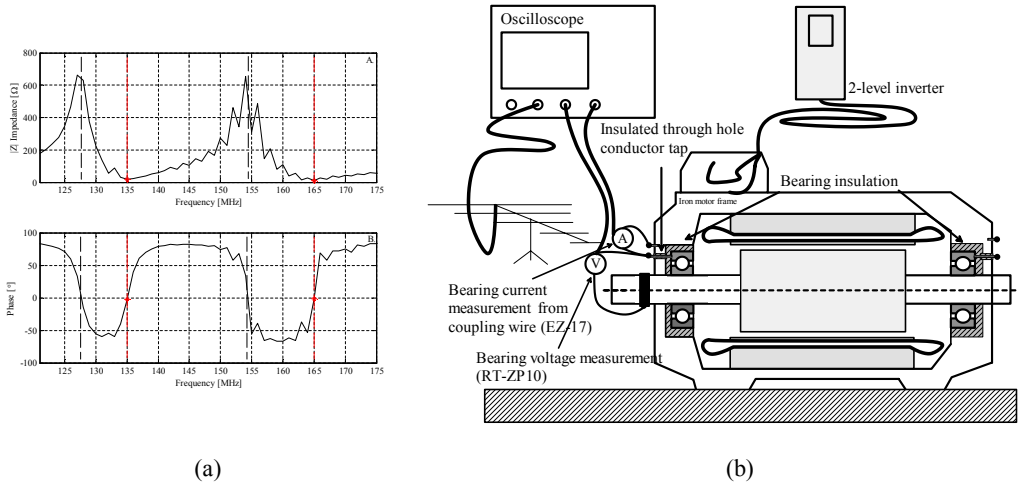

(a)   (b)

Fig. 4.4a. Simulated $P_n = 15kW$ motor impedance in the frequency domain when analyzed from the DE bearing. Serial resonances (red) can be found around 135 MHz and 165 MHz. The impedances are $19.5-j0.9$ (at 135 MHz) and $11.8-j0.3$ (at 165 MHz). In addition, parallel resonances are detected (dashed black) ~127 MHZ and ~154 MHz. Fig. 4.4b. VHF oscillation measurement setup.

For an experimental study, a set of four EDM events were measured, and the signal waveforms of U_b and U_{RF} were filtered by a band-pass filter of $f_c = 135$ MHz and a pass band $BW_{Att <-1dB} = 130–140$ MHz. For the study, based on the datasheet of the current probe (EZ-17, 2005), the transfer impedance of the probe can be determined by

$$k = 20 \cdot \log_{10}\left(\frac{1}{Z_t}\right). \tag{4.6}$$

As the oscilloscope measures the voltage signal $U_{Ib,VHF}$, it has to be translated into a corresponding current value by

$$I_{b,VHF} = \frac{U_{Ib,VHF}}{Z_t}. \tag{4.7}$$

This applies in the case of EZ-17 (probe ver. 2); if $f \geq 10$ MHz, then $Z_{\text{out, EZ-17}} = 50\ \Omega$, and $k \approx -8\ \text{dB}_{(BW:130-140\ \text{MHz})}$ can be obtained from the probe datasheet.

After verifying the dependency between the simulation model and the experimental tests in the case of the VHF oscillation frequency, the signal strength differences were verified as a function of position of the receiving antenna in the application-level circumstances. The same simulation model that was applied to study the motor antenna VHF oscillation was used to simulate the radiation patterns of two different measurement setups: the motor without a load and the motor with a load machine, which is attached with an insulated shaft coupler. An illustration of the simulation model for the motor with the load machine attached by a galvanic coupling is presented in Fig. C5 (Appendix C). In the case of the load machine, only the end plate is included in the model. There are two reasons for this: first, it is assumed that it has the highest effect on the radiation charasteristics of the system, and second, the maximum number of wires that can be used in the simulation model was exceeded. Therefore, in order to minimize the effects of individual differences in EDM pulses and to reinforce the common features, ten EDM pulses from each radiation angle $(\theta_e = 20°/90°/160°, \Phi = 0°)$ were recorded. Furthermore, in each case $U'_b = 10$ V ± 0.1 V was required. It is pointed out that in the directivity studies U_{RF} is not filtered by other filters than the band-pass filter used in the RF-SBBCDM ($BW_{U_{\text{RF}}} = 90-400$ MHz). In addition, the motor was stopped while the position of the receiving antenna was changed. This was done in order to minimize variation in the circumstances inside the motor system such as warming of the bearings. Now, the directivity and the effect of the load machine are studied by power and energy parameters of the received RF pulses. For this purpose, the received RF pulse peak power is introduced

$$\hat{P}_{\text{RF}} = \frac{\hat{U}_{\text{RF}}^2}{Z_{\text{OSC}}}, \tag{4.8}$$

where $Z_{\text{osc}} = 50\ \Omega$ and the average of the peak power values is obtained by

$$\hat{P}_{\text{RF,ave}} = \frac{1}{M} \sum_{M=1}^{M=10} \hat{P}_{\text{RF}}(M), \tag{4.9}$$

where M is the number of pulses involved in the analysis. The RF pulse energy is calculated as a sum equation of the samples of the RF pulse

$$E_{\text{RF}} = \sum_{m=1}^{m=N} \frac{U_{\text{RF}}^2(m)}{Z_{\text{OSC}}} \cdot t_s, \tag{4.10}$$

where the sampling time $t_s = 1/f_s$ and N is the number of samples in an individual RF pulse. The length of the RF pulse was determined by the signal threshold level, which

was set to $U_{th} = 2$ mV. Therefore, the signal emerging from the noise and exceeding the required threshold level was set as the start point for the received RF pulse. The end of the RF pulse was acquired similarly by determining the point where the RF signal submerges in noise. It is also noted that a similar mean value equation as Eq. (4.9) is used for the average pulse energy calculation. The measurement setups used in the laboratory for directivity studies are illustrated in Fig. 4.5a for the motor without a load and Fig. 4.5b for the motor with a load machine. In both cases, the distance between the motor and the receiving antenna was set to 3 m. Photograps of the measurement setup are shown in Fig. C6a and Fig. C6b (Appendix C).
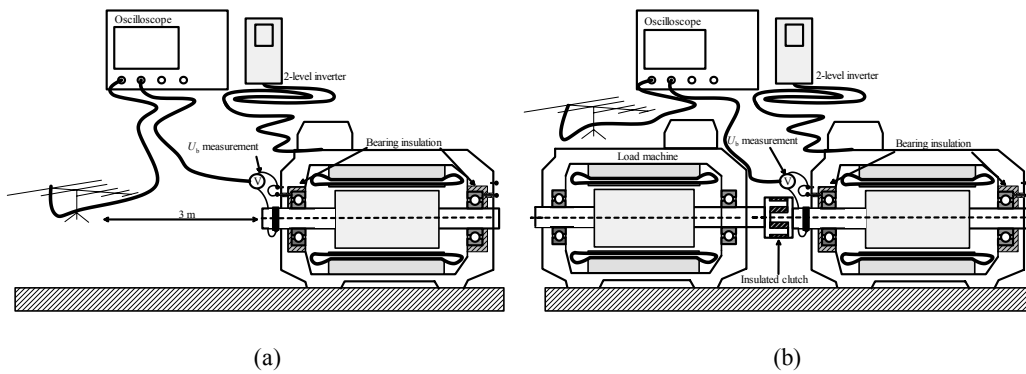

(a)   (b)

Fig. 4.5a. Directivity measurement setup for the motor without a load. Fig. 4.5b. Directivity measurement setup for the motor with a load machine attached with an insulated shaft coupler.

4.4   Results

An example case on the measured link budget frequency response of the motor antenna structure for an extended shaft, Fig. C2b (Appendix C), and the corresponding simulation-based curve are shown in Fig. 4.6. In addition, the results of the measured transmitter antenna gains and the corresponding values given by the simulator at each elevation angle for the external transmit signal measurements in the outdoor environment are summarized in Table 4.1. The motor with the original shaft length is shown in Fig. C2a (Appendix C) and the extended shaft in Fig. C2b (Appendix C). In addition,
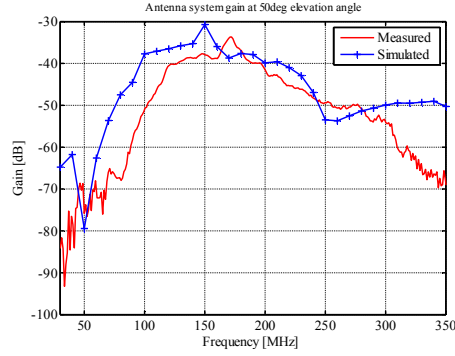
Fig. 4.6. Measured and simulated antenna system gains for the extended shaft (41 cm) at a 50° elevation angle.

Table 4.1. Comparison of the measured and simulated gains for outdoor measurements.

	Simulation standard shaft	Measurement standard shaft	Simulation extented shaft	Measurement extented shaft
Peak gain at the best elev. angle [dBi]	−40	−44	−31	−34
Elevation angle for peak gain [°]	35	50	58	50
≤ |1 dB| elevation angle range [°]	18–85	(N/A)	20–97	(N/A)
Peak gain frequency at the best elevation angle [MHz]	160	171	150	172
Peak gain at the worst elev. angle [dBi]	−51	−51	−39	−35
Elevation angle for the lowest gain [°]	170	170	20	80
Peak gain frequency at the worst elevation angle [MHz]	170	164	150	170

In the laboratory measurements, the dependency shown in Fig. 4.7 between the transmitted and the received signal can be derived. It is pointed out that the $I_{b,VHF}$ and $U_{b,VHF}$ waveforms are not necessarily in an actual phase, since the propagation delay between the measurement channels was not verified. The phase difference, which is crucial here, is constant in all cases when considering the $U_{b,VHF}$ and $I_{b,VHF}$ measurements.
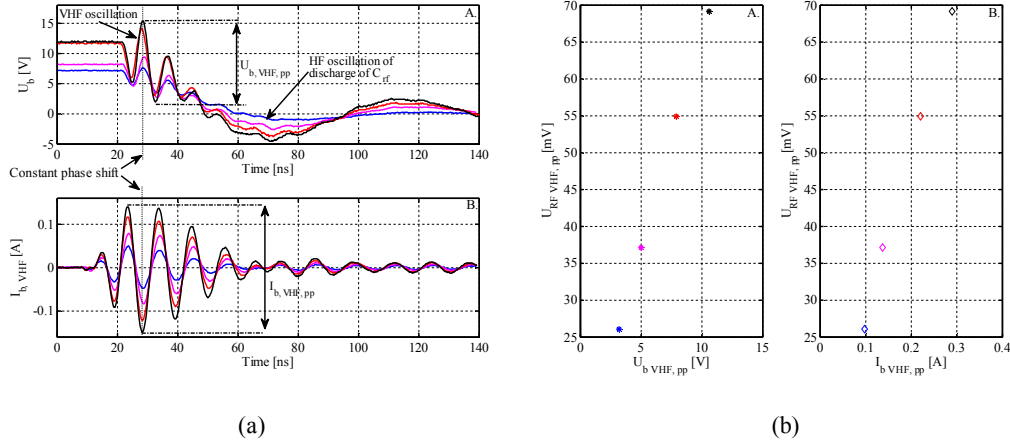
(a)   (b)

Fig. 4.7. VHF oscillation measurement of EDM discharges. Fig. 4.7a. Subplot A: Original measured U_b waveforms with different amplitudes of $f_c = 135$ MHz oscillation (not filtered); subplot B: band-pass-filtered $I_{b,VHF}$ signals at $f_c = 135$ MHz EDM current pulses. Fig. 4.7b. Received $U_{RF,VHF,pp}$ signal levels as a function of $I_{b,VHF,pp}$ and $U_{b,VHF,pp}$. Subplot A: the dependency between $U_{b,VHF,pp}$ and $U_{RF,VHF,pp}$ of the filtered signals at $f_c = 135$ MHz. Subplot B: the dependency between the corresponding $I_{b,VHF,pp}$ and $U_{RF,VHF,pp}$ of the filtered signals at $f_c = 135$ MHz.

The simulated maximum and minimum system gains and the corresponding elevation angles for the three electric motor configurations are listed in Table 4.2.

Table 4.2. Simulation results for different load couplings.

	Motor only	With noninsulated coupling	With insulated coupling
$H_f = 160$ mm, $P_n = 15$ kW, $f = 135$ MHz			
Peak gain at the best elev. angle [dBi]	−30	−4	−4
Elevation angle for peak gain [°]	110	94	95
≤ |1 dB| elevation angle range [°]	89–132	73–118	73–117
Peak gain at the worst elev. angle [dBi]	−39	−12	−12
Elevation angle for the lowest gain [°]	170	170	170

Based on the laboratory measurements, where the average signal strength values of ten EDM events at each elevation angle were compared, the directivity values shown in Table 4.3 and Table 4.4 can be derived. It is pointed out that the EDM events in the case of a noninsulated shaft coupler could not be measured. This is propably explained by the low-impedance grounding path through the load machine.

Table 4.3. The highest signal strength differences of the EDM events.

Classification	Motor only	Motor with insulated coupler
Average pulse energy difference 90°/160°	5.6 dB	6.1 dB
Average peak power difference 90°/160°	7.8 dB	8.9 dB

Table 4.4. Average pulse energies in different elevation angles and drive system configurations.

Elevation angle[º]	Average RF pulse enegy [pJ]: Motor only	Average RF pulse enegy [pJ]:Motor with load	Signal strength difference between drive system layouts [dB]
Front (20°)	0.173	71	25.8 dB
Above (90°)	0.211	98	26.7 dB
Rear (160°)	0.058	24	26.4 dB

Based on the results given above, the influence of the different motor setup configurations on the electric motor transmitting characteristics can be summarized as follows:

- The system peak gain increases if a load machine with conductive parts is attached. According to the results given by the simulation model and the corresponding laboratory tests, it is proposed that the increment is approximately 25 dB. This is explained by the increase in the radiation resistance of the machine antenna structure.

- When the gain of the antenna system is studied at $\Phi = 0º$ and $\theta_e = 0–180º$ (projection illustrated in red in Fig. 4.3), when compared with the maximum attenuation of −1 dB with reference to the maximum gain, the gain is close to its maximum value in the radiation angle range $> 30º$. Thus, the best location for the receiver antenna is in the range of elevation angles $\theta_e = 70–120º$.

- Based on the laboratory measurements, it is verified that a deviation in the signal peak value can be up to 8 dB in the case of a motor without a load and up to 9 dB in the case of a motor with a load as a function of receiver antenna position. In practice, a deviation of this range would either mean a lack of pulse detection or a significant decrease in the signal-to-noise-ratio.

4.5 Conclusions

The studies carried out in this chapter showed that it is possible to estimate a feasible frequency span in which the RF-SBBCDM should be tuned in order to detect EDM discharges as effectively as possible. Further, the best signal strength for the RF-SBBCDM can be achieved when the receiving antenna is placed above the shaft of the motor. Based on our studies, up to 9 dB signal strength differences can be obtained depending on the motor drive configuration and the position of the receiving antenna. Moreover, based on the laboratory tests, regardless of the elevation angle, the difference in the signal strength between nonloaded and loaded motor systems is nearly 26 dB. The difference is well in range with the simulation model. In general, based on the signal strength differences obtained by the studies, the position of the receiving antenna can be considered significant from the perspective of RF-SBBCDM, since a wrong position may lead to an insufficient signal-to-noise-ratio for EDM pulse detection. Because

similar results are suggested by the simulation model and the experimental measurements, we may suggest that a simulation-based approach could be used for radiation characteristic studies on motor drive systems. However, in order to improve the simulation accuracy, more detailed models are needed, which will require for instance a program version that allows the use of 1500+ wires in the model. Considering the uncertainty of the field strength analysis, there are a few aspects to be taken into account: first, the verification measurements were performed with a vertically polarized antenna while the field strength values obtained by a simulator were associated with the overall signal strength. Thus, it is proposed that the accuracy between the measurement and the simulation can be improved by a different antenna structure that is not so sensitive to signal polarization. In general, it is suggested that an electromechanical simulation-model-based approach adopted from RF engineering is applicable to studies on the side effects and RF radiation charasteristics of modern electric motor drive systems. Moreover, the introduced approach can be considered feasible when electromagnetic interference (EMI) related issues of modern VSI-driven motor systems are studied.

As to an EDM discharge, the HF waveform is determined by a circuit that discharges the main energy storage C_{rf}. In addition to that, it is shown by an electromechanical simulation model and an analysis of experimental measurements that there could be electrical resonant circuit structures that are set to oscillate at their VHF resonant frequencies as a result of the discharge. Based on the preliminary study carried out in this doctoral dissertation, the magnitudes of the received RF pulses are shown to be proportional to the amplitude of the oscillation of the proposed VHF resonant circuit. It is noted that in most of the cases, more than one VHF frequency is likely to be associated with an individual EDM discharge, thereby making analysis more difficult in practice. It is also noteworthy that the signal transmitted from the motor does not necessarily correspond to the frequency at which the antenna gain is the best possible. Furthermore, it is pointed out that the dependency between the nonfiltered I_{b} (conventional) in the motor and the received RF pulse is not studied or verified. It is likely to differ from the corresponding intrusively measured I_{b} value, since only the dependency between the signal content in the narrow ($130 \leq BW_{\mathrm{Att}\ <-1\mathrm{dB}} \leq 140$ MHz) VHF range is studied.

Based on the above findings, studies on the effect of the value of the Z_{EDM} on $U_{\mathrm{RF,pp}}$ could be advisable in order to improve the applicability of the RF-SBBCDM as well as maybe to apply the method as a supplementary measurement for nonintrusive, simulation-model-based bearing current magnitude estimation. This study is, however, far beyond the scope of this doctoral dissertation.

5   Application of nonintrusive HFMNFP to EDM current magnitude measurements

In the previous chapters of this doctoral dissertation, starting from the introduction, it is emphasized that the nonintrusive method for measuring EDM bearing current magnitude is independent of deviations in the EDM-current-related parameters of a motor. Nonintrusive measurement of the EDM bearing current magnitude would be beneficial for maintenance and diagnostic purposes. The method is proposed to enable estimation of the current magnitude and the distribution of current pulses in the magnitude-quantity plane. Based on the current knowledge of the applicability of the RF-SBBCDM, it is suggested that the method is not directly applicable to bearing current magnitude measurements. As stated above, the different approaches have their disadvantages and limitations such as intrusive coupling, fixed operating parameters, or operating point assumption. This can partly explain why equations related to bearing current aging impacts such as Eq. (1.6–1.8) are based on an assumption that the determined peak current amplitude is constantly present. The problem is that the magnitude and the DA of the EDM bearing currents are likely to vary all the time. This degrades the accuracy of the analytical bearing wear approximation. When considering the aging impact of EDM bearing currents, besides the deviation in the peak value of current pulses, the number of EDM events that have reached a certain level has to be taken into account. Thus, the number of each pulse in each aging impact classification (Table 1.1) will count. As shown in the previous chapters, because the EDM DA is dependent on various parameters, the reproducibility of the EDM DA remains uncertain and calls for continuous bearing current monitoring.

This chapter focuses on a sensor that would enable effective nonintrusive bearing current monitoring, which is based on the peak value measurement of individual EDM pulses. The study aims at the design, development, and verification of the applicability of a nonintrusive magnetic near-field probe. The applicability of the probe is verified by experimental studies, where the magnitudes of individual EDM current pulses measured by the nonintrusive probe are determined by a simultaneous intrusive reference measurement. In addition, it is studied whether the accuracy of the designed probe is adequate for aging impact classification according to Table 1.1. It is also investigated how a feasible frequency band can be determined based on the FFT analysis of an arbitrarily selected EDM discharge and how the probe can be tuned by experimental measurements. An advantage is that the sensor could be applied to series production motors. The questions addressed in this section are based on studies discussed in Chapter 3 and publication (VII).

In the near-field (NF) region, as determined in Eq. (4.3), unlike in the far field, there is no certain ratio between the magnetic and electric fields, and these fields are not necessarily in the same phase. Since the ratio and phase of the fields are determined by the impedance of the measured circuit, the fields can have arbitrary values compared with each other. Therefore, considering the current measurement, the NF coupling of

the probe has to be through the magnetic field, leading to a design of an inductive coil probe. In the NF region, the magnetic field generated by the surface current can be calculated by

$$H = \frac{1}{4\pi} \int_{A_s} \frac{J_{A_s} \times u_r}{r^2} \mathrm{d}A_s \, , \tag{5.1}$$

where J_s is the surface current of the studied surface area A_s, u_r is the unit vector that points towards the observation point, and r is the distance between the surface area and the observation point. Additionally, since the magnetic field attenuates by $1/r^2$, in order to achieve the best possible signal levels, the probe has to be placed as close as possible to the surface of the end-plate of the motor. Again, compared with an air-wound coil, coupling to the magnetic field can be improved by applying a core made of an appropriate ferrite material (Guru et al., 2001). This can be seen from

$$B = \mu_o \mu_r H \, , \tag{5.2}$$

where the magnetic flux density B can be obtained by increasing the relative permeability of ferrite μ_r. It should be noted that $\mu_r > 1$ in order to achieve an improvement compared with the air core. In addition, unwanted coupling of the electric field can be reduced when assuming that the coupling with the electric field is independent of the core material. The ferrite material is chosen according to the desired frequency range. Therefore, as a preliminary study, in order to determine an appropriate band for the ni-HFMNFP measurement, an arbitrarily selected EDM pulse was analyzed in MATLAB[®], where the band-pass filter (BPF) was tuned so that $I_{de, pp}$ equals the $|\hat{I}_{de}|$ value. According to the FFT analysis, the frequency content of the EDM pulse can be defined as shown in Fig. D1 (Appendix D), and thus, we may conclude that the measurement of the magnitude of the EDM bearing current pulses sets a 5–30 MHz bandwidth requirement. Hence, the EDM current pulse magnitude can be reproduced. The voltage induced in the winding of the ni-HFMNFP can be estimated based on the approximated magnetic field strength. The surface-segmentation-based calculation of the magnetic field is illustrated in Fig. 5.1.
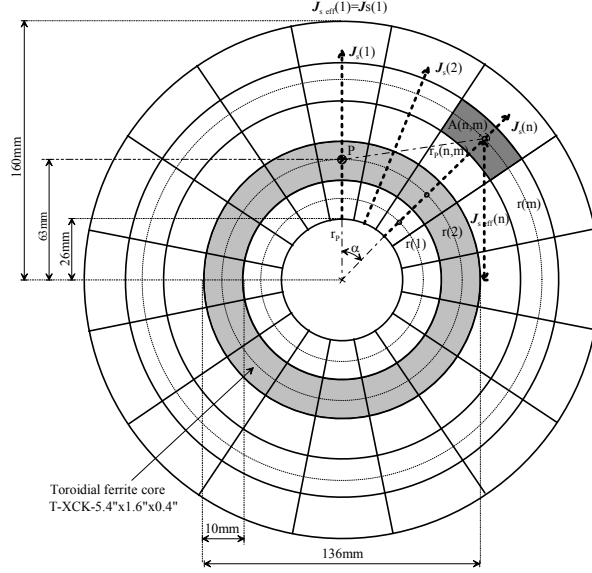
Fig. 5.1. Segmentation of the DE plate.

Since the currents in each sector are running in different directions, they are at different angles to the point P. When considering the 2D-plane illustration shown in Fig. 5.1 and taking into account that according to Lenz's law, the magnetic field that couples to the ferrite has to be parallel to it, each cell from a certain direction substitutes the field strength according to its effective current term as

$$J_{s,eff}(n) = J_s(n) \cdot \cos(\alpha \cdot (n-1)),$$

(5.3)

where α is the angle between the direction of the point P from the origin and the direction of the incipient current vector $J_s(n)$ from the origin ($\alpha = 5.625°$). Finally, the complete magnetic field strength is calculated by

$$H_p = \frac{1}{4\pi} \sum_{n=1}^{n=64} \sum_{n=1}^{r=15} \frac{J_{s,eff}(n) \cdot A_s(r)}{r_p^2(n,r)}$$

(5.4)

where A_s is the area of an area cell, and r_p is the 3D diagonal distance between the center of an area cell and the point P. With the total current of 1 A, the magnetic field strength in the point P is 0.068 A/m. In ideal conditions, the same magnetic field strength will affect in every direction at the distance of P from the origin. Now, according to Maxwell's induction law, the peak value of the electromotive force e for a sinusoidal signal can be calculated for a coil with multiple turns as

$$\hat{e} = -2\pi f \cdot N_{wt} \cdot \hat{B}_f \cdot A_f, \tag{5.5}$$

where A_f is the cross-sectional area of the ferrite core and B_f is the magnetic flux density in a ferrite core. The manufacturer of the ferrite core also gives $\mu_i \approx 125$ in the frequency band in the range of 1–30 MHz (CMI magnets, 2014). In practice, a coil with $N_{wt} = 10$ turns was wound and analyzed in the case of a signal frequency $f = 15$ MHz, thus resulting in $|\hat{e}| \approx 4.9$ V. In addition, it is verified that the band-pass frequency of the low-pass RL circuit does not restrict the desired measurement band (5–30 MHz). The reactive impedance of the ni-HFMNFP can be solved by

$$X_L = 2\pi f \cdot N_{wt}^2 \cdot A_L, \tag{5.6}$$

where A_L is the inductance of an individual winding turn around the ferrite core, obtained from the datasheet provided by the manufacturer of the ferrite core ($A_L = 100\pm20$ nH/N^2 in 1–30 MHz) (CMI magnets, 2014). Now, when the voltage probe of an oscilloscope with a load impedance of $Z_{probe} = 10$ MΩ is connected to the ni-HFMNFP, the band-pass frequency does not restrict the bandwidth if $Z_{probe} \gg X_{L,\,NFP}$ applies at the highest frequency of the desired measurement band. This holds true when it is assumed that the resistance in the ni-HFMNFP section and the reactance in the voltage probe of the oscilloscope are negligible. Thus, it is verified that at the 30 MHz frequency, the desired $N_{wt} = 10$ winding turns does not restrict the measurement band

$$Z_{probe} \gg 2\pi f \cdot N_{wt}^2 \cdot A_L. \tag{5.7}$$

The result of 10 MΩ $\gg$ 2262 jΩ is obtained when $A_L = 120$ nH/N^2 is applied. For an input impedance measurement, a linear frequency sweep from 1–35 MHz is injected to the terminals of the ni-HFMNFP with the measurement equipment listed in Table D1 (Appendix D). The input impedance and phase measurement of the ni-HFMNFP is shown in Fig. 5.2. As it can be seen, the input impedance of the ni-HFMNFP is inductive up to 20 MHz.

The result corresponds with the measured input impedance of the ni-HFMNFP, which is shown in Fig. 5.2. However, it can also be seen that because of the stray capacitances that are probably involved in the ni-HFMNFP (the equivalent circuit is presented in Fig. D3 (Appendix D)), the input impedance is somewhat different compared with the calculated values. For example, in an ideal case, at 15 MHz, the input impedance should be 1130 jΩ, but according to the measurement, the impedance is approximately 2000 jΩ.
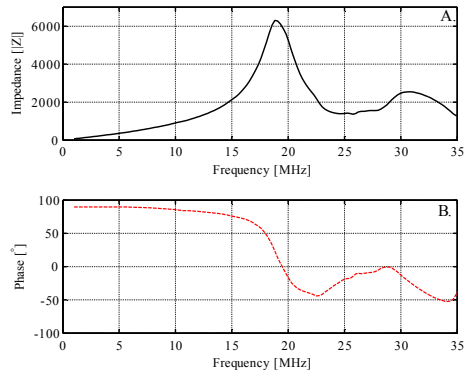
Fig. 5.2. Input impedance of the nontuned (5–30 MHz) ni-HFMNFP in the frequency band of 1–35 MHz.

The final adjustment to the number of applied winding turns was based on a gain-phase measurement, according to which the number of the winding turns of the ni-HFMNFP was set to seven. The selection was based on the lowest deviation in the gain and phase within the desired frequency range. It was assumed that a reduction in the winding turn number would not increase the input impedance of the ni-HFMNFP, and therefore, the pass-band criteria would also be satisfied. The measurement setup is illustrated in Fig. 5.3a and the measurement equipment listed in Table D1 (Appendix D). The gain and phase response of the tuned ni-HFMNFP is shown in Fig. 5.3b.
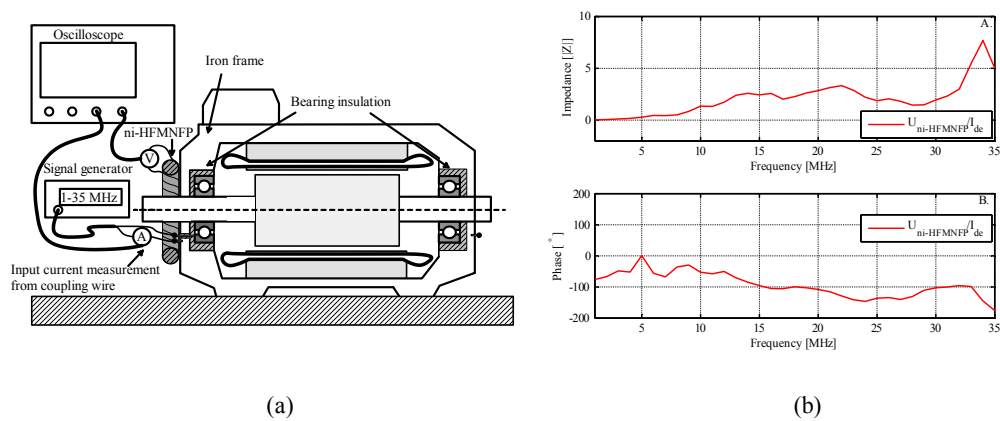

(a)   (b)

Fig. 5.3a. Gain and phase measurement setup for tuning the ni-HFMNFP. The motor is stopped during the gain phase and the measurements of the ni-HFMNFP are measured in its assembly position on the DE plate of the motor. Fig. 5.3b. Gain and phase response of the tuned (5–30 MHz) ni-HFMNFP on the DE plate in the frequency band of 1–35 MHz.

Next, the motor was driven by a VSI. The measurement setup is illustrated in Fig. 5.4. The measurement equipment is listed and a photograph of the measurement system assembly in the laboratory is shown in Table D1 and Fig. D2 (Appendix D). During the tests, EDM current pulses were measured simultaneously as I_{de} by an intrusive current probe assembled around the shorting wire of the bearing insulation and by the ni-HFMNFP as $U_{ni\text{-}HFMNFP}$ on the DE plate of the $P_n = 15$ kW motor. The motor was set to run at $n = 1500$ rpm, and the current waveforms from 30 EDM pulses were recorded. The dependency between the peak-to-peak values of the BPF (5–30 MHz) $I_{de,pp}$, and $U_{ni\text{-}HFMNFP,pp}$ is shown in Fig. 5.5a. Similarly, the dependency between the absolute peak value of the original EDM bearing current pulse $|\hat{I}_{de}|$ ($BW = $ DC–100 MHz, no additional filters applied) and the BPF $U_{ni\text{-}HFMNFP,pp}$ is shown in Fig. 5.5b.

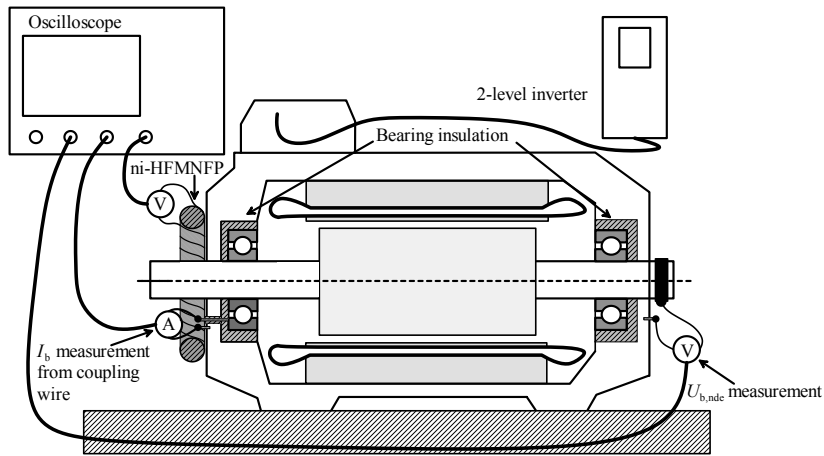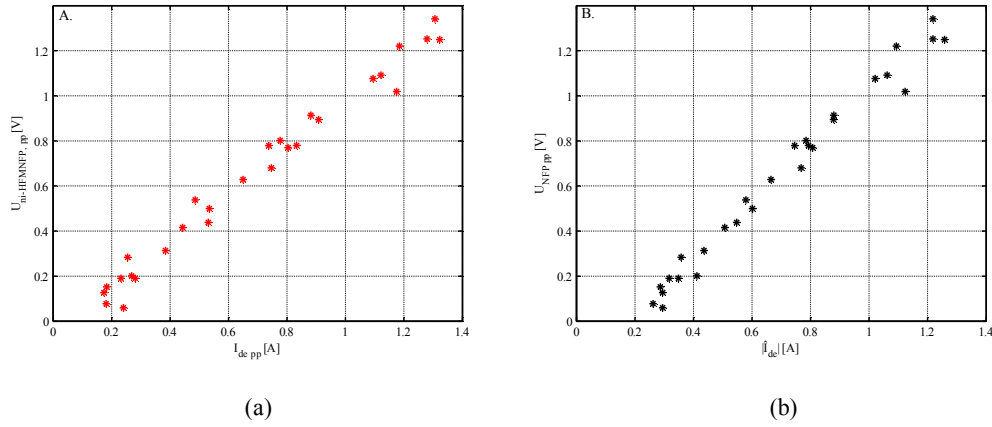Fig. 5.4. Comparative measurements of the intrusive and ni-HFMNFP bearing current measurement methods.

(a)   (b)

Fig. 5.5a. Dependency between BPF $I_{de,pp}$ and $U_{ni\text{-HFMNFP, pp}}$. Fig. 5.5b. Dependency between $|\hat{I}_{de}|$ and $U_{ni\text{-HFMNFP, pp}}$.

5.1 Results

Based on the studies carried out in this chapter, it is proposed that the ni-HFMNFP can be applied to the nonintrusive measurement of the EDM current pulse magnitude. The signal magnitude can be reproduced by the measurement that is executed in the frequency range of 5–30 MHz. The applicability of the frequency range is verified for the $P_n = 15$ kW ($H_f = 160$ mm) LVSCIM. The effects on the applicability of the ni-HFMNFP that may be caused by a change in the motor dimensions were not studied and are left for future work. Based on the theory of the magnetic circuit design (Guru et al., 2001), it is proposed that the magnetic field coupling can be improved by applying an appropriate ferrite core material, thereby achieving an improved signal strength compared with an air-wound coil. In addition, uncertainty caused by the coupling with the electric field is reduced as a result of the improved magnetic field coupling. This is based on the assumption that the electric field coupling through stray capacitances to the ni-HFMNFP is independent of the core material. The uncertainty values calculated based on the measurement data are listed in Table 5.1. The uncertainty analysis is based on the calculation shown in Appendix D (see Uncertainty, Fig. D4, and the Matlab script for EDM pulse processing).

Table 5.1. Uncertainty values obtained from the NFP measurement data set.

	The highest absolute uncertainty [V/A]	The highest relative uncertainty [p.u]	Amount of EDM with relative uncertainty $\leq \pm 10\%$
$\dfrac{\left\|\Delta U_{ni\text{-HFMNFP,pp}}\right\|}{I_{de,\,pp}}$	0.093	1.6	85 %
$\dfrac{\left\|\Delta U_{ni\text{-HFMNFP,pp}}\right\|}{\left\|\hat{I}_{de}\right\|}$	0.097	0.83	90 %

Based on the gain response illustrated in Fig. 5.3b, it can be stated that the ni-HFMNFP has a gain deviation in the range of three in the linear scale within the desired measurement band (5–30 MHz). It will inevitabely increase the uncertainty of the measurement. Still, with the determined accuracy, the bearing current pulses could possibly be classified according to their aging impact as shown in Table 1.1. Furthermore, when considering the electrical aging impact on the lifetime estimation of a bearing proposed in Eq. (1.6) and based on the measurement series shown in Fig. 5.3a and Fig. 5.3b, it is demonstrated how the magnitude of the bearing current pulses deviates within the measurement series. Thus, it is proposed that in the case of the EDM, where the magnitude distribution of $\hat{J}_b$ is likely to vary significantly, especially in cyclic operation, the $\hat{J}_b$ term in the equation could possibly be improved with

$$\hat{J}_{b,ave} = \frac{1}{M} \sum_{M=1}^{M \to} \left| \hat{J}_b(M) \right|.$$

(5.8)

This is when assuming that the aging impact is a linear function of $\hat{J}_b$. The significance of the amount and magnitude of EDM current pulses for its aging impact is also reported for instance in (Kriese et. al., 2012). Therefore, further studies on the subject are required.

The results given in this chapter are based on a comparison of the signal levels that are obtained by conventional intrusive and nonintrusive measurements. The ni-HFMNFP is designed, tuned, and tested to reproduce a signal magnitude that is measured within the pass band of the intrusive measurement (DC−100 MHz). Therefore, it is pointed out that even if the measured current magnitude values obtained by the ni-HFMNFP are well in line with the intrusive reference measurement, neither of these measurements take into account the effect of additional VHF signal components. This is an aspect that is not considered in the reference publications based on which Table 1.1 is constructed. Therefore, depending on the phase shift of the HF current pulse and the VHF current pulse, it is assumed that uncertainty is involved in the measurements. Consequently, the total wideband (DC−200 MHz) EDM current pulse magnitude can deviate, and thus, $\hat{I}_b = \hat{I}_{ni\text{-}MNFP,pp} \neq \hat{I}_{b,HF+VHF}$ can be noted. Nevertheless, it is too early to say anything about the significance of the matter. Further studies on the subject are recommended, and for the sake of convenience, an active current probe that meets the band width criteria ~DC−200 MHz is suggested to be applied. In addition, in the nonintrusive measurement, a probe applying Rogowski coil could be tested because of its more linear frequency response compared with a probe equipped with a magnetic material core as discussed in section 1.3.1.

5.2 Conclusions

In this chapter, a novel approach to measure the magnitude of the HF EDM bearing currents with the nonintrusive ni-HFMNFP on the surface of the motor end plate was designed and tested. When properly tuned to the right frequency range, it is possible to obtain the magnitude of individual EDM bearing current pulses. The final tuning of the ni-HFMNFP was based on the magnitude-phase measurement. The general applicability of the method was not verified, in other words, it was not tested whether tuning is needed in each individual motor and what the effects would be on uncertainty. The accuracy of the ni-HFMNFP can be improved by paying attention to the appropriate probe design. For example, a wider bandwidth with a fixed gain and phase response is desirable, not to mention a possible improvement that may be achieved by modifying the form of the core structure such that the magnetic field coupling is improved even further. On the other hand, if the ~DC−200 MHz bandwidth criteria in the EDM current measurement will turn out to be crucial in order to improve the accuracy of the aging impact analysis, the applicability of any toroid material may become somewhat difficult and questionable. In that case, studies regarding the applicability of air-wound coils (Rokowski coil) may come into guestion. Moreover, in any case where a wider bandwidth is needed for the measurement, the frequency equalization (not applied to this study) is more probably required to improve the accuracy and applicability of the nonintrusive measurement procedure. In addition, the opportunity to extend the usage of the ni-HFMNFP to CBC measurements should be studied. Furthermore, studies on the applicability of the probe with up-scaled dimensions for larger motors should be carried out. It is also suggested that in the ni-HFMNFP measurement that enables simultaneous measurement of EDM and CBC, a classification between the EDM and the CBC could be made with appropriate filters. For feasible assembly, it is suggested that a toroid structure could be constructed from two halves. It is also worth studying whether a single ferrite rod placed below the bearing could serve the purpose. This might be applicable when considering horizontally installed motors and assuming that discharges are likely to take place at the bottom of a bearing, where the lubricant film is thinnest as a result of gravitational pull.

It is proposed that the ni-HFMNFP could be a feasible device for online EDM bearing current measurements to be applied in series production motors in parallel with their normal operation. In order to verify this, it is necessary to study whether the bearing insulation system used in the measurements has a significant impact on the system behavior, for instance on the path that the HF EDM current tends to flow. The introduced NFP can be applied to research, maintenance, and product development. For these aims, the NFP should be installed into the part of an embedded system that serves as the pulse-magnitude analyzer (PMA). When the measurement concerns peak value acquisition, it is possible to apply signal processing, such as envelope detection and a signal peak detector, thereby lowering the ADC bandwidth requirements. It also enables a short-range wireless communication scheme such as ZigBee for data transmission.

6 Conclusion

The findings presented in this doctoral dissertation show that RF-signal-based methods can be used as an operating mode detector for the bearings of a VSI-driven LVSCIM. A nonintrusive measurement approach enabled by the use of the RF signal content originating from the bearing current phenomena, combined with the knowledge of the bearing behavior in certain operating parameters, is shown to provide a feasible tool to be applied in the future bearing current studies. However, in this context, the operating temperature for the bearing-current-related aging analysis is proposed to be a significant parameter, which cannot most probably be estimated accurately enough, and has therefore to be measured. Furthermore, a common problem in the studies presented in this doctoral dissertation is the limited number of individual bearing current events in each analysis. Hence, in general, the unknown deviation in the common behavior and possible exceptions make the results and the applicability of the proposed methods uncertain for the time being. Therefore, measurement systems are required that enable automatic data logging for thousands of bearing current events (and more) so that probabilistic and statistical methods can be applied to the accuracy and applicability analysis of the proposed nonintrusive bearing current measurement methods. Again, this target could be reached as a consequence of the further development of nonintrusive bearing current measurement systems. In addition, such development would direct the research towards measurements systems that are capable of operating online in field conditions for long periods of time without a requirement for maintenance. Along with the targeted improvements in the accuracy of the measurement methods, more detailed studies are needed to be able to classify the aging impacts of different bearing current types. Studies are required to enhance knowledge and clarify information related to the bearing current phenomena and the related aging charasteristics. For example, it is considered feasible to derive an aging impact equation for different bearing current types that covers information on both the energy and number of individual bearing current events. Once it is verified how the bearing currents and the aging impacts correlate with each other, it is possible to apply different measurement methods to maintenance and condition monitoring. Finally, all these studies can be based on the research work introduced and discussed in this doctoral dissertation.

Suggestions for future work

1. Based on the literature and the studies carried out in this doctoral dissertation, we may conclude that a nonintrusive measurement or approximation method for the bearing voltage waveform is required. Because continuous intrusive measurement of U_b is considered impractical, closer studies should be made on an approach for EDM discharge energy estimation by nonintrusive U'_b determination. The method proposed here is based on the knowledge that the U_b mirrors U_{com} with the ratio of BVR. Thus, U'_b could be determined by a simultaneous measurement (or an

approximation based on a verification measurement) of U_{com} and acquisition of the time difference Δt between the switching event and the moment of EDM. Further, a nonintrusive indication of the moment of EDM can be obtained by the RF-SBBCDM. Thus, by knowing BVR(T), $U_{com}(t)$, and Δt, the U'_b could be solved. Figure 6.1 illustrates the procedure by which U'_b can be obtained without a continuous intrusive measurement of U_b. In subplot A, a set of U_b waveforms are recorded by an intrusive measurement. For example, two EDM events are indicated by their U'_b values. In addition, the time differences of the EDM events to the switching event are denoted Δt_1 and Δt_2. In subplot B, the associated RF pulses for each EDM are measured by the RF-SBBCDM. Again, the Δt_1 and Δt_2 time differences are indicated, this time between the received RF pulses and the switching event. In addition, the U_{com} waveform of the switching event that has no associated EDM is added to illustrate the Δt_1 and Δt_2. Now, with the U_{com} waveforms shown in subplot C, U'_b can be estimated by multiplying the $U_{com}(\Delta t)$ value by the BVR. In the experimental measurement it is calculated that BVR is 0.038.
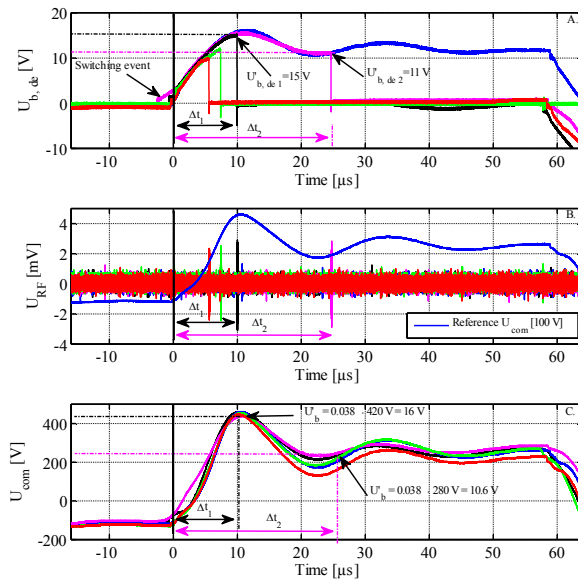

Fig. 6.1. Nonintrusive determination of U'_b by BVR and $U_{com}(\Delta t)$. The time difference Δt between the switching event and the EDM can be determined by the RF-SSBCDM. In each subplot, signals associated with the same switching event are indicated by the same color. Subplot A demonstrates the U_b waveforms of multiple switching events with two examples of Δt. Subplot B shows the U_{RF} waveforms of multiple switching events with two examples of Δt. Finally, subplot C depicts the U_{com} waveform of multiple switching events.

By the proposed measurement procedure, the energy dissipated in a bearing during an EDM discharge could be estimated, as discussed in section 1.1.12. Furthermore, slightly different approaches may be adopted depending on the required level of "nonintrusivity" of the measurement, at the cost of accuracy. For example, U_{com} can be either measured simultaneously or approximated based on a short verification measurement by which the BVR is likely to be obtained. It is proposed that the method could also be used for nonintrusive parameter acquisition in simulation-based bearing current estimation methods.

Owing to the bearing impedance behavior as a function of operating point, one aspect that also has to be considered is variation in the bearing voltage waveform when compared with the corresponding U_{com} waveform. Because of a lower bearing impedance, C_{rg} is discharged faster by an increased leakage current, thus having an effect on the BVR. Moreover, it is suggested that the presented approach brings the inverter-based condition monitoring and bearing current measurements closer to each other. Thus, it is proposed that the subject should be studied carefully before estimating the performance and applicability of the proposed approach. Therefore, several questions still remain open, and should be addressed in the future work.

2. The bearing impedance measurements indicate that the discharge impedance may not be fixed, and thus, it has an effect on the peak value of the bearing current pulse. An example of the measurements on the effect of the variation in $Z_{\mathrm{b,EDM}}$ on $\hat{I}_{\mathrm{b}}$ is shown in Fig. 6.2, where a discharge from the higher U'_{b} results in a lower $\hat{I}_{\mathrm{b}}$ than a discharge from a lower U'_{b}. From a nonintrusive measurement point of view, it is considered possible that Z_{EDM} could be approximated with the aid of a parameter such as the magnitude of the associated RF pulse. This is an issue to be investigated in the further studies.
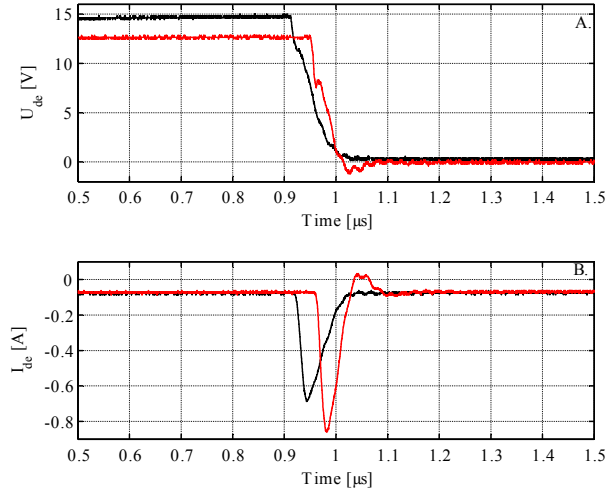
100

Fig. 6.2. Deviation in the magnitude of the EDM current pulse as a function of U'_b. U_b and I_b waveformd of same EDM are associated by the color. In subplot A the U_b waveforms and in subplot B the I_b waveforms of two EDM event with different Z_{EDM} are indicated.

3. The EZNEC could be applied for the magnetic field strength analysis according to which the induction voltage for the ni-HFMNFP could be estimated for motors of different dimensions. In order to make the ni-HFMNFP measurement probe a part of a complete measurement system, a low-cost instrumentation and data analysis concept has to be designed. Because a crucial parameter is the magnitude of the bearing current pulse, it should be possible to construct a peak-value-detector-based data acquisition system that can be connected to a central data logging device for example by applying short-range radio communication. This approach makes measurements applicable to various motors, which may well be the requirement in the industry. It is suggested that this should be basically a matter of engineering work.

References

Abu-Rub, H., Ahmed, S. M., Iqbal, A., Rahimian, M., and Toliyat, H. A. (2010), "Incipient bearing fault diagnostics for inverter fed induction motor drive using ANFIS," in *the XIX International Conference on Electrical Machines (ICEM)*, Rome, Italy.

Adabi, J., Zare, F., Ghosh, A., and Lorenz, R. D. (2010), "Calculations of capacitive couplings in induction generators to analyse shaft voltage," *IET Power Electronics*, Vol. 3, No. 3, 2010, pp. 379–390.

Adabi, J., Zare, F., Ledwich, G., Ghosh, A., and Lorenz, R. D. (2008), "Bearing damage analysis by calculation of capacitive coupling between inner and outer races of a ball bearing," in *the 13 th Power Electronics and Motion Control Conference (EPE-PEMC 2008)*, Poznan, Poland, pp. 903–907.

Ahola, J., Särkimäki, V., Muetze, A., and Tamminen, J. (2010), "Radio frequency based Detection of Electrical discharge machining Bearing currents," *IET Electric Power Applications*, Vol. 5, 2011, pp. 386–392.

Akagi, H. and Tamura, S. (2006), "A Passive EMI Filter for Eliminating Both Bearing Current and Ground Leakage Current From an Inverter-Driven Motor," *IEEE Transactions on Power Electronics*, Vol. 21, No. 5, 2006, pp. 1459–1469.

Alger, P. and Samson, H. (1924), "Shaft currents in electric machines," in *A.I.R.E. conference*, Philadelphia, PA, USA, pp. 235–245.

Balanis, C. A. (2005), *Antenna Theory – Analysis and Design* (3rd Edition), John Wiley & Sons., Online version available at: http://app.knovel.com/hotlink/toc/id:kpATADE001/antenna-theory-analysis.

Barclay, L. (2013), *Propagation of Radiowaves* (3rd Edition). Institution of Engineering and Technology, Online version available at:http://app.knovel.com/hotlink/toc/id:kpPRE00004/propagation-radiowaves.

Bell, S., Cookson, T. J., Cope, S. A., Epperly, R. A., Fischer, A., Schlegel, D. W., and Skibinski, G. L. (1998), "Experience with variable frequency drives and motor bearing reliability," in *Industry Applications Society 45th Annual Petroleum and Chemical Industry Conference*, Indianapolis, IN, USA, pp. 253–262.

Blake, L. V. and Long, M. W. (2009), *Antennas – Fundamentals, Design, Measurement* (3rd Edition), 1. Antennas (Electronics), SciTech Publishing, 2009.

Bonnett, A. H. (1993), "Cause and analysis of anti-friction bearing failures in A.C. induction motors," in *Conference Record of Pulp and Paper Industry Technical Conference*, Seattle, WA, USA, pp. 36–46.

Bonnett, A. H. (2000), "Root cause AC motor failure analysis with a focus on shaft failures," *IEEE Transactions on Industry Applications*, Vol. 36, No. 5, pp. 1435–1448.

Bonnett, A. H. (2010), "Root cause failure analysis for AC indiction motors in the petroleum and chemical industry," in *Record of Conference Papers of the Industry Applications Society 57th Annual Petroleum and Chemical Industry Conference (PCIC)*, San Antonio, TX, USA.

Burke, G. J. and Poggio, A. J. (1981), *Numerical electromagnetics code (NEC) – methods of moments, part II: program description – code*, Lawrence Livermore Laboratory.

Busse, D. F., Erdman, J. M., Kerkman, R. J., Schlegel, D. W., and Skibinski, G. L. (1997a), "Bearing currents and their relationship to PWM drives," *IEEE Transactions on Power Electronics*, Vol. 12, No. 2, pp. 243–252.

Busse, D. F., Erdman, J. M., Kerkman, R. J., Schlegel, D. W., and Skibinski, G. L. (1997b), "System electrical parameters and their effects on bearing currents," *IEEE Transactions on Industry Applications*, Vol. 33, No. 2, 1997, pp. 577–584.

Busse, D. F., Erdman, J. M., Kerkman, R. J., Schlegel, D. W., and Skibinski, G. L. (1997c), "The effects of PWM Voltage Source Inverters on the mechanical performance of rolling bearings," *IEEE Transactions on Industry Applications*, Vol. 33, No. 2, pp. 567–576.

Cacciato, M., Consoli, A., Scarcella, G., Scelba, G., Testa, A, (2009), "Modified Space-Vector-Modulation Technique for Common Mode Currents Reduction and Full Utilization of the DC Bus ," In the *Applied Power Electronics Conference and Exposition*, pp. 109–115.

Cacciato, M., Caro, S.D., Scarcella, G., Scelba, G., Testa, A., (2013), "Improved space-vector modulation technique for common mode currents reduction," *IET power electronics*, Vol. 6, No. 7, pp. 1248–1256.

Cetin, N.O. ; Hava, A.M. (2009), "Scalar PWM implementation methods for three-phase three-wire inverters," In the *International Conference on Electrical and Electronics Engineering*, 2009, pp. 447–451.

Chen, S., Lipo, T. A., and Novotny, D. W. (1996), "Circulating type motor bearing current in inverter drives, Industry Applications Conference," in the *Conference Record of the Thirty-First IAS Annual Meeting, IAS '96*, San Diego, CA, USA, Vol. 1, 1996, pp. 162–167.

CMI magnets (XCK material) (2014), Ferrite core material datasheet, available at http://www.cmi-ferrite.com/Materials/Datasheets/NiZn/XCK.pdf.

Costabile, G., De Vivo, B., Egiziano, L., Lamberti, P., and Tucci, V. (2007), "Performances of dielectric greases for rolling bearings employed in high power induction motors fed by PWM inverters," in the *Conference on Electrical Insulation and Dielectric Phenomena (CEIDP)*, Vancouver, Canada, pp. 45–48.

ETS Lindgren, (2002), antenna datasheet, available: http://www.ets-lindgren.com/manuals/3148.pdf, accessed 28. Aug. 2014.

ETS Lindgren, (2011), antenna datasheet, available:http://www.ets-lindgren.com/pdf/3110C.pdf, accessed 28.8.2014.

EZNEC (2014), "Antenna Software," available at www.eznec.com, accessed 17 March, 2014.

Frosini, L. and Bassi, E. (2010), "Stator Current and Motor Efficiency as Indicators for Different Types of Bearing Faults in Induction Motors," *IEEE Transactions on Industrial Electronics,* Vol. 57, No. 1, 2010, pp. 244–251.

Frosini, L., Bassi, E., and Gazzaniga, C., (2008), "Effect of the bearing faults on the efficiency of the induction motors," in the *34th Annual Conference of Industrial Electronics (IECON 2008)*, Orlando, FL, USA, pp. 1167–1172.

Guru, B. S. and Hiziroglu, H. R., (2001), *Electric Machinery and Transformers*, available at http://app.knovel.com.

Guttowski, S., Weber, S., Schinkel, M., John, W., and Reichl, H. (2006), "Troubleshooting and fixing of inverter driven induction motor bearing currents in existing plants of large size - an evaluation of possible mitigation techniques in practical applications," in the *Twenty-First Annual IEEE Applied Power Electronics Conference and Exposition*, Dallas, TX, USA.

Harish, A.R., Sachidananda, M., (2007), Antennas and Wave Propagation, available at http://app.knovel.com.

Hava, A.M. and Un, E. (2009), "Performance Analysis of Reduced Common-Mode Voltage PWM Methods and Comparison With Standard PWM Methods for Three-Phase Voltage-Source Inverters," *IEEE Transactions on Power Electronics*, Vol. 24, No. 1, pp. 241–252.

Herbert, W. (2011), "Rolling element bearing basics in large electric motors," in *Annual IEEE Conference Record of the Pulp and Paper Industry Technical Conference (PPIC)*, Nashville, TN, USA, pp. 189–195.

Hewson, C. R., Ray, W. F., and Davis, R. M. (2006), "Verification of Rokowski current transducer's ability to measure fast switching transients," In *Proceedings of the IEEE Applied Power Electronics Conference (APEC)*, Dallas, TX, USA.

Hyypio, D. B. (1997), "Effects of risetime and cable length on motor insulation degradation resulting from operation on PWM voltage source inverters," *IEEE International Electric Machine and Drives Conference, (IEMDC),* 1997.

Kriese, M., Wittek, E., Gattermann, S., Tischmacher, H., Poll G., and Ponick, B. (2010), "Prediction of motor bearing currents for converter operation," in the *XIX International Conference on Electrical Machines (ICEM)*, Rome, Italy.

Kriese, M., Wittek, E., Gattermann, S., Tischmacher, H., Poll, G., and Ponick, B. (2012), "Influence of bearing currents on the bearing lifetime for converter driven machines," in the *XXth International Conference on Electrical Machines (ICEM)*, Dublin, Ireland, pp. 1735–1739.

Li, B., Chow, M.-Y., Tipsuwan, Y., and Hung, J. C. (2000), "Neural-network-based motor rolling bearing fault diagnosis," *IEEE Transactions on Industrial Electronics*, Vol. 47, No. 5, 2000 , pp. 1060–1069.

Magdun, O. and Binder, A. (2009), "Calculation of roller and ball bearing capacitances and prediction of EDM currents," in the 35th *Annual Conference of IEEE on Industrial Electronics (IECON '09)*, Porto, Portugal, pp. 1051–1056.

Mercier, C.D. and Cooper, D.A. (1999), "Selection of power cables for PWM AC adjustable-speed drives," in *IEEE Annual Textile, Fiber and Film Industry Technical Conference*, San Diego, CA, USA.

Muetze, A. (2008), "On a New Type of Inverter-Induced Bearing Current in Large Drives with Oil-Lubricated Bearings," in *IEEE Industry Applications Society Annual Meeting (IAS '08)*, Edmonton, Canada.

Muetze, A. and Binder, A. (1997), "Don't lose your bearings," *IEEE Industry Applications Magazine*, Vol. 12, No. 4, 2006, pp. 22–31.

Muetze, A. and Binder, A., (2003), "Experimental evaluation of mitigation techniques for bearing currents in inverter-supplied drive-systems - investigations on induction motors up to 500 kW," in *IEEE International Electric Machines and Drives Conference (IEMDC'03)*, Madison, WI, USA, Vol. 3, 2003, pp. 1859–1865.

Muetze, A. and Binder, A. (2007a), "Practical Rules for Assessment of Inverter-Induced Bearing Currents in Inverter-Fed AC Motors up to 500 kW," *IEEE Transactions on Industrial Electronics*, Vol. 54, No. 3, 2007, pp. 1614–1622.

Muetze A., and Binder, A. (2007b), "Calculation of Motor Capacitances for Prediction of the Voltage Across the Bearings in Machines of Inverter-Based Drive Systems," *IEEE Transactions on Industry Applications*, Vol. 43, No. 3, 2007, pp. 665–672.

Muetze, A., and Binder, A. (2007c), "Calculation of Circulating Bearing Currents in Machines of Inverter-Based Drive Systems," *IEEE Transactions on Industrial Electronics,* Vol. 54, No. 2, 2007, pp. 932–938.

Muetze, A., Binder, A., Vogel, H., and Hering, J. (2004), "Experimental evaluation of the endangerment of ball bearing due to inverter-induced bearing currents," In *Proceedings of IEEE Industry Applications Conference*, Seattle, WA, USA,Vol. 3, pp. 1989–1995.

Muetze, A., Binder, A., Vogel, H., and Hering, J. (2006), "What can bearings bear?" *IEEE Industry Applications Magazine*, Vol. 12, No. 6, 2006, pp. 57–64.

Muetze, A., Tamminen, J., and Ahola, J. (2010), "Influence of motor operating parameters on discharge bearing current activity," in *IEEE Energy Conversion Congress and Exposition (ECCE)*, Atlanta, GA, USA, pp. 2739–2746.

Nachi, (2003), technocal datasheet, SRL multitemp grease, available: http://www.kyodoyushi-europe.com/publications/Multemp%20SRL%20Leaflet.pdf, accessed: 28.8.2014

Niskanen, V. (2010), "Wireless torque measurement system," Master's thesis, Lappeenranta University of Technology.

Niskanen, V. and Ahola, J., (2011), "Implementing clamp on wireless torque measurement system for rotating shaft applications (UI)," in *Proceedings of the 14th European Conference on Power Electronics and Applications (EPE 2011)*, Birmingham, UK.

Niskanen, V., Lehtinen, P., and Ahola, J. (2013), "Verification of the applicability of an RF-signal-based detection method for partial discharges on inverter-fed random wound stator windings in a low-voltage induction motor," in the *15th European Conference onPower Electronics and Applications (EPE)*, Lille, France.

Perrin, M. C., (1996), "Large Induction motor anti-friction bearing selection," *IEEE Industry Applications Magazine*, Vol. 2, No. 2, 1996, pp. 16–20.

Rao, B. K. N., Kaliszer, H., and Rowe, G. W. (1981), *"*An on-line technique to monitor running-in of plain grease-lubricated bearings," *Wear. An International Journal on the Science and Technology of Friction, Lubrication and Wear*, Vol. 73, Iss. 1, pp. 157–162.

Ray, W. F and Davis, R. M. (1999), "High Frequency Improvements in Wide Bandwidth Rogowski Current Transducers," In *Proceedings of European Power Electronics and Applications (EPE)*, Lausanne, Switzerland.

Saunders, L. A., Skibinski, G. L., Evon, S. T., and Kempkes, D. L. (1996), "Riding the reflected wave-IGBT drive technology demands new motor and cable considerations," in *Record of the Conference Papers of the 43rd Annual Petroleum and Chemical Industry Conference of The Institute of Electrical and Electronics Engineers Incorporated Industry Applications Society*, Philadelphia, PA, USA, pp. 75–84.

Schweitzer, G. and Maslen, E.H. (eds.) (2009), *Magnetic Bearings, Theory, Design, and Application to Rotating Machinery*, Berlin, Heidelberg, Springer.

Shah, A. (2011), "Paradigm shift in proper selection criteria of VFD cable for variable frequency drives," in the *53rd Cement Industry Technical Conference (IEEE-IAS/PCA)*, St. Louis, MO, USA.

Shancheng, X. and Wu, Z. (2006), "Characteristic Research of Bearing Currents in Inverter-Motor Drive Systems," in the *5th CES/IEEE International Power Electronics and Motion Control Conference (IPEMC)*, Shanghai, China, Vol. 2, 2006.

Stack, J. R., Habetler, T. G., and Harley, R. G. (2003), "Effects of machine speed on the development and detection of rolling element bearing faults," *IEEE Power Electronics Letters*, Vol. 1, No. 1, 2003, pp. 19–21.

SNR, (2010), "Technical datasheet, LUB universal +", Available: http://www.ntn-snr.com/services/fr/en-en/file.cfm/TECHNICAL_DATA_SHEET_LUB_UNIVERSAL_+_GB.pdf?contentID=6705, accessed 28.Aug. 2014.

Särkimäki, V. (2009), *Radio Frequency measurement method for detecting bearing currents in induction motors*, Doctoral dissertation, Acta Universitatis Lappeenrantaensis 341, Lappeenranta University of Technology, Lappeenranta, Finland.

Tavner, P. J. (2008), "Review of condition monitoring of rotating electrical machines," *IET Electric Power Applications*, Vol. 2, No. 4, 2008, pp. 215–247.

Tavner, P., Li R., Penman, J., and Sedding, H. (2008), *Condition Monitoring of Rotating Electrical Machines*, 2nd Edition, Institution of Engineering and Technology.

Tischmacher, H. and Gattermann, S. (2010), "Bearing currents in converter operation," in the *XIX International Conference on Electrical Machines (ICEM)*, Rome, Italy.

Tischmacher, H. and Gattermann, S. (2012a), "Investigations on bearing currents in converter-fed electrical motors," in the *XXth International Conference on Electrical Machines (ICEM)*, Dublin, Ireland, pp. 1764–1770.

Tischmacher, H. and Gattermann, S. (2012b), "Multiple signature analysis for the detection of bearing currents and the assessment of the resulting bearing wear," in *International Symposium on Power Electronics, Electrical Drives, Automation and Motion (SPEEDAM)*, Sorrento, Italy, pp. 1354–1359.

Tischmacher, H., Gattermann, S., Kriese, M., and Wittek, E. (2010), "Bearing wear caused by converter-induced bearing currents," in the *36th Annual Conference on IEEE Industrial Electronics Society (IECON)*, Glendale, AZ, USA, pp. 784–791.

Wei, Z., Habetler, T. G., and Harley, R. G. (2008), "Bearing Fault Detection Via Stator Current Noise Cancellation and Statistical Control," *IEEE Transactions on Industrial Electronics*, Vol. 55, No 12, pp. 4260–4269.

Wu, B. (2006), *High-power converters, and AC drives*, Hoboken, John Wiley & Sons, Inc.

Yazici, B. and Kliman, G.B. (1999), "An adaptive statistical time-frequency method for detection of broken bars and bearing faults in motors using stator current," *IEEE Transactions on Industry Applications*, Vol. 35, No. 2, 1999, pp. 442–452.

Zare, F. (2010), "Practical approach to model electric motors for electromagnetic interference and shaft voltage analysis," *IET Electric Power Applications*, Vol. 4, No. 9, 2010, pp. 727–738.

Zika, T., Gebeshuber, I. C., Buschbeck, F., Preisinger, G., and Gröschl, M. (2009), "Surface analysis on rolling bearings after exposure to defined electrical stress," in *Proceedings of the Institution of Mechanical Engineers*, *Part J: Journal of Engineering Tribology*, Vol. 223, no. 5 pp. 787–797.

Appendix A: Bearing impedance measurement setups

Table A1. Measurement equipment for the $P_n = 15$ kW motor test setup.

Device	Model
VSI	ABB ACS400
Motor	Invensys, $P_n = 15$ kW, 4-pole, delta connected, LVSCIM
Bearings*	SNR 6309-C3, mineral-oil, lithium soap-based lubricant (SNR, 2010)
Oscilloscope	R&S RTO 1014 (10 GS/s–1 GHz)
Active current probe	R&S ZC-20 (DC–100 MHz)
Differential voltage probe	R&S ZT-01 (DC–100 MHz)
Signal generator**	Hameg HM8131-2 (DC–15 MHz, U_{pp}, max 20 V
RF receiver antenna	ETS-93148 log. periodic antenna (200 MHz–2 GHz)
RF BPF	Mini-Circuits BHP100+ and BLP750+ (90–400 MHz)
Temperature measurement***	Handheld AZ8868 infrared thermometer

*Both the bearings are insulated by polyethen sleeves that are installed between the bearing seats and the bearings in the end plates of the motor. In addition, to enable intrusive measurement of the bearing current magnitude, the outer raceway is shorted to the DE plate by an electric cord. **A signal generator is used to generate an external single-tone signal over the NDE bearing. ***The temperature is measured between the shaft and the DE plate of the motor.

Table A2. Measurement equipment for the $P_n = 75$ kW motor test setup.

Device	Model
VSI	ABB ACS550
Motor	ABB, $P_n = 75$ kW, 4-pole, delta connected, LVSCIM
Bearings*	SNR 6316-C3, mineral oil, lithium soap-based lubricant (SNR, 2010)
Oscilloscope	R&S RTO 1014 (10 GS/s–1 GHz)
Active current probe	R&S ZC-20 (DC–100 MHz)
Differential voltage probe	R&S ZT-01 (DC–100 MHz)
Signal generator**	Hameg HM8131-2 (DC–15 MHz, U_{pp}, max 20 V
RF receiver antenna	ETS-93148 log. periodic antenna (200 MHz–2 GHz)
RF BPF	Mini-Circuits BHP100+ and BLP750+ (90–400 MHz)
Temperature measurement***	handheld AZ8868 infrared thermometer

*Both the bearings are insulated by polyethen sleeves that are installed between the bearing seats and the bearings in the end plates of the motor. In addition, to enable the intrusive measurement of the bearing current magnitude, the outer raceway is shorted to the DE plate by an electric cord. **A signal generator is used to generate an external single-tone signal over the NDE bearing. ***The temperature is measured between the shaft and the DE plate of the motor.

Matlab script of the FFT and impedance calculation

```
% Parameters for FFT calculation
Fs = 1e7; %determined according to decimation factor
fsig = 300e3; %external input signal frequency
N = 32; %window size
k = 2;

Ude_fft = zeros(size(Ude_dec));
Ck = zeros(N);

% sample window defined earlier is slided over measurement data
for (i=1:size(Ude_dec)-N),
    Ck = fft(Ude_dec(i:i+N),N)./N;
    Ude_fft(i)=2*Ck(k);
end

Ide_fft = zeros(size(Ide_dec));
Ck = zeros(N);
for (i=1:size(Ide_dec)-N),
    Ck = fft(Ide_dec(i:i+N),N)./N;
    Ide_fft(i)=2*Ck(k);
end

Zb = Ude_fft./Ide_fft; %Impedance calculation
% cells for Cb are determined by iteration cycle according to which piece of signals at -90deg phase shift is selected.
Cb = 1/(mean(abs(Zb(850:1100)))*2*pi*fsig)
Rmin = min(abs(Zb))
```

TrA Matlab script

```
%%interference reduction filtering
Fs = Fsample;  % Sampling Frequency
Fstop1 = 5e4;        % First Stopband Frequency
Fpass1 = 1e5;        % First Passband Frequency
Fpass2 = 7.5e5;       % Second Passband Frequency
Fstop2 = 8e5;       % Second Stopband Frequency
Astop1 = 60;         % First Stopband Attenuation (dB)
Apass  = 1;          % Passband Ripple (dB)
Astop2 = 80;         % Second Stopband Attenuation (dB)
match  = 'passband';  % Band to match exactly
% Construct an FDESIGN object and call its CHEBY1 method.
h  = fdesign.bandpass(Fstop1, Fpass1, Fpass2, Fstop2, Astop1, Apass, ...
              Astop2, Fs);
Hd2 = design(h, 'cheby1', 'MatchExactly', match);

Ude_DC_filtered1=filter(Hd2,Ude);

%Envelope detection
Ude_curtain1=abs(Ude_DC_filtered1); %absolute value. ie. two-pulse-rectifying
U_ref_high=mean(Ude_curtain1(118000:119900))% determines the highest level of envelope detected signal
U_ref_low=mean(Ude_curtain1(120000:120600))% determines the lowest level of envelope detected signal

Fs = Fsample;  % Sampling Frequency
Fpass = 50*1e3;      % Passband Frequency
Fstop = 200*1e3;     % Stopband Frequency
Apass = 1;        % Passband Ripple (dB)
Astop = 20;         % Stopband Attenuation (dB)
match = 'stopband';  % Band to match exactly
% Construct an FDESIGN object and call its BUTTER method.
h  = fdesign.lowpass(Fpass, Fstop, Apass, Astop, Fs);
Hd = design(h, 'butter', 'MatchExactly', match);

Ude_LOWPASS_Filtered1 = filter(Hd, Ude_curtain1);
```

```
Uth1H=U_ref_high*0.75;%Capacitive level threshold margin
Uth1L=U_ref_low+U_ref_high-U_ref_high*0.75;%Resistive level threshold margin
Ref=(max(Ude_LOWPASS_Filtered1))*0.50;
Uth11H=ones(size(Time1))*Uth1H;
Uth11L=ones(size(Time1))*Uth1L;
Ude_Pulse_Filtered1(n)=zeros;
% ----Hystereesi filter.
if Ude_LOWPASS_Filtered1(1)> Ref
   UTHL_flag=1;
   LTHL_flag=0;
else
   UTHL_flag=0;
   LTHL_flag=1;
end
for d=1:1:n
   signal_level=Ude_LOWPASS_Filtered1(d);
   if UTHL_flag==1 %when in capacitive mode
      if signal_level < Uth1L %if signal less than lower threshold level
      Ude_Pulse_Filtered1(d)=0;
      UTHL_flag=0;
      LTHL_flag=1;
      else
      Ude_Pulse_Filtered1(d)=Upp;
      end
   elseif LTHL_flag==1 % when in resistive mode
      if signal_level > Uth1H %if signal more than upper threshold level
      Ude_Pulse_Filtered1(d)=Upp;
      UTHL_flag=1;
      LTHL_flag=0;
      else
      Ude_Pulse_Filtered1(d)=0;
      end
   end
end
Transient_count1=(sum(abs(diff(sign(Ude_Pulse_Filtered1)))))*0.5;
Time_c1=0;
Time_r1=0;
for d=1:1:n
   if Ude_Pulse_Filtered1(d) > Ref
   Time_c1=Time_c1+Ts;
   elseif Ude_Pulse_Filtered1(d) <= Ref
   Time_r1=Time_r1+Ts;
   end
end
Total_time1= n*Ts;
Mode_C_ratio1= Time_c1/Total_time1;
Mode_R_ratio1= Time_r1/Total_time1;
Total_time_diff1= Total_time1-(Time_c1+Time_r1);
 TimeR1=0;
 TimeC=0;
 TimeF=0;
for d=1:1:n
   signal_level=Ude_LOWPASS_Filtered1(d);
      if signal_level < Uth1L %if signal level is lower then threshold level
      TimeR1=TimeR1+Ts;
      elseif signal_level > Uth1H %if signal is higher than upper thresh
      TimeC=TimeC+Ts;
      else
      TimeF=TimeF+Ts;
      end
end%
Time_Sum=TimeC+TimeR1+TimeF;
TimePU(1)=TimeC/(Total_time1);
TimePU(2)=TimeR1/(Total_time1);
TimePU(3)=TimeF/(Total_time1);
```

Appendix B: Measurement setup for the RF-SBBCDM for CBC and RGC detection

Table B1. Equipment commonly applied in RF-SBBCDM for CBC and RGC detection.

Device	Model
RF receiver antenna	ETS-93148 log. periodic antenna (200 MHz–2 GHz)
RF BPF	Mini-Circuits BHP100+ and BLP750+ (90–400 MHz)
Temperature measurement*	Handheld AZ8868 infrared thermometer
Passive current probe**	R&S EZ-17 (DC–100 MHz)

For both motors (P_n = 15 kW and P_n = 75 kW), both the bearings are insulated by polyethen sleeves that are installed between the bearing seats and the bearings in the end plates of the motor. In addition, to enable the intrusive measurement of the bearing current magnitudes, the outer raceways of both bearings are shorted to the end plates by an electric cord. *The temperature is measured between the shaft and the DE plate of the motor. **The HF CM current measurement.

Table B2. P_n = 15 kW motor setup.

Device	Model
VSI	ABB ACS400
Motor	Invensys, P_n = 15kW, 4-pole, delta connected, LVSCIM
Bearings*	SNR 6309-C3, mineral-oil-based lubricant (SNR, 2010)
Oscilloscope	Textronix TDS7140 (2.5 GS/s–1 GHz)
Active current probe	Textronix TCP202 (DC–50 MHz)
Differential voltage probe	Tektronix P5210 (DC–100 MHz)

In the cases where more than four measurement channels were needed, an additional oscilloscope R&S RTO 1014 was triggered in series so that an R&S trigger output signal was connected to the Tektronix TDS7104 external trigger input port.

Fig. B1. P_n = 15 kW motor laboratory measurement setup placed on a wooden platform. The antenna is outside the photograph.

Table B3. P_n = 75 kW motor setup.

Device	Model
VSI	ABB ACS550
Motor	ABB, P_n = 75 kW, 4-pole, delta connected, LVSCIM
Bearings*	SNR 6316-C3, mineral-oil, lithium soap-based lubricant (SNR, 2010)
Oscilloscope	R&S RTO 1014 (10 GS/s–1 GHz)
Active current probe	R&S ZC-20 (DC–100 MHz)
Differential voltage probe	R&S ZT-01 (DC–100 MHz)

Measurements requiring up to four channels were executed by an R&S RTO 1014 oscilloscope. An additional oscilloscope Tektronix TDS7104 was triggered in series so that an R&S RTO 1014 trigger output signal was connected to the external trigger input port of Tektronix TDS7104. A photograph of the measurement system is shown in Fig. B2. In addition, the P_n = 15 kW motor is covered by a blanket to accelerate the warming of the motor.

Fig. B2. P_n = 75 kW motor laboratory setup, where the motor is assembled on a motor test platform. It is pointed out that unlike the setup for the P_n = 15 kW motor, the P_n = 75 kW motor is also grounded through the platform.

Appendix C: Motor antenna simulation model

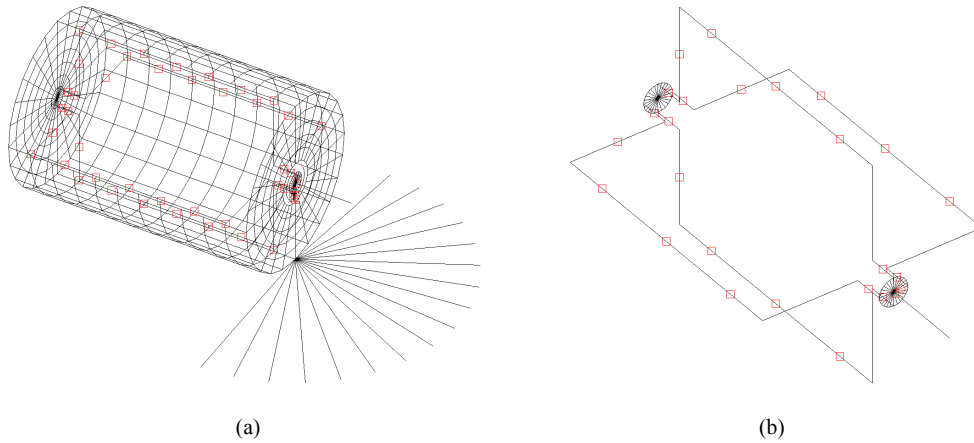(a)   (b)

Fig. C1. EZNEC model of the 3D antenna behavior of the LVSCIM that can be varied in different sizes of motors by scaling the dimensions and values of the lumped elements. The machine body and the ground plane below the DE shaft (Fig. C1a) and the rotor stucture (Fig. C1b) are modeled as wired structures. An exception is the DE motor shaft, which appears as an individual wire, but in the simulator it is dimensioned as a cylindrical rod, with the diameter of the shaft. In both subplots, the red squares represent additional loads such as resistances and capacitances. In the second subplot, all loads represent distributed additional resistances in the rotor circuit.

(a)   (b)

Fig. C2. Feed point of the motor with a 10 Ω surge resistor placed parallel to the feed point connection screws. In Fig. C2a, the shaft length is 12 cm; in Fig. C2b, the extended shaft length is 41 cm.
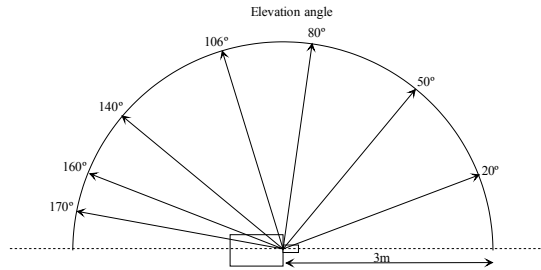
Fig. C3. Elevation angles used in the signal strength verification in the theoretical simulations and the experimental measurements.
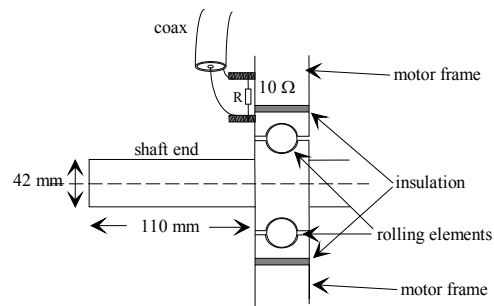

Fig. C4. Feedpoint structure in the verification measurements of the antenna radiation pattern. Since the motor is standing still during the measurements, the discharge impedance $Z_{b, EDM}$ through the bearing is imitated by a resistor of 10 Ω. This is done in order not to alter the test conditions too far from the actual EDM conditions.
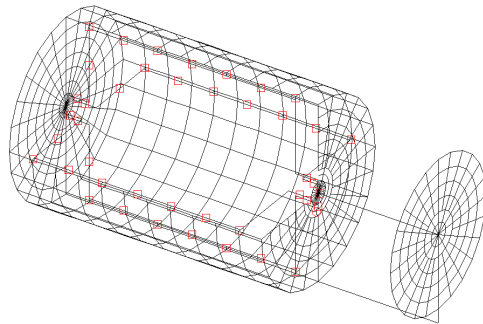

Fig. C5. Motor antenna simulation model for a system with a load machine and a galvanic shaft coupling. One quarter of the frame is removed in order to give a better sight of the overall structure. The rotor circuit is similar to Fig. C1.

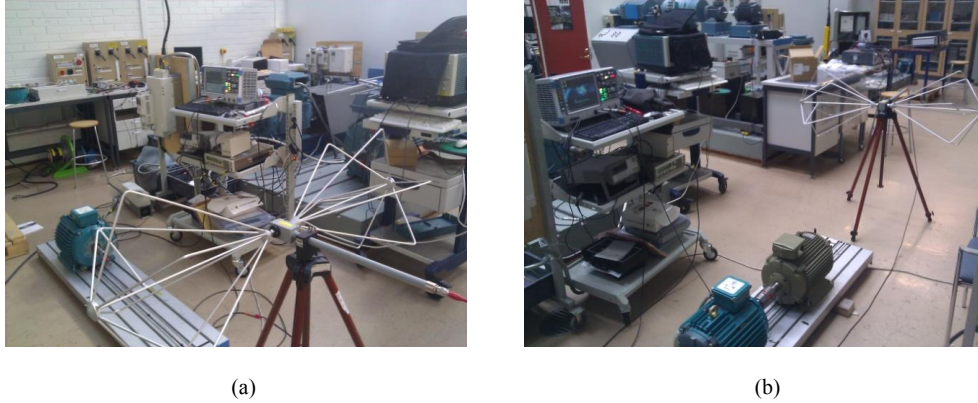(a)   (b)

Fig. C6a. Directivity measurement setup for the motor without a load.
Fig. C6b. Directivity measurement setup for motor with a load machine attached with an insulated shaft coupler.

Measurement setup for the radiation pattern verification

Table C1. Measurement equipment for the test setup.

Device	Model
Motor	Invensys, P_n = 15 kW, 4-pole, LVSCIM
Bearings*	SNR 6309-C3, mineral oil, lithium soap-based lubricant (SNR, 2010)
Network analyzer**	Agilent 4395A
S-parameter device**	Agilent 87511A
RF receiver antenna	ETS-Lindgren, dipole, 3110C (30–300 MHz)

*Both the bearings are insulated by polyethen sleeves that are installed between the bearing seats and the bearings in the end plates of the motor. **An Agilent 4395A network analyzer with an Agilent 87511A S parameter test device is used as a signal source and receiver. The RF power is supplied to the motor antenna over the DE bearing insulation. The frequency for the feed signal ranges from 30 MHz to 350 MHz. The supply power of 15 mW is fed through a 0.9 m, 50 Ω coaxial cable into the feed point of the motor antenna. It is pointed out that 15 mW is the maximum output power of the signal source and is chosen to ensure the best possible SNR.

Table C2. Equipment applied to the VHF oscillation analysis.

Device	Model
Motor	Invensys, P_n = 15 kW, 4-pole, LVSCIM
VSI	ABB-ACS400
Bearings*	SNR 6309-C3, mineral oil, lithium soap-based lubricant (SNR, 2010)
Oscilloscope	R&S RTO 1014 (10 GS/s–1 GHz)
RF BPF	Mini-Circuits BHP100+ and BLP750+ (90–400 MHz)
Passive current probe	R&S EZ-17 (DC–200 MHz) MOD.2
Passive voltage probe	ZP-RT10 (DC–500 MHz)
RF receiver antenna	ETS-Lindgren, dipole, 3110C (30–300 MHz)

Both of the bearings are insulated by polyethen sleeves that are installed between the bearing seats and the bearings in the end plates of the motor. In addition, to enable the intrusive measurement of the bearing current magnitudes, the outer raceway of the DE bearing is shorted to the DE end plate by an electric cord.

Appendix D: Measurement setup for the NFP verification

Table D1. Measurement equipment.

Device	Model
VSI	ABB ACS400
Motor	Invensys, P_n = 15 kW, 4-pole, delta connected, LVSCIM
Bearings*	Nachi 6309-C3, synthetic, lithium soap-based, Multemp SRL grease (Nachi, 2003)
Oscilloscope	R&S RTO 1014 (10 GS/s–1 GHz)
Active current probe	R&S ZC-20 (DC–100 MHz)
Differential voltage probe	R&S ZT-01 (DC–100 MHz)
Passive voltage probe	RT-ZP10 (DC–500 MHz)
Impedance analyzer	HP4194A
Signal generator	Agilent 33250A signal generator (DC–80MHz)

*Both the bearings are insulated by polyethen sleeves that are installed between the bearing seats and the bearings in the end plates of the motor. In addition, to enable the intrusive measurement of the bearing current magnitude, the outer raceway is shorted to the DE plate by an electric cord.
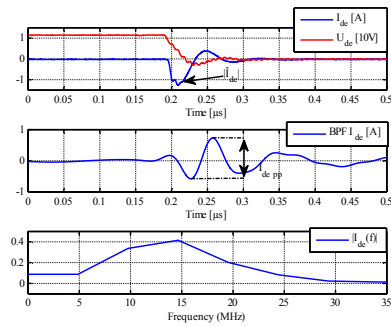

Fig. D1. Signal waveforms of the EDM in the topmost subplot. The waveform of the BPF I_{de} in the second subplot, and the FFT analysis of the BPF-filtered I_{de} in the bottom subplot.

Fig. D2. Ni-HFMNFP assembled on the DE plate in the laboratory measurement setup.
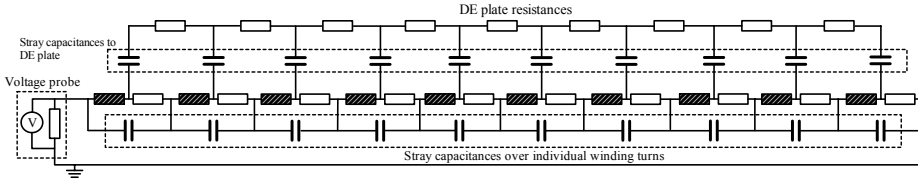
Fig. D3. Equivalent circuit of the ni-HFMNFP in its assembly position on the DE plate with the stray capacitances involved in the system.

Uncertainty

The uncertainty of the ni-HFMNFP measurement is estimated by a worst-case analysis, where it is assumed that $|\Delta I_{de}|$ and $|\Delta U_{ni\text{-}HFMNFP}|$ are independent of each other. Hence, the outmost point of the uncertainty area is studied by comparing the measurement data points with the first-order curve fit, which is obtained with MATLAB®. As illustrated in Fig. D4, $|\Delta U_{ni\text{-}HFMNFP}|$ is determined by the following procedure:

1. Determination of the location of a data point in the curve fit $U_{ni\text{-}HFMNFP} = k \cdot I_{de,md}$, if $U_{ni\text{-}HFMNFP} > U_{ni\text{-}HFMNFP,md}$ below, $U_{ni\text{-}HFMNFP} < U_{ni\text{-}HFMNFP,md}$ above.
2. Compensation of the intrusive current measurement uncertainty: below $I_{de} = I_{de,md} - |\Delta I_{de}|$ and if above the curve fit $I_{de} = I_{de,md} + |\Delta I_{de}|$
3. Substitution of I_{de} obtained in item 2 into the first-order curve fit $U_{ni\text{-}HFMNFP} = k \cdot I_{de}$
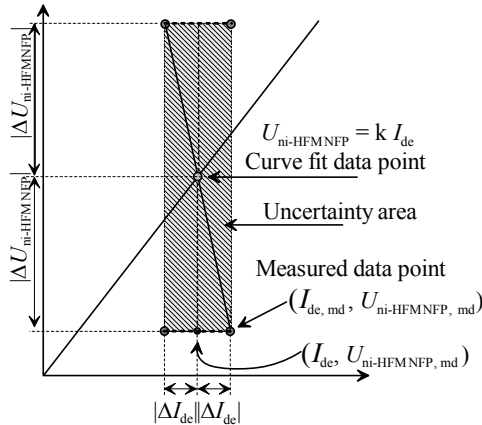4. Determination of the $|\Delta U_{ni\text{-}HFMNFP}| = |\Delta U_{ni\text{-}HFMNFP} - U_{ni\text{-}HFMNFP,md}|$

Fig. D4. Uncertainty estimation of $\left|\Delta U_{ni\text{-}HFMNFP,pp}\right|$.

Matlab script for EDM pulse processing

```
%-------------- Filter----------------------
Fstop1 = 3e6;        % First Stopband Frequency
Fpass1 = 5e6;        % First Passband Frequency
Fpass2 = 2.5e7;      % Second Passband Frequency
Fstop2 = 3e7;        % Second Stopband Frequency
Astop1 = 40;         % First Stopband Attenuation (dB)
Apass  = 1;          % Passband Ripple (dB)
Astop2 = 40;         % Second Stopband Attenuation (dB)
match  = 'stopband'; % Band to match exactly
% Construct an FDESIGN object and call its CHEBY1 method.
```

```matlab
h  = fdesign.bandpass(Fstop1, Fpass1, Fpass2, Fstop2, Astop1, Apass, ...
                Astop2, Fs);
Hd = design(h, 'cheby1', 'MatchExactly', match);
%           Uncertainty Analysis
K=1;
offset=-0.061; %uncertainty component caused by Ide measurement; quantization uncert+ sensitivity.+ probe uncert. Zero
error.%fixed uncertainties of current measurement:
Zero_uncertainty=0.01; %+-10mA %oscilloscope
Quantization_uncertainty=0.0781;% 2V/div * 10div 20V/2^8=
for i=1:1:N_EDM
Ide_measurement_uncertainty(i)=Zero_uncertainty+Zero_uncertainty+0.02*Ide_pp_array1(i);
Ide_measurement_uncertainty_abs(i)=Zero_uncertainty+Zero_uncertainty+0.02*Ide_abs_array(i);
end
for i=1:1:N_EDM
   Yref=Ide_pp_array1(i)-0.061;
   Yref_abs=1.24*Ide_abs_array(i)-0.224;
   Yreal=NFP_pp_array1(i);
   Yreal_abs=NFP_pp_array1(i)
   if Yref>Yreal%Smaller value compared to curve fit
      X_corrected=Ide_pp_array1(i)-Ide_measurement_uncertainty(i);
   elseif Yref<Yreal% Bigger value compared to curve fit
      X_corrected=Ide_pp_array1(i)+Ide_measurement_uncertainty(i);
   else
   end
    if Yref_abs>Yreal_abs%Smaller value compared to curve fit
      X_corrected_abs=Ide_abs_array(i)-Ide_measurement_uncertainty_abs(i);
   elseif Yref_abs<Yreal_abs% Bigger value compared to curve fit
      X_corrected_abs=Ide_abs_array(i)+Ide_measurement_uncertainty_abs(i);
   else
   end
Uncertainty_NFP(i)=abs((K*X_corrected-0.061)-abs(NFP_pp_array1(i)));
Uncertainty_NFP_abs(i)=abs((1.24*X_corrected_abs-0.224)-abs(NFP_pp_array1(i)));
end
%Y=1.24*X-0.224 Ide_p vs NPF_pp
The_biggest_uncertainty=max(Uncertainty_NFP)
The_biggest_uncertainty_abs=max(Uncertainty_NFP_abs)
for i=1:1:N_EDM
relative_uncertainty(i)=Uncertainty_NFP(i)/NFP_pp_array1(i);
relative_uncertainty_abs(i)=Uncertainty_NFP_abs(i)/NFP_pp_array1(i);
end
The_biggest_relative_uncertainty=max(relative_uncertainty)
The_biggest_relative_uncertainty_abs=max(relative_uncertainty_abs)
```

ACTA UNIVERSITATIS LAPPEENRANTAENSIS

582. SAUNILA, MINNA. Performance management through innovation capability in SMEs. 2014. Diss.

583. LANA, ANDREY. LVDC power distribution system: computational modelling. 2014. Diss.

584. PEKKARINEN, JOONAS. Laser cladding with scanning optics. 2014. Diss.

585. PELTOMAA, JYRKI. The early activities of front end of innovation in OEM companies using a new FEI platform as a framework for renewal. 2014. Diss.

586. ROZHANSKY, IGOR. Resonant tunneling effects in semiconductor heterostructures. 2014. Diss.

587. PHAM, THUY DUONG. Ultrasonic and electrokinetic remediation of low permeability soil contaminated with persistent organic pollutants. 2014. Diss.

588. HOKKANEN, SANNA. Modified nano- and microcellulose based adsorption materials in water treatment. 2014. Diss.

589. HINKKANEN, JUHA. Cooperative strategy in emerging markets – analysis of interfirm R&D cooperation and performance in Russian manufacturing companies. 2014. Diss.

590. RUSKOVAARA, ELENA. Entrepreneurship education in basic and upper secondary education – measurement and empirical evidence. 2014. Diss.

591. IKÄHEIMONEN, TUULI. The board of directors as a part of family business governance – multilevel participation and board development. 2014. Diss.

592. HAJIALI, ZUNED. Computational modeling of stented coronary arteries. 2014. Diss.

593. UUSITALO, VILLE. Potential for greenhouse gas emission reductions by using biomethane as road transportation fuel. 2014. Diss.

594. HAVUKAINEN, JOUNI. Biogas production in regional biodegradable waste treatment – possibilities for improving energy performance and reducing GHG emissions. 2014. Diss.

595. HEIKKINEN, JANNE. Vibrations in rotating machinery arising from minor imperfections in component geometries. 2014. Diss.

596. GHALAMCHI, BEHNAM. Dynamic analysis model of spherical roller bearings with defects. 2014. Diss.

597. POLIKARPOVA, MARIIA. Liquid cooling solutions for rotating permanent magnet synchronous machines. 2014. Diss.

598. CHAUDHARI, ASHVINKUMAR. Large-eddy simulation of wind flows over complex terrains for wind energy applications. 2014. Diss.

599. PURHONEN, MIKKO. Minimizing circulating current in parallel-connected photovoltaic inverters. 2014. Diss.

600. SAUKKONEN, ESA. Effects of the partial removal of wood hemicelluloses on the properties of kraft pulp. 2014. Diss.

601. GUDARZI, DAVOOD. Catalytic direct synthesis of hydrogen peroxide in a novel microstructured reactor. 2014. Diss.

602. VALKEAPAA, ANTTI. Development of finite elements for analysis of biomechanical structures using flexible multibody formulations. 2014. Diss.

603. SSEBUGERE, PATRICK. Persistent organic pollutants in sediments and fish from Lake Victoria, East Africa. 2014. Diss.

604. STOKLASA, JAN. Linguistic models for decision support. 2014. Diss.

605. VEPSÄLÄINEN, ARI. Heterogenous mass transfer in fluidized beds by computational fluid dynamics. 2014. Diss.

606. JUVONEN, PASI. Learning information technology business in a changing industry landscape. The case of introducing team entreneurship in renewing bachelor education in information technology in a university of applied sciences. 2014. Diss.

607. MÄKIMATTILA, MARTTI. Organizing for systemic innovations – research on knowledge, interaction and organizational interdependencies. 2014. Diss.

608. HÄMÄLÄINEN, KIMMO. Improving the usability of extruded wood-plastic composites by using modification technology. 2014. Diss.

609. PIRTTILÄ, MIIA. The cycle times of working capital: financial value chain analysis method. 2014. Diss.

610. SUIKKANEN, HEIKKI. Application and development of numerical methods for the modelling of innovative gas cooled fission reactors. 2014. Diss.

611. LI, MING. Stiffness based trajectory planning and feedforward based vibration suppression control of parallel robot machines. 2014. Diss.

612. KOKKONEN, KIRSI. From entrepreneurial opportunities to successful business networks – evidence from bioenergy. 2014. Diss.

613. MAIJANEN-KYLÄHEIKO, PÄIVI. Pursuit of change versus organizational inertia: a study on strategic renewal in the Finnish broadcasting company. 2014. Diss.

614. MBALAWATA, ISAMBI SAILON. Adaptive Markov chain Monte Carlo and Bayesian filtering for state space models. 2014. Diss.

615. UUSITALO, ANTTI. Working fluid selection and design of small-scale waste heat recovery systems based on organic rankine cycles. 2014. Diss.

616. METSO, SARI. A multimethod examination of contributors to successful on-the-job learning of vocational students. 2014. Diss.

617. SIITONEN, JANI. Advanced analysis and design methods for preparative chromatographic separation processes. 2014. Diss.

618. VIHAVAINEN, JUHANI. VVER-440 thermal hydraulics as computer code validation challenge. 2014. Diss.

619. AHONEN, PASI. Between memory and strategy: media discourse analysis of an industrial shutdown. 2014. Diss.

620. MWANGA, GASPER GODSON. Mathematical modeling and optimal control of malaria. 2014. Diss.

621. PELTOLA, PETTERI. Analysis and modelling of chemical looping combustion process with and without oxygen uncoupling. 2014. Diss.